Photons, Space and Time: The many Ways of Quantum Walks

January 25, 2026

Der Naturwissenschaftlichen Fakultät der Universität Paderborn
zur Erlangung des Doktorgrades Dr. rer. nat.
vorgelegt von
Federico Pegoraro

Erklärung der Selbstständigkeit

Hiermit versichere ich, die vorliegende Arbeit selbstständig verfasst und keine anderen als die angegebenen Quellen und Hilfsmittel benutzt sowie die Zitate deutlich kenntlich gemacht zu haben.

Paderborn, den 26.01.2026 Federico Pegoraro

Erstgutachter:	Prof. Dr. Christine Silberhorn
Zweitgutachter:	Prof. Dr. Tim Bartley
Vertreter des Mittelbaus:	Dr. Mattias Reichelt
Vorsitzender der Prüfungskommission:	Prof. Dr. Wolf Gero Schmidt

Contents

1 Abstract

In this work we present two implementations of optical quantum networks resorting both to spatial and temporal multiplexing in order to realize evolutions identifiable as discrete time quantum walks.
Additionally, we deal with the preparation of the photon states and their detection.
Depending on the specific system, the input states employed are either coherent light pulses or single photons generated using parametric down-conversion in a dispersion engineered nonlinear medium. From the point of view of detection, we employ both mode-resolved click detection and a fully fledged tomography setup.
Both path- and time-encoded platforms are fully reconfigurable and can realize a large optical interferometer involving their input and output modes. Within the path-encoded platform this is achieved using thermal phase shifters and directional couplers in an integrated device. Instead, the time-multiplexed system exploits fast-switching electro-optical modulators to dynamically act on the polarization space.
Using the spatially-multiplexed platform we demonstrate a resource efficient way of programming the system to reduce the need for detection units and additional devices in order to perform single- and two photon evolutions. In both platforms we investigate loss-induced effects in quantum walks of two photons coupled to an external environment. We employ the time encoded platform to probe the entangling power of quantum walks, showing how the walk dynamics combined with measurement-induced nonlinearities is capable of generating entanglement between the polarization of two photons which were initially in a separable state.
Making use of the full power of the time multiplexed setup in terms of system programmability, we realize the first direct implementation of a time-encoded quantum CNOT achieving a fidelity of $\approx 94\%$. Finally, we demonstrate how the time-multiplexing setup can be used to implement a quantum circuit involving single- and two-qubit gates to generate the four Bell states.

2 Zusammenfassung

In dieser Arbeit werden mehrere Implementierungen optischer Quantennetzwerke vorgestellt, die sowohl räumliches als auch zeitliches Multiplexing einsetzen, um Propagation zu realisieren, die als diskrete zeitliche Quantenirrfahrten (englisch: discrete time quantum walks) identifizierbar sind.

Darüber hinaus befassen wir uns mit der Präparation der Photonzustände sowie deren Detektion.

Je nach verwendetem System bestehen die Eingangszustände entweder aus kohärenten Lichtpulsen oder aus einzelnen Photonen, die durch einen parametrischen Fluoreszenzprozess (englisch: spontaneous parametric down-conversion) in einem dispersionsoptimierten, nichtlinearen Medium erzeugt werden. Für die Detektion kommen sowohl modenaufgelöste Klickdetektion als auch ein vollständig ausgestattetes Tomographie-Setup zum Einsatz.

Sowohl pfad- als auch zeitkodierte Plattformen sind vollständig rekonfigurierbar und können ein großes optisches Interferometer realisieren, das ihre Ein- und Ausgabemoden umfasst. In der pfadkodierten Plattform wird dies durch thermische Phasenschieber und Richtkoppler in einem integrierten Bauteil erreicht, während das zeitmultiplexierte System schnell schaltende elektro optische modulatoren nutzt, um dynamisch auf den Polarisationsraum einzuwirken.

Mit der räumlich multiplexten Plattform wurde eine ressourceneffiziente Methode zur Systemprogrammierung demonstriert, die den Bedarf an Detektionseinheiten und zusätzlichen Komponenten reduziert, um Ein- und Zwei-Photonen-Evolutionen zu realisieren. Mit beiden Plattformen konnten verlustinduzierte Effekte in Quantenirrfahrten von zwei Photonen untersucht werden, die mit einer externen Umgebung gekoppelt sind. Darüber hinaus wurde mit der zeitkodierten Plattform die Verschränkungsfähigkeit von Quantenirrfahrten untersucht. Dabei konnte gezeigt werden, dass die Dynamik der Irrfahrt, kombiniert mit messungsinduzierten Nichtlinearitäten, in der Lage ist, Verschränkung zwischen den Polarisationen zweier Photonen zu erzeugen, die sich ursprünglich in einem separablen Zustand befanden.

Die volle Programmierbarkeit des zeitmultiplexierten Aufbaus wurde schließlich genutzt, um die erste direkte Implementierung eines zeitkodierten Quanten-CNOT-Gatters zu realisieren. Für dieses Gatter konnte eine Leistungsfähigkeit von $\approx 94\%$ im Vergleich zum erwarteten Verhalten nachgewiesen werden. Abschließend wurde gezeigt, dass das zeitmultiplexierte Setup zur Implementierung eines Quanten-Schaltkreises mit Ein- und Zwei-Qubit-Gattern geeignet ist, der die vier Bell-Zustände erzeugt.

3 Introduction

Almost half a century after the first proposal [1] for the adoption of quantum systems as a means of simulation and computation, quantum effects are still intensively investigated as they come with the promise of attaining advantage over classically available technology. Their potential field of application is manifold and comprises uses that range from secure communication [2, 3], efficient prime number factorization [4] and database search [5], to unforgeable money [6] and enhanced measurement precision [7, 8].
In recent years quantum advantage [9] has been proposed for tasks as sampling of random quantum circuits [10], Gaussian boson sampling [11, 12], and has been demonstrated both in superconductive [13, 14] and photonic [15, 16, 17] systems.
Quantum computation relies on three main building blocks: the generation of a resource state, its evolution and its detection. These tree steps respectively aim at encoding information in one of the system's degrees of freedom, processing the information and reading out the process' outcome.
Such a scheme may be implemented in a variety of physical platforms, including superconductive systems [18], trapped ions [19], linear optics [20], neutral atoms [21], nuclear spins in semiconductors [22], and quantum dots [23].
In this work we concentrate on photonic implementations, where photons are the carries of quantum information and their evolution is performed by optical devices. In particular, throughout this work we concentrate on a specific class of evolutions: the quantum walk.

This chapter is devoted to the introduction of the basic concepts and motivation standing behind this work and it is subdivided into three main blocks.
In section (3.1) we focus on the quantum walk: we start by introducing quantum walks from a theoretical point of view posing them in relation to their classical version. We then introduce the two main flavors of quantum walk, which are distinguished by how the evolution takes place from a temporal point of view. In particular, we focus on discrete time quantum walks, specifically on the Hadamard quantum walk. We concentrate on this version of the walk because it is the one implemented experimentally in most of the cases presented in chapter (5).
In section (3.2) we provide a discussion about the state of the art for quantum walks and photonic implementations. In particular, we discuss the importance of quantum walks within the field of quantum information and computation by giving an overview of applications that have benefitted from the use of quantum walks for their investigation. After that, we comment on photonic implementations in a broader sense as they are playing a key role in the development of quantum information and simulation A particular attention is devoted to implementations that exploit path- and time-encoding as these are the degrees of freedom used in the experiments presented in this work.
In section (3.3), we discuss fundamental concepts relative to quantum information which will be useful to comprehend the processes and quantities investigated in this thesis.

3.1 Fundamentals on quantum walks

In this section we deal with the concept of quantum walks. After highlighting the parallelism between classical random walks and quantum walks, we delve deeper in quantum walks by presenting their continuous- and discrete-time versions. We focus particularly on the latter, as it is the one that we have experimentally implemented and used.

3.1.1 Random Walks

The term *random walk*, initially introduced by K. Pearson in [24], denotes a stochastic process where one or more entities called *walkers* move within a mathematical space. In general, it is possible to identify a graph structure underlying the space where the walk takes place. Such a structure is characterized by a set of sites that a walker can visit and can be thought as the set of possible positions where it can find itself at a given time. The structure also features a set of connections among positions which dictates where the walker can go starting at a given position.

A walk starts at any site of the network and proceeds in discrete steps, during which the walker use a probabilistic process to decide where to go next. For instance, it might cast a die with a number of faces matching the number of sites it could move to.

In order to perform a random walk of N steps, the walker repeats this operation N times, after which it has a certain probability of being located at one of the network's sites. A wide range of phenomena can be described and modeled in terms of a random walk, some notable examples include modeling of the path traced by a molecule traveling in a gas or a liquid [25], the study of share prices trends in financial economics [26], describing genetic drift in population genetics [27], and to study the properties of the World Wide Web in computer science [28].

The fundamental example of random walk takes place in one dimension, namely on a discrete infinite line whose sites are identified with the integers of $\mathbb{Z}$. A walker starts its journey at position $x = 0$ and takes a step to the left or to the right by tossing a coin with a bias $p \in [0, 1]$. The bias p may represent the probability of stepping to the right, and therefore increasing x by one.

After performing n steps we would like to know what is the probability is located at position $x = k$. To do so we may consider that the walker can be found at position k if and only if the number of times it moved to the right (n_r) exceeds exactly by k the number of times it moved to the left (n_l). Hence, $n_r - n_l = k$, but at the same time it must be that $n_r + n_l = n$ and therefore $n_r = \frac{n+k}{2}$.

From this follows that the number of walks of n steps, where the walker ended in the desired position is equal to $N(k, n) = \binom{n}{\frac{n+k}{2}}$.

At the same time, the probability of a sequence of n_r moves is given by $p^{n_r}(1-p)^{n-n_r}$, and since each sequence is independent of all the others we find that the position probability distribution after n steps is:

$$P_n(k) = \binom{n}{\frac{n+k}{2}} p^{\frac{n+k}{2}} (1-p)^{\frac{n-k}{2}}, \tag{1}$$

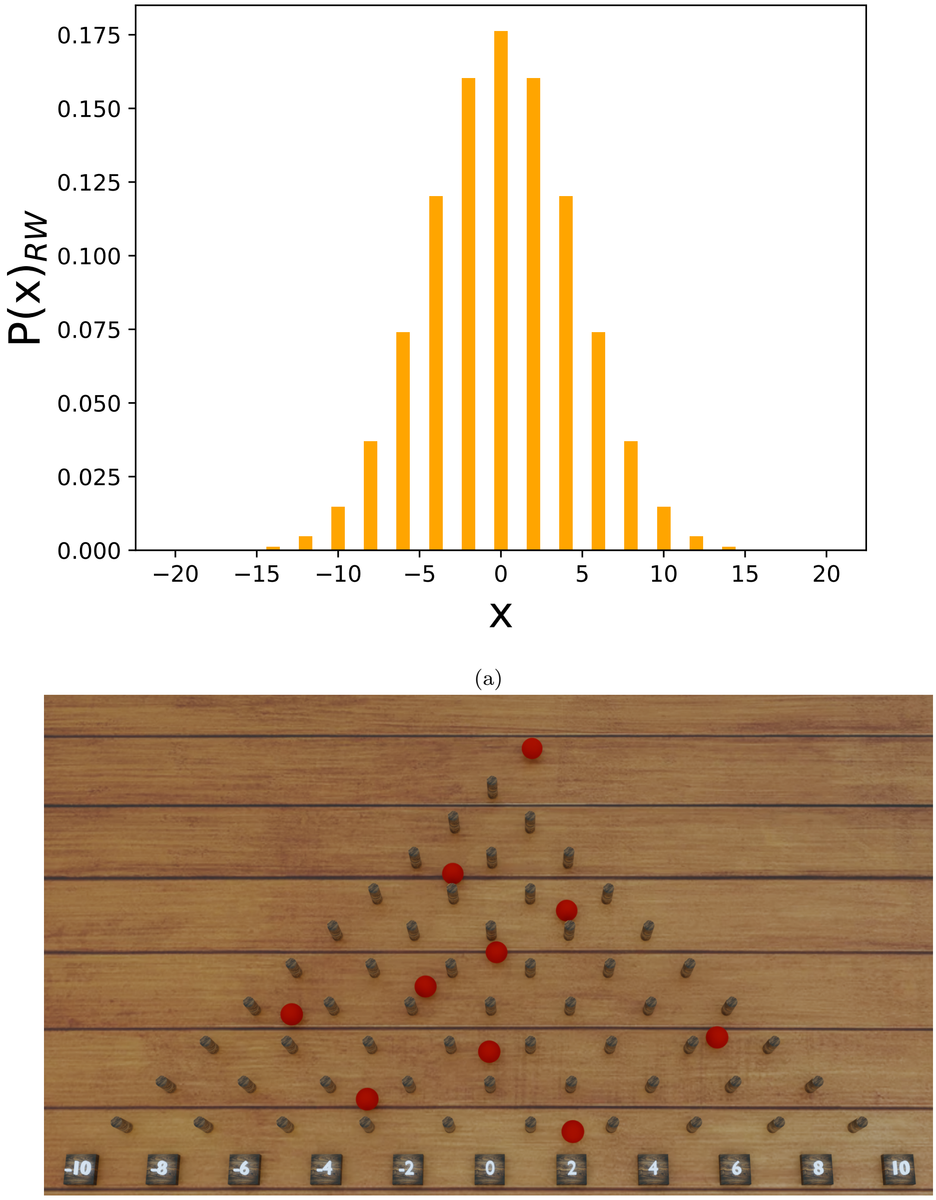

(a)

(b)

Figure 1: **(a):** Position probability distribution for a random walk of 20 steps. The walker starts at x=0 and steps to the left or to the right according to the outcome of a fair coin toss. Here we see how only the even integer positions from −20 to +20 can be occupied and how the distribution is symmetrical and centered on the starting position. **(b):** Galton quincunx or Galton board. A series of beads are dropped from the top onto a set of pins in a triangular arrangement. Upon impinging on a pin the bead falls either to the right or to the left. The process can be modeled as a random walk where each row of pins corresponds to a step and each pin to a position on a discrete line.

which is commonly known as *binomial distribution.*
Since n_r must be an integer such that $0 \leq n_r \leq n$, n and k must have the same parity, and it must be that $-n \leq k \leq n$. Therefore, after an even (odd) number of steps, the walker can only occupy positions identified by and even (odd) integer of $[-n, n]$.
The expected position after n steps of this kind of walk can be obtained by considering the sequence of random variables $\{d_1, d_2, ..., d_n\}$, where d_i corresponds to the displacement of the walker at step i. Since at each step the walker moves by one unity to the right or to the left, we have that $d_i = \pm 1$ with probability p and $1-p$, respectively. Given an instance of the random walk, the walker's final position is obtained as the sum of all the d_i, hence its expected value is:

$$\begin{aligned} \langle x \rangle &= \sum_{i=1}^{n} \langle d_i \rangle = \sum_{i=1}^{n} [p - (1-p)] = \\ &= n(2p-1), \end{aligned} \tag{2}$$

where we notice that depending on the coin bias the walker is more or less likely to be found towards the outermost positions. In particular, for a fair coin, *i.e.* , $p = \frac{1}{2}$, $\langle x \rangle = 0 \ \forall n$, which means that the walker is expected to be found where it originally started.
Fig. 1a shows the output probability distribution for the walker's position after 20 steps of a random walk on a line with the fair coin. We see how the distribution is symmetrical and centered at $x = 0$ with a spread that can be quantified considering that $P_n(k)$ is binomial and its variance σ^2 is proportional to n. Therefore, the distance that the walker travels on average with respect to the mean position scales as $\sqrt{n}$.
Fig. 1b shows a representation of a simple physical system performing a random walk on a line: beads fall under the action of gravity in a set of pins positioned in a pyramidal arrangement typically called *Galton quincunx* or *Galton board* [29]. As it proceeds through the interleaved rows of pegs, upon hitting one of them, each bead has a probability to fall to the right or to the left and proceed to the next row, where the process repeats until it reaches the last one where it ends up in one of the output bins (numbered form -10 to 10 in the figure). In this sense a walk on N steps is performed by a traveling through a board with N rows of pins, while the output bins can be associated to the line positions.

3.1.2 Quantum Walks

As already stated, in a random walk, the walker propagates in a space where the available positions are connected according to a certain network structure. Within this structure many paths may lead the walker from the start position to the end one, however one and only one is taken in a specific walk instance. Additionally, at any step of the walk the walker is to be located at just one position.
Given these considerations a random walker behaves like a classical particle for which it is possible to identify a trajectory as a succession of positions occupied over time. Although this approach successfully models a wide range of phenomena, the classical

nature of the entities involved in a random walk renders it insufficient to deal with any quantum mechanical dynamics.

This becomes possible using a *quantum walk*: in quantum walks the discretized position structure of the classical counterpart is kept, while the walker becomes a quantum object. Therefore, the state of a quantum walker evolves according to the laws of quantum mechanics, which allows it to be in a superposition of the graph sites. Its evolution will not be characterized by a unique trajectory, instead, it will be the result of interfering all possible paths that lead the walker from initial to final position. Moreover, quantum walks featuring multiple walkers show effects of correlations such as bosonic and fermioninc wavefunction symmetries and quantum entanglement.

As any quantum process involving an isolated system, quantum walks follow Schrödinger's equation, hence their temporal evolution must be the result of a unitary operation. This means that, in stark contrast with their classical counterparts, quantum walks follow a deterministic and reversible evolution. Randomness in quantum walks arises from the collapse of the walker's wavefunction following from a measurement of one of its observable quantities, which typically corresponds to its position.

Depending on the way the walker evolves in time, two "flavors" of quantum walks are possible:

Continuous time quantum walks:

According to Schrördinger's equation, a system with an associated Hamiltonian $\hat{H}$ in an initial state $|\Psi(0)\rangle$ evolves in time under the action of a unitary operator $\hat{U}(t)$:

$$|\Psi(t)\rangle = \hat{U}(t)|\Psi(0)\rangle = e^{-\frac{i}{\hbar}\hat{H}t}|\Psi(0)\rangle. \tag{3}$$

In a continuous-time quantum walk, the walk is described by a tight-binding Hamiltonian involving coupling between modes. These modes can be interpreted as the positions accessible to the walker. The couplings between positions define a graph structure with and the adjacency matrix A:

$$A = \begin{cases} -\frac{c_{i,j}}{\hbar} & \text{if } i \text{ and } j \text{ are connected} \\ 0 & \text{else} \end{cases} \tag{4}$$

where $c_{i,j}$ is the coupling among position i and j. In this scheme if the walker starts in a state $|\Psi_0\rangle$, its state at time t is given by:

$$|\Psi(t)\rangle = e^{iAt}|\Psi_0\rangle. \tag{5}$$

Compared to the classical model, we see that the continuous time quantum walk significantly differs from it as the evolution cannot be broken down into a sequence of coin tosses and steps.

Discrete time quantum walks:

In this model the walker consists of a bipartite quantum system arising from the tensor product of a position space $\mathcal{H}_p$ and a coin space $\mathcal{H}_c$.
The evolution takes place in discrete temporal steps: at first an operation $\hat{C}$ acts on the subspace $\mathcal{H}_c$ to put the coin in a superposition of its basis states.
$\mathcal{H}_c$ generally has a finite dimension N, so $\hat{C}$ can be any $N \times N$ unitary operation acting on the states of $\mathcal{H}_c$.
After the coin state is evolved a conditional shift takes place, this is realized by an operation $\hat{S}$ acting on $\mathcal{H}_p$. The dimension of $\mathcal{H}_p$ corresponds to the number of positions that the walker might occupy.
One step of a discrete time quantum walk consists of a unitary $\hat{U} = \hat{S}\hat{C}$, therefore, given an input state $|\psi_s\rangle$ for a walker at step s, the state at step $s+1$ is given by:

$$|\psi_{s+1}\rangle = \hat{U}|\psi_s\rangle. \tag{6}$$

If $\hat{C}$ and $\hat{S}$ are the same at any step, the unitary $\hat{U}^n$ generates the evolution of a discrete time quantum walk of n steps. Because of the intermitting and discretized action of coin and shift operations, this model of quantum walk closely resembles the classical walk.

An extensive account on the mathematical and physical relations among discrete and continuous time quantum walks can be found in [30, 31]. In this work we concentrate exclusively on discrete time quantum walks, in particular we focus on a specific structure for the position space: the infinite discrete line.

3.1.3 Discrete Time Quantum Walk on a Line

In a discrete time quantum walk on a line the walker's state belongs to the bipartite Hilbert space $\mathcal{H} = \mathcal{H}_p \otimes \mathcal{H}_c$, where the position space $\mathcal{H}_p$ is spanned by the basis states $|x\rangle_p$ with $x \in \mathbb{Z}$ and the coin space $\mathcal{H}_c$ spanned by the two states $\{|\uparrow\rangle_c, |\downarrow\rangle_c\}$.
In this composite space a walker can be in a generic state:

$$|\Psi\rangle = \sum_{x\in\mathbb{Z}} \sum_{i\in\{\uparrow,\downarrow\}} \alpha_{x,i}|x\rangle_p \otimes |i\rangle_c, \tag{7}$$

where $\alpha_{x,i}$ are complex amplitudes satisfying the normalization condition:
$\sum_{x,i} |\alpha_{x,i}|^2 = 1$.
The action of $\hat{C}$ on the walker's state is similar to the classical case, where a coin with a given bias is tossed, where we can assimilate the states $|\uparrow\rangle_c$ and $|\downarrow\rangle_c$ to the two possible outcomes of the coin toss. In order to realize this, $\hat{C}$ transforms the two basis states in a superposition, while the position state is left unchanged. This corresponds to the operation:

$$\hat{C}_s = \sum_{x\in\mathbb{Z}} |x\rangle_{pp}\langle x| \otimes \mathcal{C}_{x,s}, \tag{8}$$

where the projectors $|x\rangle_{pp}\langle x|$ make sure that nothing happens to the walker's position

and $\mathcal{C}_{x,s}$ is a unitary operation acting on states of $\mathcal{H}_c$.
The two indices x and s signify the fact that the quantum coin flip might be different depending on the step and position where it is applied.
If we identify $|\uparrow\rangle_c$ and $|\downarrow\rangle_c$ with the vectors $\begin{pmatrix}1\\0\end{pmatrix}$ and $\begin{pmatrix}0\\1\end{pmatrix}$, we can write $\mathcal{C}_{x,s}$ as a 2×2 unitary matrix, which in general takes the form:

$$U = \begin{pmatrix} a & b \\ -e^{i\phi}b^* & e^{i\phi}a^* \end{pmatrix}, \tag{9}$$

with $a, b \in \mathbb{C}$, $\phi \in [0, 2\pi]$ and $|a|^2 + |b|^2 = 1$.
A notable instance is the case where $\mathcal{C}_{x,s}$ is the same at all positions and steps and is represented by the operation:

$$\hat{H} = \frac{1}{\sqrt{2}} \begin{pmatrix} 1 & 1 \\ 1 & -1 \end{pmatrix}, \tag{10}$$

and therefore the coin operation becomes:

$$\hat{C}_H = \mathbb{I}_p \otimes \hat{H}, \tag{11}$$

where $\mathbb{I}_p$ is the identity operator for the position space. $\hat{C}_H$ is commonly referred to as *Hadamard coin*, and the quantum walk that results from its application is the *discrete time Hadamard quantum walk* or, as we will call it from now on, *Hadamard walk*.
After the coin state is evolved the step is completed by a conditional shift operation defined as:

$$\hat{S} = \sum_{x\in\mathbb{Z}} |x+1\rangle_{pp}\langle x| \otimes |\uparrow\rangle_{cc}\langle\uparrow| + |x-1\rangle_{pp}\langle x| \otimes |\downarrow\rangle_{cc}\langle\downarrow|. \tag{12}$$

From this definition follows that all the state contributions associated to the coin state $|\uparrow\rangle_c$ are shifted one position to the right, while contributions relative to $|\downarrow\rangle_c$ move one position to the left. If we now consider a walk of n steps with input state $|\Psi_0\rangle$, the output state is given by:

$$|\Psi_n\rangle = \left(\prod_{s=1}^{n} \hat{S}\hat{C}_s\right) |\Psi_0\rangle \tag{13}$$

In an Hadamard walk, $\hat{C}_H$ maps $|\uparrow\rangle_c$ and $|\downarrow\rangle_c$ as follows:

$$\begin{aligned} |\uparrow\rangle_c &\to \frac{|\uparrow\rangle_c + |\downarrow\rangle_c}{\sqrt{2}}, \\ |\downarrow\rangle_c &\to \frac{|\uparrow\rangle_c - |\downarrow\rangle_c}{\sqrt{2}}. \end{aligned} \tag{14}$$

In both cases the transformation results in an even superposition of $|\uparrow\rangle_c$ and $|\downarrow\rangle_c$, thus the relative local position state is shifted to the left or to the right with equal probability. For this reason we can consider the Hadamard walk the quantum

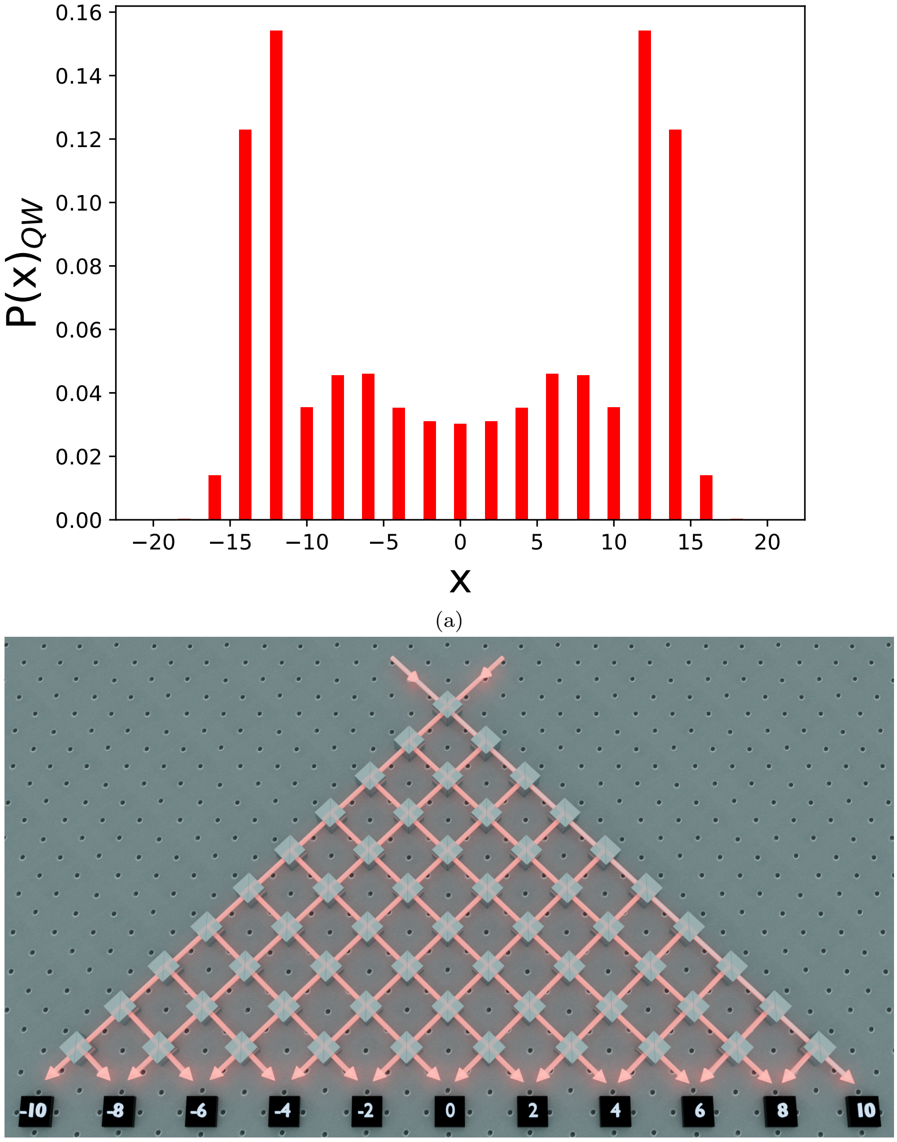

(a)

(b)

Figure 2: **(a):** Output position probability for an Hadamard walk of 20 steps starting at position 0 and coin $\frac{|\uparrow\rangle_c + i|\downarrow\rangle_c}{\sqrt{2}}$. Similarly to the classical case the walker occupy only even positions from -20 to $+20$ and feature a symmetrical shape, however with pronounced peaks on the sides, therefore the walker features a larger spread over the position space. **(b):** Optical implementation of an Hadamard walk. A series of 50:50 beam splitters is arranged as the pins of a Galton board. Light enters at the input beam splitter and propagates thought the network where each row of beam splitters implements one step of the evolution. Here a beam splitter implements at the same time coin and conditional shift by putting the state of the incoming photons in a superposition of the two outputs.

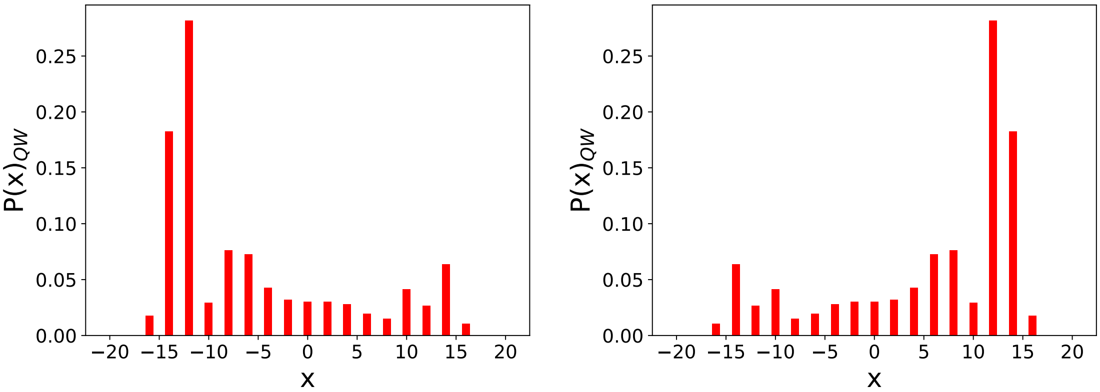

(a)

(b)

Figure 3: Coin dependence of the output probability distribution of an Hadamard walk. **(a):** Hadamard walk of 20 steps stating at position 0 with coin $|\uparrow\rangle_c$. In contrast to what is shown in Fig. 2a the output distribution features only one peak on the left side of the position space. **(b):** Hadamard walk of 20 steps stating at position 0 with coin $|\downarrow\rangle_c$. In contrast to what is shown in Fig. 2a the output distribution features only one peak on the right side of the position space.

counterpart of a random walk on a line with a fair coin.
At this point we can discuss the expected output probability distribution for the position occupied by the walker after N steps.
Keeping in mind the general form of the walker's state (see Eq. (7)), the position probability distribution is given by:

$$P_{QW}(x,N) = |\alpha_{x,\uparrow}(N)|^2 + |\alpha_{x,\downarrow}(N)|^2, \tag{15}$$

where the functional dependence on N is added to the $\alpha_{x,i}$ coefficients to signify that they are the coefficients obtained applying the coin and shift operators N times to the input state. Here we also notice that $P_{QW}(x,N)$ always consists of two separated contributions corresponding to the two possible coin states. These two contributions can be understood as the probabilities for a walker to be found at position x with coin state $|\uparrow\rangle_c$ or $|\downarrow\rangle_c$, respectively.
In contrast to the classical case, it is not possible to categorize the output distribution of the quantum walk into a specific class of probability distributions like the one seen in Eq.(1). Fig.(2a) shows the output distribution for an Hadamard walk of 20 steps where the walker is initiated in the state $|\psi_0\rangle = \left(\frac{|\uparrow\rangle+i|\downarrow\rangle}{\sqrt{2}}\right)_c \otimes |0\rangle_p$. Comparing this picture with the one of Fig.(1a) we can notice significant qualitative differences among quantum and classical cases. While the classical walk features a bell-shaped distribution centered around the starting position, the quantum one exhibits two large peaks located at the two sides of the accessible position space. This means that the probability of finding the quantum walker at the center, *i.e.* near to the input position, is much lower than in the classical case. At step N the deviation from the mean position, quantified by the standard deviation of $P_{QW}(x,N)$, is $O(N)$ [32], thus the

Hadamard walk spreads faster than its classical counterpart, whose scaling is $O(\sqrt{N})$.
A final remarkable difference among quantum and random walk is the fact that the output of a quantum walk strongly depends on the input coin state. In fact, if we take the two input states $|\psi_{\uparrow}\rangle = |\uparrow\rangle_c \otimes |0\rangle_p$ and $|\psi_{\downarrow}\rangle = |\downarrow\rangle_c \otimes |0\rangle_p$ the output distributions after 20 steps for these two states look like the ones shown in Figs.(3a) and (3b), where we still see peaks at the edges of the position space, but the overall distributions appear to be skewed towards one or the other side.

In analogy to the classical random walk we can envision a physical realization of a quantum walk following the scheme shown in Fig.(2b), where we have again a Galton board but this time instead of pins, the board is constituted by optical beam splitters, while the walkers are photons of light. Upon impinging on a beam splitter the state of a photon is cast into a superposition of the two paths corresponding to the beam splitter output ports. This action constitutes the coin operation, which in case of a $50:50$ beam splitter can be modeled as the Hadamard coin of Eq.(11). The shift operation arises from the propagating nature of light, which can be thought as a position update dependent on the beam splitter output from which the photon came from.

3.2 State of the art

Now that we have illustrated the principles of quantum walks, with a particular focus on their discrete time version, we discuss their importance within the field of quantum information and computation. In particular, we start by providing an overview of the various frameworks where quantum walks have proven themselves useful. We comment on possible implementations of quantum walks with a particular focus on the photonic ones. Finally, we expand more on the importance of photonic implementations that exploit light path and/or time as degree of freedom to implement large quantum networks.

3.2.1 Applications of Quantum Walks

Given their general mathematical structure, quantum walks are well suited to model and study the evolution of a complex quantum network. Both continuous and discrete time walks may be applied to quantum computing [33, 34, 35], for instance, search algorithms are a prominent example where they have been successfully employed [36, 37]. From the point of view of quantum simulation, quantum walks can be applied to the investigation of physical processes and have been used in the study of relativistic wave-packet spread [38], energy transfer in photosintetic systems [39, 40], dephasing assisted transport [41], molecular binding [42], Bloch oscillating spinor atoms [43], nonlinear Dirac equations and solitons [44]. Given the symmetries present in quantum walks, they have also been exploited to investigate topological phenomena [45, 46, 47]. In addition, photonic quantum walks constitute an adequate platform for the implementation of boson sampling [48, 49, 50, 51, 52].

3.2.2 Implementations of Quantum Walks

From an experimental point of view, a quantum walk may be implemented in any quantum system where a walker can be identified, and its state is redistributed across many modes according to the dynamics discussed in 3.1.

Therefore, continuous time quantum walks can be implemented in any system where a set of modes feature fixed coupling constants which determine the probability for a walker to evolve from one mode to the other. For this reason continuous time walks have been implemented using integrated optics in waveguide arrays [53, 54, 55, 56].

On the other hand, in order to realize a discrete time quantum walk, the system of choice must exhibit a bipartite structure, *i.e.* an internal and external degree of freedom serving as coin and position, respectively. Experimentally, the coin state may be implemented using hyperfine levels in ions and atoms [57, 58, 59, 60] as well as nuclear spins in molecules [61].

If instead we look into photonic approaches, we find that multiple properties of light can be employed to realize walks with photons. Many implementations exploit the path taken by light as position degree of freedom , for instance, in bulk implementations involving beam displacers [62, 63, 64], beam splitters cascades [52], or combinations of beam displacers and beam splitters [65]. Also, directional couplers in laser written

waveguide arrays have been used [66, 67, 68, 69]. When looking at degrees of freedom different from path, frequency has been used [70] as well as light optical angular moment [71, 72, 73, 74]. Time has also been harnessed to efficiently implement the walk dynamics in looped architectures featuring fiber delays [75, 76, 77].
An overview over experimental implementations of quantum walks can be found in [78].

3.2.3 Interest in path- and time-multiplexing

We live in the era of noisy intermediate scale quantum computing (NISQ) [79], which means that the available quantum hardware is still limited in terms of resources and error correction. Therefore, current research both in academic and industrial environments tends to the development of novel systems with improved capabilities which may ultimately lead to quantum advantage.
In practice, quantum computing has been pursued exploiting a variety of physical strategies. Notable ones involve, for instance, spins of charged particles in semiconductors [80], nuclear magnetic resonance in atomic nuclei [81], trapped ions [82] and quantum dots [83]. Others exploit vibrational energy levels in molecules [84], superconductive systems [85], or topological properties of two-dimensional systems [86].
As shown by several works [87, 20, 88], photonic systems can be exploited for quantum computing. This approach offers excellent isolation between system and external environment allowing for instance operation at room temperature. Additionally, photonic strategies grant ease of manipulation of the single qubit states via linear optical elements combined with measurement-induced non-linearities.
Recent years have witnessed an increasing effort in the development of large optical networks, where many photons evolve according to a unitary evolution.
This requires the adoption of suitable schemes to implement the desired process exploiting one or more degrees of freedom of light.
To this aim, several strategies have been proposed to implement linear optical processors using path encoding [89, 90], as well as time [91]. Quantum walks fit well in this framework as they constitute a prime example of large optical evolution network. Time-multiplexing platforms capable of implementing walks with dynamical coins through the adoption of fast electro-optical modulators have rendered possible to study phenomena as noise and Anderson localization [92, 93], percolation [94], state transfer and finite graphs [95]. Using time encoded systems it has been possible to generate large cluster states [96, 97]. At the same time, machines that exploit path encoding for modular quantum computing have been proposed [98]. In terms of quantum computational advantage, both strategies have been successfully employed in the framework of boson sampling both in its Gaussian [17, 99, 100] and scattershot [101, 102] versions.

3.3 Quantum Information

In this section we discuss some key concepts pertaining quantum information and computation.
We start introducing the quantum bit (qubit), which constitutes at the same time the elementary unit of quantum information and the fundamental building block for quantum computing.
Then we expand on the evolution of qubits both in the case of ideal and noisy systems. Afterward, we describe how states of multiple qubits can be reconstructed. At the end of the section, we focus on quantum entanglement: one of the key features of quantum mechanics and a powerful resource in quantum computation.

3.3.1 The quantum bit

A quantum bit, or qubit, can be any two level quantum system, *i.e.* a quantum mechanical object whose state belongs to a complex Hilbert space $\mathcal{H}$ with dimension equal to 2.
In such a space one may choose an orthonormal basis identified by the two vectors:

$$|0\rangle = \begin{pmatrix} 1 \\ 0 \end{pmatrix}, \ |1\rangle = \begin{pmatrix} 0 \\ 1 \end{pmatrix}. \tag{16}$$

The two states of this *computational* basis, are the quantum equivalent of the 0 or 1 values of a classical bit.
Any state of $\mathcal{H}$ can be expressed in terms of the $|0\rangle$ and $|1\rangle$ basis states as:

$$|\psi\rangle = \alpha|0\rangle + \beta|1\rangle, \tag{17}$$

where α and β belong to $\mathbb{C}$ and satisfy the normalization condition: $|\alpha|^2 + |\beta|^2 = 1$. The physical implication of Eq. (17), is that a qubit does not exclusively exist in the $|0\rangle$ or $|1\rangle$ state. Instead, its state can be a superposition of the two computational states.
Since quantum states are defined up to a global phase of no physical importance, it is possible to require the α parameter of Eq. (17) to be real. Under this assumption and keeping in mind the normalization condition, the qubit state may be rewritten as:

$$|\psi\rangle = \cos\frac{\theta}{2}|0\rangle + e^{i\phi}\sin\frac{\theta}{2}|1\rangle, \tag{18}$$

with $\theta \in [0, \pi]$ and $\phi \in [0, 2\pi)$.
As shown in Fig. 4, the parameters θ and ϕ define a point on a 3-dimensional unit sphere often referred to as the *Bloch sphere*.
This geometric representation is useful to picture how the state of a qubit transforms, additionally it must be noted that this formalism is similar to the one used in optics to graphically represent different types of polarized light.
By embedding the Bloch sphere in the three-dimensional space, the Cartesian axes define six points on the sphere corresponding to the six quantum states:

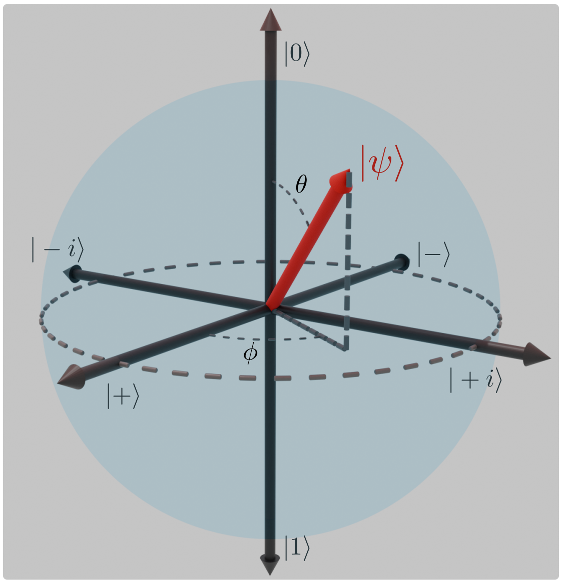

Figure 4: The Bloch sphere is a geometrical representation of the possible states of any two-level quantum system. Each point on the sphere's surface represents a pure state $|\psi\rangle$. The sphere's radius equals one because of the normalization condition for quantum states, therefore $|\psi\rangle$ is uniquely identified by the two angles θ and ϕ. States located at the intersections between the sphere and the Cartesian axes correspond to the eigenstates of the Pauli operators (see. Eq. (22)).
Points inside the sphere represent statistical mixtures of states, which can be uniquely identified by a Bloch vector $\vec{r}$, whose length is smaller than one.

Z-axis:

$$\begin{cases} |0\rangle & \theta = 0 \quad \phi = 0 \\ |1\rangle & \theta = \pi \quad \phi = 0 \end{cases} \tag{19}$$

X-axis:

$$\begin{cases} |+\rangle = \frac{|0\rangle+|1\rangle}{\sqrt{2}} & \theta = \frac{\pi}{2} \;\; \phi = 0 \\ |-\rangle = \frac{|0\rangle-|1\rangle}{\sqrt{2}} & \theta = \pi \;\; \phi = \pi \end{cases} \tag{20}$$

Y-axis:

$$\begin{cases} |+i\rangle = \frac{|0\rangle+i|1\rangle}{\sqrt{2}} & \theta = \frac{\pi}{2} \;\; \phi = \frac{\pi}{2} \\ |-i\rangle = \frac{|0\rangle-i|1\rangle}{\sqrt{2}} & \theta = \pi \;\; \phi = \frac{3}{2}\pi. \end{cases} \tag{21}$$

The importance of these states is related to the Pauli operators:

$$\hat{\sigma}_z = \begin{pmatrix} 1 & 0 \\ 0 & -1 \end{pmatrix}, \; \hat{\sigma}_x = \begin{pmatrix} 0 & 1 \\ 1 & 0 \end{pmatrix}, \; \hat{\sigma}_y = \begin{pmatrix} 0 & -i \\ i & 0 \end{pmatrix}. \tag{22}$$

Considering the vectorial parametrization of the computational basis (see Eq.16) it is possible to rewrite the above operators as:

$$\begin{aligned}\hat{\sigma}_z &= |0\rangle\langle 0| - |1\rangle\langle 1| \\ \hat{\sigma}_x &= |+\rangle\langle +| - |-\rangle\langle -| \\ \hat{\sigma}_y &= |+i\rangle\langle +i| - |-i\rangle\langle -i|.\end{aligned} \tag{23}$$

From this rewriting it is immediate to realize that the six states $|0\rangle$, $|1\rangle$, $|\pm\rangle$ and $|\pm i\rangle$ are the eigenstates of the Pauli operators.

So far we only considered how the state of a qubit is expressed in terms of state vectors. An alternative language is the one that employs a tool known as *density matrix* or *density operator*. This formalism is perfectly equivalent to the one of state vectors, with the additional advantage of being able to describe cases where it is not possible to represent the system's state using a state vector.

This happens when there is and ensemble of pure states $|\psi_i\rangle$, and we only know that the system is found in the $i-th$ state with probability p_i. In this case we represent the system state using the density operator:

$$\hat{\rho} = \sum_i p_i |\psi_i\rangle\langle\psi_i|. \tag{24}$$

As a consequence of this formulation, the density operator associated to a pure state $|\psi\rangle$ is given by: $\hat{\rho}_\psi = |\psi\rangle\langle\psi|$.

Before commenting on the specific case of qubits, let us recapitulate the general properties of a density operator:

- **Normalization:** the trace of any density operator $\hat{\rho}$ is equal to one, this is equivalent to the normalization condition for pure states.
- **Observability:** As it can be seen by its definition, $\hat{\rho}$ is Hermitian, thus according to the postulates of quantum mechanics it constitutes a physically measurable object.
- **Positivity:** $\hat{\rho}$ is a positive operator. This means that for any vector $|\phi\rangle$, $\langle\phi|\hat{\rho}|\phi\rangle \geq 0$.
- **Purity criterion:** for any density operator $\hat{\rho}$, $Tr(\hat{\rho}^2) \leq 1$, in particular $Tr(\hat{\rho}^2) = 1$ if and only if $\hat{\rho}$ represents a pure state.

Coming back to the case of a qubit, we have that its density operator can be written in the computational basis as:

$$\hat{\rho} = \sum_{i,j\in\{0,1\}} \rho_{ij} |i\rangle\langle j|, \tag{25}$$

where the coefficients ρ_{ij} must satisfy the following conditions: ρ_{00} and ρ_{11} must be real and such that $\rho_{00} + \rho_{11} = 1$; the coefficients ρ_{01} and ρ_{10} may be complex and fulfill the condition: $\rho_{01} = \rho_{10}^*$.

By regrouping the terms of this expression for $\hat{\rho}$ and comparing it to the form taken by the Pauli operators in the computational basis, it can be shown that any single qubit density operator takes form:

$$\hat{\rho} = \frac{1}{2}(\mathbb{I} + \vec{r} \cdot \vec{\sigma}), \tag{26}$$

where $\mathbb{I}$ represents the 2x2 identity operator, the operation ”$\cdot$” formally corresponds to the usual Euclidean scalar product in three-dimensions. The vector $\vec{\sigma}$ is a *Pauli vector* and it is defined as $(\hat{\sigma}_x, \hat{\sigma}_y, \hat{\sigma}_z)$, while $\vec{r}$ is a three-dimensional vector with real entries and length smaller or equal than one.
The vector $\vec{r}$ is often referred to as *Bloch vector* and it identify a quantum state with a point within the Bloch sphere. In particular, all pure states have Bloch vectors of unitary length, while states with $||\vec{r}|| < 1$ correspond to statistical mixtures. The case $||\vec{r}|| = 0$ identifies a state located at center of the Bloch sphere and corresponds to the density operator $\hat{\rho} = \frac{\mathbb{I}}{2}$.
This state is said to be *completely mixed*, in fact it can be understood as an equiprobable mixture of any possible pair of basis states of $\mathcal{H}$.
Besides allowing for a comprehensive representation of both pure and mixed quantum states; the density matrix formalism is useful to handle composite systems. Let us consider for instance a bipartite system. Such a system results from the combination of two subsystems from two Hilbert spaces $\mathcal{H}_1$ and $\mathcal{H}_2$, where we can identify two basis sets $\{|i\rangle_1\}$ and $\{|j\rangle_2\}$. Its overall state resides in an Hilbert space $\mathcal{H} = \mathcal{H}_1 \otimes \mathcal{H}_2$, which is the tensor product of the spaces associated to the two subsystems.
In the bipartite case, a pure state can be written as:

$$|\psi\rangle = \sum_{i,j} c_{i,j} |i\rangle_1 \otimes |j\rangle_2. \tag{27}$$

From now on we denote the tensor product $|i\rangle_1 \otimes |j\rangle_2$ with the short-hand notation $|ij\rangle$, whereby the first and second index refer to the subsystem 1 and 2, respectively. The density operator associated to $|\psi\rangle$ is:

$$\hat{\rho} = \sum_{i,\alpha} \sum_{j,\beta} c_{i,\alpha} c^*_{j,\beta} |i, \alpha\rangle\langle j, \beta|. \tag{28}$$

If we are interested only in the state of one subsystem we can use the *reduced* density operators:

$$\hat{\rho}_1 = Tr_2(\hat{\rho}) = \sum_i {}_2\langle i|\hat{\rho}|i\rangle_2, \tag{29}$$

$$\hat{\rho}_2 = Tr_1(\hat{\rho}) = \sum_j {}_1\langle j|\hat{\rho}|j\rangle_1. \tag{30}$$

The operations Tr_1 and Tr_2 denote the partial traces on one of the two subsystems.

3.3.2 Evolution (part I): The circuit model of quantum computation

A classical computer can be described as a finite register of n classical bits [103]. One can devise elementary logical operations acting on single bit or pairs of bits that can be combined in an ordered way to implement any given logic function. This model of computation goes by the name of *circuit model.* A quantum computer may be thought as a collection of n qubits, whose state is described in terms of a tensor product of n two-dimensional Hilbert spaces. Such a state takes the form:

$$|\psi\rangle = \sum_{i=0}^{2^n-1} c_n|i\rangle = \sum_{i_{n-1},i_{n-2},\dots,i_1,i_0=0}^{1} c_{i_{n-1},i_{n-2},\dots,i_1,i_0}|i_{n-1},i_{n-2},...,i_1,i_0\rangle. \qquad (31)$$

Provided that one is able to initialize the state of the n qubits, it is necessary to manipulate the quantum computer's wave function to carry out any task of interest. Since the quantum computer is an n-body quantum system, its temporal evolution is governed by the Schrödinger equation. Therefore, assuming that the system is closed, *i.e.* there is no coupling between system and external environment, the evolution a quantum computer is described by a unitary operation. It must be emphasized that even if the evolution of the wavefunction of Eq. (31) is parameterized by a $2^n \times 2^n$ unitary matrix, this matrix can always be decomposed into the combined action of smaller unitaries acting only one or two qubits [104]. Analogously to classical computing, these elementary unitaries constitute the so-called *quantum gates* for the circuit model of quantum computation.

Single-qubit gates

Quantum gates acting on single qubits are represented by 2×2 unitary matrices. Among all the possible choices two gates stand out: the Hadamard and phase-shift gates. Their importance is associated to the fact that any single qubit unitary can be decomposed into the action of these two gates.

The *Hadamard gate* is defined in the computational basis as:

$$\hat{H} = \frac{1}{\sqrt{2}}\begin{pmatrix}1 & 1\\ 1 & -1\end{pmatrix}. \qquad (32)$$

The $\hat{H}$ gate transforms states of the computational basis $\{|0\rangle, |1\rangle\}$ into the states $\{|+\rangle, |-\rangle\}$. Since $\hat{H}^2 = \mathbb{I}$, the inverse transformation of $\hat{H}$ is the Hadamard gate itself.

The *Phase gate* is defined in the computational basis as:

$$\hat{R}_z\left(\delta\right) = \begin{pmatrix}1 & 0\\ 0 & e^{i\delta}\end{pmatrix}. \qquad (33)$$

When this gate acts on the states of the computational basis, it leaves $|0\rangle$ unchanged and transforms $|1\rangle$ into $e^{i\delta}|1\rangle$. The action of the phase gate can be better understood considering how it transforms a qubit in a an arbitrary state $|\psi\rangle$ (see Eq. (18)):

$$\hat{R}_z\left(\delta\right)|\psi\rangle = \begin{pmatrix} 1 & 0 \\ 0 & e^{i\delta} \end{pmatrix} \begin{pmatrix} \cos\frac{\theta}{2} \\ e^{i\phi}\sin\frac{\theta}{2} \end{pmatrix} = \begin{pmatrix} \cos\frac{\theta}{2} \\ e^{i(\phi+\delta)}\sin\frac{\theta}{2} \end{pmatrix}. \tag{34}$$

It is readily seen from this equation, that the phase gate generates a counterclockwise rotation of an angle δ about the z axis of the Bloch sphere.

In general the action of a single qubit unitary operation can be understood as the process of transferring the qubit state from one point of the Bloch sphere to another. This can be obtained using these two quantum gates.

In fact starting from the state $|0\rangle$ we can consider the following transformation:

$$\hat{R}_z\left(\frac{\pi}{2}+\phi\right)\hat{H}\hat{R}_z\left(\theta\right)\hat{H}|0\rangle = e^{i\frac{\theta}{2}}\left(\cos\frac{\theta}{2}|0\rangle + e^{i\phi}\sin\frac{\theta}{2}|1\rangle\right), \tag{35}$$

where on the left side we apply only Hadamard and phase gates and on the right side we recognize the expression of a generic qubit.

From Eq. 35 we can conclude that phase and Hadamard gate can map the basis state $|0\rangle$ into any other state, but also that a generic single-qubit state $|\psi\rangle$ can transformed in $|0\rangle$ using the same type of gates in reverse to implement the operation $\hat{H}\hat{R}_z\left(-\theta\right)\hat{H}\hat{R}_z\left(-\frac{\pi}{2}-\phi\right)$.

Therefore, a generic state $|\psi\rangle$ can be mapped to another generic state $|\phi\rangle$ by first applying the transformation that turns $|\psi\rangle$ into $|0\rangle$ and then the transformation that maps $|0\rangle$ to $|\phi\rangle$.

Two-qubit gates

We have seen how for a single qubit one can define a set of operations capable of mapping a point on the surface of the Bloch sphere to any other one. However, when considering a system of n qubits, single qubit operations are not enough to map the initial state of the system to any other one.

We can convince ourselves of this fact considering the case of two qubits in the generic state:

$$|\Psi\rangle = \alpha|00\rangle + \beta|01\rangle + \gamma|10\rangle + \delta|11\rangle, \tag{36}$$

where the coefficients α, β, γ and δ are complex and satisfy the normalization condition: $|\alpha|^2 + |\beta|^2 + |\gamma|^2 + |\delta|^2 = 1$. Because of this condition and since we can always force one of the four coefficients to be real by redefining $|\psi\rangle$ up to a global phase, the general two-qubit state is described by six real parameters.

Now let us consider a separable state $|\Psi\rangle = |\psi_1\rangle \otimes |\psi_0\rangle$, consisting of a tensor product of two single-qubit states. Since $|\psi_1\rangle$ and $|\psi_0\rangle$ are uniquely identified by two real parameters, a state of this kind is defined by four parameters, therefore separable states are a smaller subset of all possible two-qubit states.

If we now take $|\Psi\rangle = |\psi_1\rangle \otimes |\psi_0\rangle$ and apply only single qubit transformations, we obtain a new state $|\Psi'\rangle = |\psi_1'\rangle \otimes |\psi_0'\rangle$, which despite the fact that $|\psi_1'\rangle$ and $|\psi_0'\rangle$ can be any two single-qubit states, it is still separable. Therefore, it is not possible to

transform $|\Psi\rangle$ in any arbitrary two-qubit using only single qubit operations.
This can be achieved only combining single-qubit gates and operations involving an interaction between two qubits.
The prototypical two-qubit gate is the CNOT gate. The action of the CNOT gate in the two-qubit computational basis is parametrized by the unitary matrix:

$$\hat{U}_{CNOT} = \begin{pmatrix} 1 & 0 & 0 & 0 \\ 0 & 1 & 0 & 0 \\ 0 & 0 & 0 & 1 \\ 0 & 0 & 1 & 0 \end{pmatrix}. \tag{37}$$

Alternatively we can write: $CNOT(|x, y\rangle) = |x, y \oplus x\rangle$, where $x, y = 0, 1$ and $\oplus$ indicates the addition modulo 2. The CNOT gate can transform a separable state in a non-separable one. For instance, we may consider the operation:

$$CNOT((\alpha|0\rangle + \beta|1\rangle) \otimes |0\rangle)) = \alpha|00\rangle + \beta|11\rangle \tag{38}$$

where we can see that the input is a tensor product of single qubit states, but the output is non-separable for any $\alpha, \beta \neq 0$.

With this we have a complete picture of the single- and two-qubit operations. In classical computation a small set of gates (e.g. AND, OR, NOT) are sufficient to compute any arbitrary classical logical function. Such a set is *universal* for classical computation. A similar concept of universality is true for quantum computation. A set of gates is said to be *universal for quantum computing* if any unitary operation may be approximated to an arbitrary accuracy by a quantum circuit involving only those gates. The construction of a universal set of gates is not necessarily unique, in fact several approaches exist [105]. Notably, a set encompassing single qubit rotations on the Bloch sphere, phase gate and the CNOT constitutes a universal set of quantum gates [106].

3.3.3 Evolution (part II): closed vs open systems

As we have stated in the previous section, the evolution of a register of qubits is unitary under the assumption of complete isolation between system and external environment. Now we drop this assumption and discuss an approach to the description of an open system, *i.e.* a system that interacts with an external environment.
In this approach, also known as *Kraus representation*, we treat register and environment as an overall bipartite system starting in the separable state:

$$\hat{\rho}_{12} = \hat{\rho}_1 \otimes |0\rangle_{2\,2}\langle 0|, \tag{39}$$

where $\hat{\rho}_1$ is the initial state of the register, while $|0\rangle_2$ is the initial state of the environment.
By definition, the overall system is isolated, thus its evolution is unitary. Therefore, the

joint state $\hat{\rho}_{12}$ evolves into a new one according to:

$$\hat{\rho}'_{12} = \hat{U}\hat{\rho}_{12}\hat{U}^\dagger = \hat{U}\hat{\rho}_1 \otimes |0\rangle_{2\,2}\langle 0|\hat{U}^\dagger. \tag{40}$$

In a realistic scenario, an observer does not have access to the environment and can only measure the register, thus we are only interested in the state of subsystem 1. Following Eq. (29), this can be obtained by tracing over the environment:

$$\begin{aligned} \hat{\rho}'_1 = Tr_2[\hat{\rho}'_{12}] &= \sum_k {}_2\langle k|\hat{U}\hat{\rho}_1 \otimes |0\rangle_{2\,2}\langle 0|\hat{U}^\dagger|k\rangle_2 = \\ &= \sum_k {}_2\langle k|\hat{U}|0\rangle_2\,\hat{\rho}_1\,{}_2\langle 0|\hat{U}^\dagger|k\rangle_2, \end{aligned} \tag{41}$$

where $\{|k\rangle_2\}$ is a basis set of the environment Hilbert space and ${}_2\langle k|\hat{U}|0\rangle_2$ is an operator acting on the space of our qubit register. We can define the *Kraus operators*:

$$\hat{E}_k = {}_2\langle k|\hat{U}|0\rangle_2, \tag{42}$$

where we have that $\sum_k \hat{E}_k^\dagger \hat{E}_k = \mathbb{I}$.
With this definition we can rewrite the evolved state of system 1 as in terms of the linear map:

$$\mathcal{S}: \ \hat{\rho}_1 \to \hat{\rho}'_1 = \sum_k \hat{E}_k \hat{\rho}_1 \hat{E}_k^\dagger. \tag{43}$$

$\mathcal{S}$ is known as *superoperator* and Eq. (43) goes under the name of *Kraus representation* or *operator-sum representation* of the superoperator. Since the result of $\mathcal{S}$ must be a density operator, as shown in [107], the Kraus representation must satisfy the following properties:

- $\mathcal{S}$ is trace preserving: $Tr\{\hat{\rho}_1\} = Tr\{\hat{\rho}'_1\} = 1$.
- $\mathcal{S}$ preserves Hermiticity: $\hat{\rho}_1^\dagger = \hat{\rho}_1$ and $(\hat{\rho}'_1)^\dagger = \hat{\rho}'_1$.
- $\mathcal{S}$ preserves positivity: $\langle\phi|\hat{\rho}_1^\dagger|\phi\rangle \geq 0$ and $\langle\psi|\hat{\rho}_1^\dagger|\psi\rangle \geq 0$ for any state $|\phi\rangle$ and $|\psi\rangle$.
- $\mathcal{S}$ is completely positive: for any extension $\mathcal{H}_1 \otimes \mathcal{H}_E$ of $\mathcal{H}_1$ the superoperator $\mathcal{S} \otimes \mathbb{I}_E$ is positive. That is, if we add any system E with a trivial dynamics ($\mathbb{I}_E$ represents the identity acting on E) to system 1 the overall superoperator is positive.

We can imagine a superoperator $\mathcal{S}_A$ as the way of describing the evolution of $\hat{\rho}_1$ from a time t_0 to t_1, however it is not possible to treat the backwards evolution for t_1 to t_0 in the same terms without knowing the state of the environment after at time t_1. In fact it can be shown that a superoperator is invertible if and only if it is unitary [108]. From a physical point of view this means that an arrow of time has been introduced for the system. This phenomenon is known as *decoherence* and we apply it in the framework of quantum walks in section 5.2.

3.3.4 Measuring the state of a qubit

The remaining building block of any quantum computation protocol is to measure the state of the quantum computer.

The state of a single qubit is uniquely determined by the coordinates (x, y, z) of its associated Bloch vector $\vec{r}$. Therefore, the measurement must be able to determine where the state lies within the Bloch sphere and the question is what observables can be employed to this aim.

Given any observable $\hat{O}$, its expectation value on the state represented by a density operator $\hat{\rho}$ is obtained as:

$$\langle \hat{O} \rangle = Tr(\hat{O}\hat{\rho}). \tag{44}$$

In prticular, the expectation value of any of the Pauli operators on a single qubit state takes the form:

$$\langle \hat{\sigma}_i \rangle = \frac{1}{2} Tr(\hat{\sigma}_i + \hat{\sigma}_i(x\hat{\sigma}_x + y\hat{\sigma}_y + z\hat{\sigma}_z)). \tag{45}$$

Considering that the trace of the Pauli operators is zero and the identity: $\hat{\sigma}_i\hat{\sigma}_j = \delta_{ij}\mathbb{I} + i\epsilon_{ijk}\hat{\sigma}_k$, where δ_{ij} and ϵ_{ijk} are respectively the Kronecker and Levi-Civita symbols; the above expression simplifies to:

$$\begin{aligned} \langle \hat{\sigma}_x \rangle &= x, \\ \langle \hat{\sigma}_y \rangle &= y, \\ \langle \hat{\sigma}_z \rangle &= z, \end{aligned} \tag{46}$$

where x, y and z are the coordinates of the Bloch vector $\vec{r}$ that uniquely identifies the state $\hat{\rho}$. Hence, if we devise a measurement scheme capable of evaluating these three quantities we have successfully reconstructed the state of the qubit.

In particular we want to perform projective measurements [105, 108]. In a projective measurement we choose an orthonormal basis of the Hilbert space containing the states that define $\hat{\rho}$, in our case this is the computational basis $\{|0\rangle, |1\rangle\}$.

The measurement process consists in projecting the state on the chosen basis by means of the orthogonal projectors $\hat{\Pi}_0 = |0\rangle\langle 0|$ and $\hat{\Pi}_1 = |1\rangle\langle 1|$. The measurement result are the probabilities of $\hat{\rho}$ collapsing on the different basis states, in our case p_0 and p_1. These quantities are given by:

$$p_i = \langle \hat{\Pi}_i \rangle = Tr(\hat{\Pi}_i\hat{\rho}), \tag{47}$$

note that the completeness of the Hilbert space ensures that $\sum_i p_i = 1$.

Provided that we are able the project on the computational basis, the outcome probabilities can be determined to an arbitrary precision by repeating the measurement on N copies of the state.

In particular we have:

$$p_0 = \frac{N_0}{N}, \;\; p_1 = \frac{N_1}{N}; \tag{48}$$

where N_0 and N_1 are the number of events where $\hat{\rho}$ has collapsed on $|0\rangle$ or $|1\rangle$, respectively. Coming back to our original problem of determining the qubit's state, if we take the z coordinate and consider the spectral decomposition of $\hat{\sigma}_z$ (see Eqs.(23)), we have:

$$\begin{aligned} z = \langle\hat{\sigma}_z\rangle = Tr[(|0\rangle\langle 0| - |1\rangle\langle 1|)\hat{\rho}] = \\ = Tr(|0\rangle\langle 0|\hat{\rho}) - Tr(|1\rangle\langle 1|\hat{\rho}) = p_0 - p_1. \end{aligned} \tag{49}$$

Hence, z can be determined performing a projective measurement on N copies of $\hat{\rho}$ in the computational basis, whereby:

$$z = \frac{N_0 - N_1}{N}. \tag{50}$$

The two remaining coordinates may be determined in a similar manner, in fact if we now consider the spectral decompositions of $\hat{\sigma}_x$ and $\hat{\sigma}_y$, proceeding in the same manner as we did for $\hat{\sigma}_z$, we obtain:

$$x = \langle\hat{\Pi}_+\rangle - \langle\hat{\Pi}_-\rangle = p_+ - p_- \tag{51}$$

$$y = \langle\hat{\Pi}_{+i}\rangle - \langle\hat{\Pi}_{-i}\rangle = p_{+i} - p_{-i}, \tag{52}$$

where $\hat{\Pi}_\pm = |\pm\rangle\langle\pm|$ and $\hat{\Pi}_{\pm i} = |\pm i\rangle\langle\pm i|$. With this we conclude that each of the coordinates (x, y, z) can be obtained performing a projective measurement in the basis that diagonalizes the corresponding Pauli operator.
If we now take the two unitary operations:

$$\hat{U}_x = \frac{1}{\sqrt{2}}\begin{pmatrix} 1 & 1 \\ 1 & -1 \end{pmatrix}, \quad \hat{U}_y = \frac{1}{\sqrt{2}}\begin{pmatrix} 1 & i \\ i & 1 \end{pmatrix} \tag{53}$$

and we apply them to the states of the computational basis we have:

$$\begin{aligned} &\hat{U}_x|0\rangle = |+\rangle, \;\; \hat{U}_x|1\rangle = |-\rangle, \\ &\hat{U}_y|0\rangle = |+i\rangle, \;\; \hat{U}_y|1\rangle = i|-i\rangle. \end{aligned} \tag{54}$$

We may use this fact to rewrite the expressions for x and y in terms of a measurement in the computational basis. Before doing so, we must recall that the under the action of a unitary $\hat{U}$ density operators transform according to the rule:

$$\hat{\rho}' = \hat{U}\hat{\rho}\hat{U}^\dagger. \tag{55}$$

We can now rewrite the outcome probabilities $p_\pm$ and $p_{\pm i}$ as follows:

$$\begin{aligned} p_+ &= Tr(|+\rangle\langle +|\hat{\rho}) = Tr(\hat{U}_x|0\rangle\langle 0|\hat{U}_x^\dagger\hat{\rho}) = Tr(|0\rangle\langle 0|\hat{\rho}^{(x)}) \\ p_- &= Tr(|-\rangle\langle -|\hat{\rho}) = Tr(\hat{U}_x|1\rangle\langle 1|\hat{U}_x^\dagger\hat{\rho}) = Tr(|1\rangle\langle 1|\hat{\rho}^{(x)}) \\ p_{+i} &= Tr(|+i\rangle\langle +i|\hat{\rho}) = Tr(\hat{U}_y|0\rangle\langle 0|\hat{U}_y^\dagger\hat{\rho}) = Tr(|0\rangle\langle 0|\hat{\rho}^{(y)}) \\ p_{-i} &= Tr(|-i\rangle\langle -i|\hat{\rho}) = Tr(\hat{U}_y|1\rangle\langle 1|\hat{U}_y^\dagger\hat{\rho}) = Tr(|1\rangle\langle 1|\hat{\rho}^{(y)}), \end{aligned} \tag{56}$$

where $\hat{\rho}^{(x)}$ and $\hat{\rho}^{(y)}$ are the states obtained applying the inverses of $\hat{U}_x$ and $\hat{U}_y$ to the original density operator $\hat{\rho}$. In these terms the coordinates of the Bloch vector can be determined using a system that first applies a unitary operation to the state and then projects it on the computational basis:

$$x = \frac{N_0^{(x)} - N_1^{(x)}}{N_0^{(x)} + N_1^{(x)}} \tag{57}$$

$$y = \frac{N_0^{(y)} - N_1^{(y)}}{N_0^{(y)} + N_1^{(y)}} \tag{58}$$

$$z = \frac{N_0^{(z)} - N_1^{(z)}}{N_0^{(z)} + N_1^{(z)}}. \tag{59}$$

Here with the superscripts x, y and z we mean the number of "0" or "1" outcomes when the projection is performed on $\hat{\rho}^{(x)}$, $\hat{\rho}^{(y)}$ and $\hat{\rho}$, respectively.
This approach not only allows us to retrieve the state of a single qubit: in fact it constitutes the fundamental unit for a scheme capable of reconstructing the state of a register of many qubits. In fact, the state of a register n qubits can be written in terms of a tensor product of the Pauli operators relative to the local Hilbert subspaces associated to each qubit:

$$\hat{\rho} = \sum_{i_0,i_1,\ldots,i_{n-1}} a_{i_0,i_1,\ldots,i_{n-1}} \hat{\sigma}_{i_0} \otimes \hat{\sigma}_{i_1} \otimes \ldots \otimes \hat{\sigma}_{i_{n-1}}, \tag{60}$$

where each $i_k \in \{0, x, y, z\}$ and $\hat{\sigma}_0 = \mathbb{I}$. We see that Eq.(26) is a particular case of the above expression where $a_0 = \frac{1}{2}$ and the remaining coefficients equal the coordinates of the Bloch vector $\vec{r}$ divided by 2.
Similarly to the case of a single qubit, the coefficients appearing in Eq.(60) are related to the expectation value of a tensor product of Pauli operators.
In fact:

$$\begin{aligned}
&\langle \hat{\sigma}_{j_0} \otimes \ldots \otimes \hat{\sigma}_{j_{n-1}} \rangle = Tr(\hat{\sigma}_{j_0} \otimes \ldots \otimes \hat{\sigma}_{j_{n-1}} \hat{\rho}) = \\
&= \sum_{i_0,\ldots,i_{n-1}} a_{i_0,\ldots,i_{n-1}} Tr(\hat{\sigma}_{j_0}\hat{\sigma}_{i_0} \otimes \ldots \otimes \hat{\sigma}_{j_{n-1}}\hat{\sigma}_{i_{n-1}}) = \\
&= \sum_{i_0,\ldots,i_{n-1}} a_{i_0,\ldots,i_{n-1}} \prod_{k=0}^{n-1} Tr(\hat{\sigma}_{j_k}\hat{\sigma}_{i_k}),
\end{aligned}$$

again here the trace of $\hat{\sigma}_{j_k}\hat{\sigma}_{i_k}$ is non-vanishing if and only if $j_k = i_k$, in which case the product equals the 2×2 identity, thus the expectation value reduces to:

$$\langle \hat{\sigma}_{j_0} \otimes \ldots \otimes \hat{\sigma}_{j_{n-1}} \rangle = 2^n a_{j_0,j_1,\ldots,j_{n-1}}, \tag{61}$$

where the coefficient $a_{0\ldots 0}$ must always be equal to $\frac{1}{2^n}$ as $\langle \mathbb{I} \rangle = 1$ for any state. The state of the n-qubits is determined by the coefficients $a_{j_0,j_1,...,j_{n-1}}$, which in a sense play a role similar to one of the coordinates of the Bloch vector for a single qubit. However, as it can be seen from the left-hand side of Eq. (61), the coefficients of the expansion are related to the correlation of n Pauli operators. Therefore, in order to reconstruct $\hat{\rho}$ in this case we must adopt a scheme where, given many copies of the state, for each coefficient of the expansion (Eq.(60)) we perform a joint projective measurement where a set of unitary operations $\hat{U}_0$, $\hat{U}_1$, ..., $\hat{U}_{n-1}$ is applied to each qubit before measuring it in the local computational basis [109].

3.3.5 Entanglement

Let us consider two parties Alice and Bob sharing the components of a bipartite quantum system. The state of such a system lives in a composite Hilbert space $\mathcal{H}_{AB}$, whose structure consists of a tensor product of the subspaces $\mathcal{H}_A$ and $\mathcal{H}_B$.
A bipartite system in a pure state is said to be *separable* if and only if it can be written as:

$$|\Psi\rangle_{AB} = |\varphi\rangle_A \otimes |\gamma\rangle_B, \tag{62}$$

where $|\varphi\rangle_A \in \mathcal{H}_A$ and $|\varphi\rangle_B \in \mathcal{H}_B$.
When this is not possible, the state is *entangled.*
The concept of separability can be extended to the case of mixtures of quantum states. A system in a statistical mixture of states is separable if it exists an ensemble of separable states of $\mathcal{H}_{AB}$ $\{|a,b\rangle\}$ and a probability distribution $P(a,b)$ such that the density operator associated to the mixture takes the form:

$$\hat{\rho} = \sum_{a,b} P(a,b)|a,b\rangle\langle a,b|. \tag{63}$$

According to this definition, a bipartite system in a mixed state is entangled if its density operator cannot be written as a mixture of states which are exclusively separable.

At this point let us consider the case where $dim(\mathcal{H}_A) = dim(\mathcal{H}_B) = 2$. In this case Alice and Bob share a system of two qubits with local computational bases: $\{|0\rangle_A, |1\rangle_A\}$ and $\{|0\rangle_B, |1\rangle_B\}$, which generate the joint 2-qubit computational basis: $\{|00\rangle_{AB}, |01\rangle_{AB}, |10\rangle_{AB}, |11\rangle_{AB}\}$.

In this context we may take into account the four entangled states:

$$
\begin{aligned}
|\phi^+\rangle &= \frac{1}{\sqrt{2}}(|00\rangle_{AB} + |11\rangle_{AB}),\\
|\phi^-\rangle &= \frac{1}{\sqrt{2}}(|00\rangle_{AB} - |11\rangle_{AB}),\\
|\psi^+\rangle &= \frac{1}{\sqrt{2}}(|01\rangle_{AB} + |10\rangle_{AB}),\\
|\psi^-\rangle &= \frac{1}{\sqrt{2}}(|01\rangle_{AB} - |10\rangle_{AB}).
\end{aligned}
\tag{64}
$$

These states are known as *EPR states* [110] or *Bell states*. Bell states constitute a basis of $\mathcal{H}_{AB}$, hence any two-qubit state can be expressed as a superposition of these states. Among all entangled states, Bell states stand out for their property of being *maximally entangled*.

In a maximally entangled state, the reduced density operators describing Alice' and Bob's qubits are completely mixed, *i.e.* $\hat{\rho}_A = \hat{\rho}_B = \frac{\mathbb{I}}{2}$. This reflects the fact that a description of one of the parties of an entangled state that prescinds from knowledge on the complete state is not possible without a certain degree of classical uncertainty. For a maximally entangled state this uncertainty is the largest possible, as the reduced state can be understood as a mixture of any pair of orthogonal states with equal probability.

As we have already seen, two-qubit gates introduce an interaction among qubits. In particular controlled gates such as the CNOT are capable of generating entanglement. This is achieved by the circuit shown in Fig.(5). Here Alice' and Bob's qubits correspond to the upper and lower line, respectively. The circuit can be broken down in two steps: the first one consists in the action of an Hadamard gate on Alice' qubit, the second is the action of a CNOT gate on the joint Alice-Bob state. Under the action of this circuit, the states of the two-qubit computational basis are transformed into the

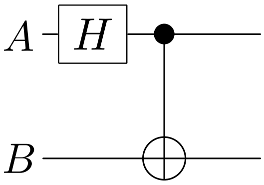

Figure 5: An Hadamard gate acts on Alice' qubit, then a CNOT gate is applied to the joint state. The circuit transforms states of the computational basis into the Bell basis. By running the circuit from right to left the inverse transformation is performed.

Bell states as follows:

$$\begin{aligned}
|00\rangle_{AB} &\xrightarrow{\hat{H}_A} \left(\frac{|0\rangle + |1\rangle}{\sqrt{2}}\right)_A \otimes |0\rangle_B \xrightarrow{CNOT_{AB}} |\phi^+\rangle_{AB}, \\
|01\rangle_{AB} &\xrightarrow{\hat{H}_A} \left(\frac{|0\rangle + |1\rangle}{\sqrt{2}}\right)_A \otimes |1\rangle_B \xrightarrow{CNOT_{AB}} |\psi^+\rangle_{AB}, \\
|10\rangle_{AB} &\xrightarrow{\hat{H}_A} \left(\frac{|0\rangle - |1\rangle}{\sqrt{2}}\right)_A \otimes |0\rangle_B \xrightarrow{CNOT_{AB}} |\phi^-\rangle_{AB}, \\
|11\rangle_{AB} &\xrightarrow{\hat{H}_A} \left(\frac{|0\rangle - |1\rangle}{\sqrt{2}}\right)_A \otimes |1\rangle_B \xrightarrow{CNOT_{AB}} |\psi^-\rangle_{AB}.
\end{aligned}$$

Since both $\hat{H}$ and CNOT are self-inverse, these transformations can be inverted simply by reversing the order of the two stages of the circuit.

Entanglement is not merely a mathematical property of composite quantum systems, but can be regarded as a fundamental resource for quantum information processing. While the generation of entangled states entails a physical and operational cost, their availability enables information-theoretic tasks that cannot be achieved using local quantum operations and classical communication alone.
One prominent example is quantum teleportation [111], which allows the faithful transfer of an arbitrary quantum state between spatially separated laboratories without direct quantum interaction. By consuming a shared entangled pair and exchanging classical information, the quantum state is reconstructed at the receiver's location, demonstrating how entanglement can reduce the requirements for quantum communication channels.
Entanglement further enables entanglement swapping [112], whereby entanglement can be established between parties that have never directly interacted. By successively consuming entangled pairs at intermediate nodes, this mechanism allows entanglement to be distributed across extended networks. This principle forms the basis of quantum repeater architectures [113], which aim to distribute entanglement over long distances while mitigating the detrimental effects of loss and noise.
Finally, entanglement plays a central role in quantum cryptography, particularly in entanglement-based quantum key distribution protocols such as E91 [114]. In these schemes, the use of entangled states provides intrinsic security guarantees, ensuring that any eavesdropping attempt can be detected and enabling the generation of provably secure cryptographic keys.

So far we have defined entanglement and we have seen a particular yet significant set of entangled states. We have shown a circuit capable of entangling two qubits and we have given an overview of the key role of entanglement for quantum information.
But given any state, how do we tell if it is entangled or not? And if it is entangled, how much? Answering both questions at the same time is nontrivial. In fact, the definition

only tells us that a state, pure or mixed, is entangled if and only if it is not possible to write it as a separable one. If we adopt only this as a criterion we might be able to exclude separability of a given state, however we cannot say if the state in question is more or less entangled than another one.
Instead, we would like to have an observable quantity, whose value depends on the state and can inform us about its entanglement content. Several criteria and entanglement quantifiers have been developed [115, 116, 117, 118, 119], here we discuss two of them: *Von Neumann entropy* and *entanglement of formation.*

Von Neumann Entropy
Given a quantum state represented by a density operator $\hat{\rho}$, its Von Neumann entropy is defined as:

$$\mathcal{S}(\hat{\rho}) = -Tr(\hat{\rho}\log\hat{\rho}). \tag{65}$$

$\mathcal{S}$ can be understood as a measure of the uncertainty of the state. In fact, let $\{\lambda_i\}$ be the eigenvalues of $\hat{\rho}$. Then $\mathcal{S}$ takes the form:

$$\mathcal{S}(\hat{\rho}) = -\sum_{i=1}^{k} \lambda_i \log \lambda_i, \tag{66}$$

with k equal to the dimension of the Hilbert space on which $\hat{\rho}$ is defined.
The right-hand side of the above equation is often denoted with $H(\lambda_1, ..., \lambda_k)$ and corresponds to the *Shannon entropy* of the ensemble $\{\lambda_i\}$. This quantity has been defined and used in classical information theory to quantify the degree of uncertainty present in a random variable [120].
To clarify this statement, we can consider a random variable x that may take a value from a discrete set $\{x_i\}$ with probabilities $\{p_i\}$. If the probability distribution for the values of x is such that only $p_n = 1$ for a given n, then the entropy associated to x is zero. Therefore, x has no uncertainty, which corresponds to the fact that x can only take the value x_n. On the other hand, if the distribution is such that $p_i = 1/N$ $\forall i$, then x can take any of its allowed values with equal probability, thus it is maximally uncertain. In fact, in this case H takes its maximum allowed value, which equals $\log N$. Any other distribution p_i is associated with a value of H strictly in between 0 and $\log N$.
Since $\mathcal{S}(\hat{\rho})$ is the Shannon entropy associated to the eigenvalues of $\hat{\rho}$, by analogy we can say that it quantifies the amount of classical uncertainty present in $\hat{\rho}$.
We notice that $\mathcal{S}(\hat{\rho})$ has the following properties:

- $\mathcal{S}(\hat{\rho}) = 0$ if and only if ρ represents a pure state. In fact, for any pure state $|\psi\rangle$ we have that $\hat{\rho} = |\psi\rangle\langle\psi|$ is already diagonal with only one eigenvalue $\lambda = 1$ and all others zero. Hence $\mathcal{S}(\delta) = -\lambda\log\lambda = -1 \cdot \log 1 = 0$.
- $\mathcal{S}(\hat{\rho})$ does not change under unitary transformations of $\hat{\rho}$. This can be seen by the fact that for any unitary $\hat{U}$, $\hat{\rho}$ and $\hat{U}\hat{\rho}\hat{U}^\dagger$ have the same eigenvalues.
- $0 \leq \mathcal{S}(\hat{\rho}) \leq \log N$, with the extremes taken for pure and completely mixed states.

> This descends from the properties of $H(\lambda_1, ..., \lambda_k)$. If $\mathcal{S}$ saturates its maximum we have $\lambda_i = \frac{1}{N}\ \forall i$, thus $\rho = \frac{1}{N}\sum_i |\lambda_i\rangle\langle\lambda_i|$. Since the eigenstates $|\lambda_i\rangle$ are an orthonormal basis we have the completeness relation $\sum_i |\lambda_i\rangle\langle\lambda_i| = \mathbb{I}$, hence $\hat{\rho}$ is completely mixed.

Earlier in this section we stated that if we have a bipartite system in a pure entangled state we cannot describe any of the two subsystems in terms of a pure state $|\psi_{AB}\rangle$.
In other terms, although the overall state has no classical uncertainty, as in fact $\mathcal{S}(|\psi_{AB}\rangle\langle\psi_{AB}|) = 0$, both A and B must feature an uncertainty.
This means that the entropies of the reduced density operators $\mathcal{S}(\hat{\rho}_A)$ and $\mathcal{S}(\hat{\rho}_B)$ must be strictly greater than zero. Furthermore, it can be shown that $\mathcal{S}(\hat{\rho}_A)$=$\mathcal{S}(\hat{\rho}_B)$, so it is sufficient to check only one of the two subsystems.
This suggests a criterion to certify entanglement of a pure state: given the overall density matrix $\hat{\rho}_{AB} = |\psi_{AB}\rangle\langle\psi_{AB}|$, if $\mathcal{S}(\hat{\rho}_A) \neq 0$ or $\mathcal{S}(\hat{\rho}_B) \neq 0$, then $|\psi_{AB}\rangle$ is entangled.

We must stress again the fact that Von Neumann entropy works only for pure states. To show this we can consider a simple example: let us take a two-qubit system in the mixed state:

$$\hat{\rho}_{AB} = \frac{1}{2}(|00\rangle\langle 00| + |11\rangle\langle 11|). \tag{67}$$

If we perform the partial traces over the two subsystems we have $\hat{\rho}_A = \hat{\rho}_B = \frac{\mathbb{I}}{2}$, which are completely mixed states so $\mathcal{S}(\hat{\rho}_{A(B)}) = \log 2$. According to the criterion for pure states $\hat{\rho}_{AB}$ should then be maximally entangled, but this is far from true as $\hat{\rho}_{AB}$ is a statistical mixture of the separable states $|00\rangle$ and $|11\rangle$ and as such not entangled by definition.

Entanglement of formation
Von Neummann entropy is not suited to quantify entanglement when applied to the case of mixed states. However, it is possible to use $\mathcal{S}$ to define a different quantifier capable of telling if a state is entangled even when it can only be described by a statistical mixture.
To do so, we start again from the form taken by the density operator of a bipartite system:

$$\hat{\rho} = \sum_i p_i |\Psi_i\rangle\langle\Psi_i|, \tag{68}$$

where $\{|\Psi_i\rangle\}$ is an ensemble of states of the composite Hilbert space and p_i is a probability distribution. Such a decomposition for $\hat{\rho}$ is not unique and this observation is crucial in order to define to a proper entanglement quantifier.
For instance let us consider the two-qubit mixed state:

$$\hat{\rho} = \frac{1}{2}(|\phi^-\rangle\langle\phi^-| + |\phi^+\rangle\langle\phi^+|). \tag{69}$$

Written in this way the state appears as a statistical mixture of the $|\phi^{\pm}\rangle$ states with equal probabilities of $\frac{1}{2}$.
Operatively speaking it might be reasonable to think that to produce the state one has

to spend resources in "building" the two Bell states, hence this resources should be found again in the state in terms of entanglement. However by writing the Bell states in terms of the computational basis and carrying out the tensor products it is possible to show that the state of Eq.(69) is exactly the state of Eq.(67), which as we have already state is not entangled.

If we keep reasoning in terms of resources we might justify this fact by saying that indeed if one has the resources to produce the entangled states of the mixture we can generate $\hat{\rho}$, however we can achieve the same result employing less resources *i.e.* using separable states. Therefore, a good entanglement quantifier for mixtures should inform us about the *minimum* amount of entanglement required to form the state.

To this aim, given a generic mixture of the form of Eq.(68), we can take the quantity:

$$\mathcal{E}(\hat{\rho}) = min\left(\sum_i p_i E(|\Psi_i\rangle\langle\Psi_i|)\right), \tag{70}$$

where $E(|\Psi_i\rangle\langle\Psi_i|)$, which from now on we call E_i, is the Von Neumann entropy of the reduced density operator associated to $|\Psi_i\rangle$. The minimization appearing in Eq. (70) is performed over all possible representations of $\hat{\rho}$ in terms of an ensemble of pure states. $\mathcal{E}(\hat{\rho})$ goes under the name of *entanglement of formation* [121] and according to its definition if $\hat{\rho}$ describes a pure state, then it reduces to the Von Neumann entropy of the state. If $\hat{\rho}$ is separable and not pure, by definition it can be written as a mixture of separable pure states, hence, all components E_i equal zero, thus $\mathcal{E}(\hat{\rho}) = 0$.

In any other case, since p_i is a probability and $0 \leq E_i \leq 1$, $\mathcal{E}$ takes values in the interval $(0, 1]$, with the case $\mathcal{E}(\hat{\rho}) = 1$ denoting a maximally entangled state.

Because of all the above reasons, $\mathcal{E}$ can quantify the amount of entanglement of any bipartite system.

A crucial part of the evaluation of this parameter is the minimization over the statistical ensembles that can realize $\hat{\rho}$, this operation is generally demanding in the sense that, depending on the dimensionality of the two subsystems, it might not have an analytically closed form.

For a system of two qubits, $\mathcal{E}(\hat{\rho})$ has a functional representation in terms of $\hat{\rho}$ [122] which is given by:

$$\mathcal{E}(\hat{\rho}) = h\left(\frac{1+\sqrt{1-C^2(\hat{\rho})}}{2}\right), \tag{71}$$

where $C(\hat{\rho})$ is the *concurrence* associated to the state and $h(x)$ is the function:

$$h(x) = -x\log_2 x - (1-x)\log_2(1-x). \tag{72}$$

Concurrence measures how similar a state and its *spin-flipped* version are. For a single qubit in the state $|\psi\rangle = \alpha|0\rangle + \beta|1\rangle$ the spin-flipped state is defined as: $|\tilde{\psi}\rangle = \hat{\sigma}_y|\psi^*\rangle$, with $|\psi^*\rangle = \alpha^*|0\rangle + \beta^*|1\rangle$. For a spin-$\frac{1}{2}$ particle this operation corresponds to the standard time reversal operation and indeed flips the particle spin [123].

If we now consider a two qubit states represented by the density operator $\hat{\rho}$ its spin-flipped version is given by:

$$\hat{\tilde{\rho}} = (\hat{\sigma}_y \otimes \hat{\sigma}_y)\hat{\rho}^*(\hat{\sigma}_y \otimes \hat{\sigma}_y), \tag{73}$$

where $\hat{\rho}^*$ is the complex conjugated of $\hat{\rho}$. We can define the matrix $\hat{R} = \sqrt{\sqrt{\hat{\rho}}\hat{\tilde{\rho}}\sqrt{\hat{\rho}}}$, which has eigenvalues: λ_1, λ_2, λ_3 and λ_4, with $\lambda_1 \geq \lambda_2 \geq \lambda_3 \geq \lambda_4$. From this the Concurrence of $\hat{\rho}$ is defined as:

$$C(\hat{\rho}) = max\{0, \lambda_1 - \lambda_2 - \lambda_3 - \lambda_4\}. \tag{74}$$

With this we have an entanglement quantifier that can be easily applied to a system of two qubits without making any assumption on its purity.

4 Experimental setups

The main focus of this chapter is to present the experimental material we have developed and employed in this work in order to implement schemes capable of performing quantum computation and simulation tasks.

As already stated we employ a photonic approach. The starting point of this strategy is the generation of a state of light featuring quantum resources. To this aim we employ nonlinear optics: in particular, in section 4.1 we discuss the photon source based on spontaneous parametric down-conversion (for short SPDC) in a KTP waveguide, which we used to generate the photon pairs employed in the experiments described in chapter 5

Once the resource state is generated, the next step is to devise a system where the state evolves in a controlled way. This is necessary in order to process the information encoded in the state and use it for any protocol of interest and it can be achieved adopting several strategies, each of which is based on how information is codified. To this aim of the degrees of freedom possessed by photons can be used, in this work we focus on two strategies: path encoding and time multiplexing. In sections 4.2 and 4.3 we describe the two systems used to perform the experiments described in this work.

The remaining block necessary for photonic based quantum information encoding and processing is the readout of information. This is achieved by detecting photons after they have undergone the desired evolution, whereby the detection scheme typically varies in function of the specific measurement that one desires to implement. In section 4.4 we show the tomographic detection setup that we have built in order perform the reconstruction of two-qubit states in our time-multiplexed platform.

4.1 Photon Source

There is no photonic quantum computation without photons, therefore this section aims at describing the photon source used in this work.

To do this we start illustrating the physical process that we employ to generate photons.

Afterward, we describe the source setup which is based on a non-linear waveguide. The waveguide and part of the setup used, namely the time-multiplexed pump laser, were preexisting to this work and have been described in [124]. Therefore, here we focus only on the process optimization that followed the waveguide realignment. Although we do not re-describe in depth setup sections that have been developed before, we will restate some key information required for the comprehension of what has been done here.

4.1.1 Photon generation via nonlinear optics: Spontaneous Parametric Down Conversion

We generate photons using Type-II SPDC, a three wave mixing process taking place in a $\chi^{(2)}$ non-linear optical medium whose detailed description can be found in the corresponding chapter of [125]. In this process a pump photon decays into two photons, often called *signal* and *idler* [126], with orthogonal polarizations. This effect is mediated by the dipoles inside the optical medium and follows an Hamiltonian with form:

$$\hat{H} = \Gamma \hat{a}_p \hat{a}_s^\dagger \hat{a}_i^\dagger + \Gamma^* \hat{a}_p^\dagger \hat{a}_s \hat{a}_i, \tag{75}$$

where $\hat{a}_p^\dagger$, $\hat{a}_s^\dagger$ and $\hat{a}_i^\dagger$ are the photonic creation operators relative to pump, signal and idler with the respective annihilation operators $\hat{a}_p$, $\hat{a}_s$ and $\hat{a}_i$. The complex constant Γ appearing in $\hat{H}_{SPDC}$ depends on the process strength.

Using coherent light as pump, the interaction Hamiltonian can be rewritten substituting $\hat{a}_p$ with a constant, thus obtaining:

$$\hat{H} = \gamma \hat{a}_s^\dagger \hat{a}_i^\dagger + \gamma^* \hat{a}_s \hat{a}_i, \tag{76}$$

where γ is complex and depends both on Γ and the strength of the pump, in particular, $|\gamma|$ increases with the input pump power.

The evolution produced by this Hamiltonian is obtained according to Schrödinger's equation as:

$$\begin{aligned} |\Psi\rangle &= e^{-i\hat{H}} |0,0\rangle_{s,i} = \\ &= e^{-i(\gamma \hat{a}_s^\dagger \hat{a}_i^\dagger + \gamma^* \hat{a}_s \hat{a}_i)} |0,0\rangle_{s,i}, \end{aligned} \tag{77}$$

with $|0,0\rangle_{s,i}$ representing a state containing zero signal-idler photons. In the structure of the evolution operator we recognize the form of a two-mode squeezing operation, therefore $|\Psi\rangle$ is a two-mode squeezed vacuum state.

Before commenting on how this can be used to approximate the state of a pair of single photons, we must consider SPDC from a physical point of view and specify under

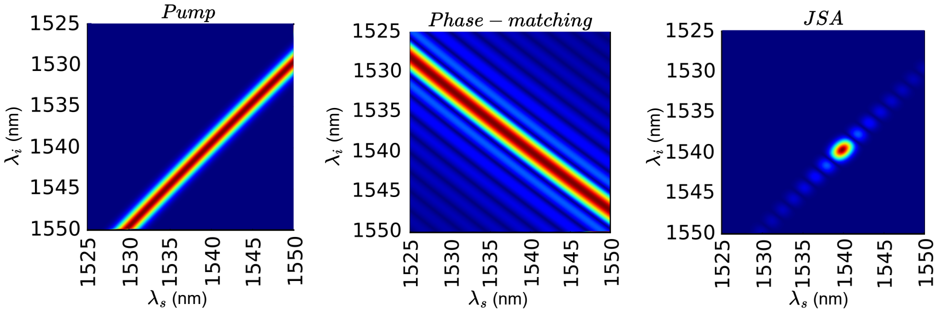

(a) (b) (c)

Figure 6: Simulated joint spectral amplitude for SPDC in ppKTP. The plots are adapted from [124]. **(a):** Pump distribution $\alpha(\omega_s, \omega_i)$. Because of energy conservation $\omega_s + \omega_i = \omega_p$, this combined with the pump spectrum results in a distribution of signal and idler frequencies that fulfil energy conservation. **(b):** Phase-matching distribution $\phi(\omega_s, \omega_i)$. This distribution arises from the fact that signal and idler must fulfil momentum conservation. This is not always possible due to dispersion, however using periodic poling it is possible to compensate for phase mismatching. **(c):** The Joint spectral amplitude dictates what signal and idler frequencies are permitted both by energy conservation and phase matching. This function is the product of pump and phase-matching distribution, the one shown here is degenerate as its central region corresponds to the point $\lambda_s = \lambda_i$.

which conditions the evolution operator looks like the one of Eq. (77).
SPDC must fulfill energy conservation, therefore the energies of signal and idler must add up to the pump energy, which in terms photon frequencies means:

$$\omega_p = \omega_s + \omega_i. \tag{78}$$

This gives rise to a pump distribution $\alpha(\omega_s, \omega_i)$ in the signal-idler spectral space resembling the one in Fig. 6a. The width of $\alpha(\omega_s, \omega_i)$ depends on the spectral width of the pump photons.
Secondly, SPDC fulfills momentum conservation, which means the following relation for the photon wave vectors:

$$\vec{k}_p = \vec{k}_s + \vec{k}_i, \tag{79}$$

which can again be translated in a requirement involving the photon frequencies:

$$n_p \omega_p \hat{k}_p = n_s \omega_s \hat{k}_s + n_i \omega_i \hat{k}_i, \tag{80}$$

where n_p, n_s and n_i are the refractive indices seen by pump, signal and idler, while $\hat{k}_p$, $\hat{k}_s$ and $\hat{k}_i$ represent the directions of each photon. This condition goes under the name of *phase matching condition*, naturally fulfilling it depends on the properties of the non-linear medium and is generally difficult if not impossible. This can be overcome using a technique known as *quasi-phase-matching*, to realize quasi-phase-matching the non-linear material must be periodically poled along the propagation direction of the pump, *i.e.* it must consist of a series of domains of thickness Λ featuring opposite spontaneous polarizations. This periodical inversion modifies the phase-matching condition adding a term $\Delta\vec{k}$ along the poling direction, thus:

$$\vec{k}_p = \vec{k}_s + \vec{k}_i + \Delta\vec{k}, \tag{81}$$

with $|\Delta\vec{k}| = \frac{2\pi}{\Lambda}$, therefore the poling period Λ can be used to compensate the phase mismatch, making also possible to have signal and idler photons emitted collinearly to the pump.

Similarly to what happens with the pump, material properties and periodic poling result in a phase matching distribution $\phi(\omega_s, \omega_i)$, an example of which is shown in Fig. 6b. Looking at an horizontal or vertical slice of $\phi(\omega_s, \omega_i)$ we would obtain a *sinc*−shaped distribution featuring a main peak and many side lobes. This structure is due to the fact that in order to obtain an output signal or idler field, contributions from the material dipoles must sum along the whole length of the material. Pump and phase-matching distributions define the spectral features of SPDC, *joint spectral amplitude* (JSA) is defined as:

$$f(\omega_s, \omega_i) = \alpha(\omega_s, \omega_i)\phi(\omega_s, \omega_i) \tag{82}$$

Using the JSA we can now write the SPDC Hamiltonian taking into account energy and momentum conservation [127, 128]:

$$\hat{H}_{SPDC} = r \int d\omega_s d\omega_i f(\omega_s, \omega_i)\hat{a}_s^\dagger(\omega_s)\hat{a}_i^\dagger(\omega_i) + h.c., \tag{83}$$

where now r only depends on the pump intensity and $\hat{a}_s^\dagger(\omega_s)$ and $\hat{a}_i^\dagger(\omega_i)$ create signal and idler photons at the specific frequencies ω_s and ω_i. In order to relate this Hamiltonian to the one of Eq. (76) we should take into account the Schmidt decomposition [115] of $f(\omega_s, \omega_i)$:

$$f(\omega_s, \omega_i) = \sum_{k=1}^{N} \lambda_k h_k(\omega_s) g_k(\omega_i), \tag{84}$$

where the sets of functions h_k and g_k can be interpreted as spectral modes for the signal and idler photons. With $f(\omega_s, \omega_i)$ decomposed in this way we may rewrite the Hamiltonian as:

$$\begin{aligned}\hat{H}_{SPDC} &= r \int d\omega_s d\omega_i \sum_{k}^{N} \lambda_k h_k(\omega_s) g_k(\omega_i)\hat{a}_s^\dagger(\omega_s)\hat{a}_i^\dagger(\omega_i) + h.c. = \\ &= \sum_{k}^{N} r\lambda_k \int d\omega_s h_k(\omega_s)\hat{a}_s^\dagger(\omega_s) \int d\omega_i g_k(\omega_i)\hat{a}_i^\dagger(\omega_i) + h.c. = \\ &= \sum_{k}^{N} \left(r_k \hat{A}_k^\dagger \hat{B}_k^\dagger + r_k^* \hat{A}_k \hat{B}_k \right),\end{aligned} \tag{85}$$

where $r_k = r\lambda_k$, $\hat{A}_k^\dagger = \int d\omega_s h_k(\omega_s)\hat{a}_s^\dagger(\omega_s)$ and $\hat{B}_k^\dagger = \int d\omega_i g_k(\omega_i)\hat{a}_i^\dagger(\omega_i)$.

The operators $\hat{A}_k^\dagger$ and $\hat{B}_k^\dagger$ can be interpreted as broadband creation operators, that generate signal and idler photons in the spectral modes h_k and g_k and in this sense $\hat{H}_{SPDC}$ can be seen as the sum of N two mode squeezing Hamiltonians with the same form as the one of Eq. (76).

This means that the general output of SPDC can be thought as a tensor product of N two-mode squeezed vacuum states, such tensor product depends on the shape of $f(\omega_s, \omega_i)$ which in turn can be tailored engineering pump and phase-matching distributions. In particular, it is possible to adjust $\alpha(\omega_s, \omega_i)$ and $\phi(\omega_s, \omega_i)$ to have a separable $f(\omega_s, \omega_i)$, *i.e.* one taking the form: $f(\omega_s, \omega_i) = h(\omega_s)g(\omega_i)$. In this case signal and idler can be only in a single spectral mode, and if h and g show the same functional dependence from the signal and idler frequencies, the process is said to be *degenerate*. The $f(\omega_s, \omega_i)$ for degenerate approximately single-mode SPDC looks like the one shown in Fig. 6c, where we observe a pronounced circular region with its absolute maximum located at the point $\omega_s = \omega_i$ (or equivalently $\lambda_s = \lambda_i$) and a series of smaller side-lobes due to the *sinc* shape of the phase-matching function. These side-lobes indicate that the process is not perfectly spectrally single-mode, however it is possible to eliminate this effect applying spectral filtering.

Provided that we have a separable and degenerate $f(\omega_s, \omega_i)$, the process is driven by the Hamiltonian: $\hat{H}_{SPDC} = r\hat{A}_s^\dagger\hat{A}_i^\dagger + r^*\hat{A}_s\hat{A}_i$. Therefore, in this case SPDC produces the two-mode squeezed vacuum state:

$$|\Psi\rangle_{SPDC} = \sqrt{1 - |\lambda|^2} \sum_{n=0}^{\infty} \lambda^n |n, n\rangle_{s,i}, \tag{86}$$

with $\lambda = e^{i\varphi}\tanh(r)$ and $|n, n\rangle_{s,i}$ representing the state of n signal and idler photons in the same spectral mode.

From this expression we see how contributions containing different numbers of photons depend on the parameter r, which in turn depends on the pump strength. An option to treat SPDC as a source of single photons is to adjust its pump power in order to suppress state contributions featuring more than one photon in the signal and idler modes. In order to state a condition for this to be the case, we start by considering that the mean number of photons present in both signal and idler is given by:

$$\langle n\rangle = (1 - |\lambda|^2) \sum_n |\lambda|^{2n} n = \frac{|\lambda|^2}{1 - |\lambda|^2}. \tag{87}$$

Inverting this relation and substituting the result in Eq. (86) we can write the probability of having k signal-idler photons in terms of the mean photon number:

$$p_k = \frac{\langle n\rangle^k}{(\langle n\rangle + 1)^{k+1}}. \tag{88}$$

To ensure that contributions with $k > 1$ are negligible we must run the process in a

regime where the ratio $\xi = \frac{p_{k>1}}{p_1}$ is sufficiently small.
Given the expression of p_k we can calculate ξ as follows:

$$\begin{aligned} \xi = \frac{\sum_{n=2}^{\infty} p_k}{p_1} &= \sum_{n=1}^{\infty} \frac{\langle n \rangle^k}{(\langle n \rangle + 1)^{k+1}} = \\ &= \frac{1}{1 - \frac{\langle n \rangle}{\langle n \rangle + 1}} - 1 = \langle n \rangle. \end{aligned} \tag{89}$$

Therefore setting a low enough mean photon number ensures that the probability of having two or more photons is negligible. Of course, we must not forget that this is a probabilistic process and reducing $\langle n \rangle$ means that also p_1 will be reduced in comparison to p_0, thus reducing the generation rate. This means that a balance among photon number statistic and generation rates must be found in order to ensure at the same time reasonable data acquisition times and good quality of the input state.

4.1.2 SPDC in ppKTP waveguide

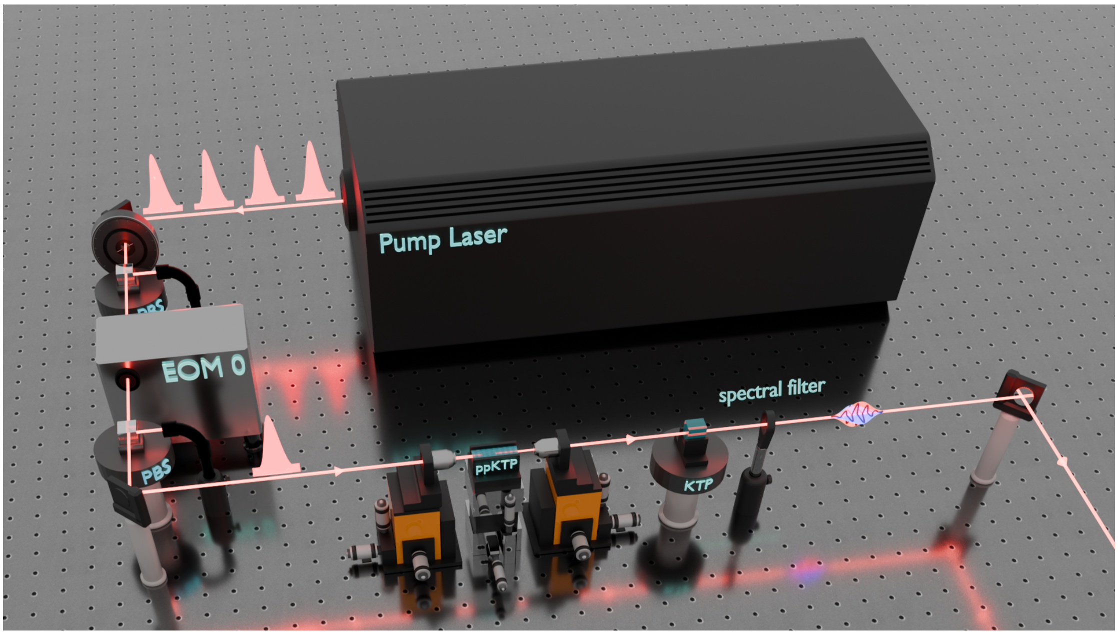

Figure 7: Sketch of the SPDC setup.

Our source is depicted in Fig. 7. We pump the process using coherent light pulses produced by a mode-locked Ti:sapph laser. Each emitted pulse has a duration in the order picoseconds, a center wavelength of $\lambda_p = 772.5\ nm$ and a spectral width of $\approx 0.3\ nm$. Since we perform degenerate SPDC we have $\omega_s = \omega_i = \frac{\omega_p}{2}$ and therefore both signal and idler have a central wavelength of 1545 nm. The laser cavity has a roundtrip time of 13.09 ns resulting in a repetition rate for the pulse train

$\nu_{laser} = 76.4\ MHz$, a photodiode located inside the cavity allows both monitoring the laser operation state and deriving an electrical signal with the same frequency as ν_{laser}. As it is clarified in subsection 4.3.5, we use this to generate all other signals required both for detection and setup operation.

In some of the experimental implementations described in this thesis, ν_{laser} must be reduced to match the desired experimental repetition rate ν_{exp}. This is achieved using an electro-optical modulator (EOM 0 in Fig. 7) in combination with two polarizing beam splitters. Using a $\frac{\lambda}{2}$-waveplate positioned before this pulse picking stage, we can set the amount of power transmitted to the nonlinear medium. After pulse picking and power adjustment, pump pulses encounter the nonlinear medium, which consists of a 25 mm long periodically poled potassium-titanyl-phosphate (ppKTP) waveguide. The waveguide has a size of 2 μm, therefore a lens with $f = 4.5\ mm$ is used to focus the pump and couple it to the waveguide.

The waveguide has an efficiency of $\approx 1.2\ dB/cm$, therefore, assuming that on average the generation takes place in the center of the waveguide, each photon exits it with a probability of 70%.

Since signal and idler are produced with orthogonal polarizations, birefringence in KTP induces a temporal walk-off between the two photons. We compensate this using an additional bulk unpoled KTP crystal with its optical axes rotated by 90° with respect to the ppKTP waveguides. The optimization of the length of the compensation crystal is provided in subsection 4.1.4. After being synchronized, the two photons pass through a bandpass spectral filter with FWHM of 1.8 nm and transmission of 90% at 1550.6 nm, used to eliminate the side lobes of the phase matching function in the signal-idler spectrum.

The optimization of this filter is provided in subsection 4.1.3.

4.1.3 Photon spectrum

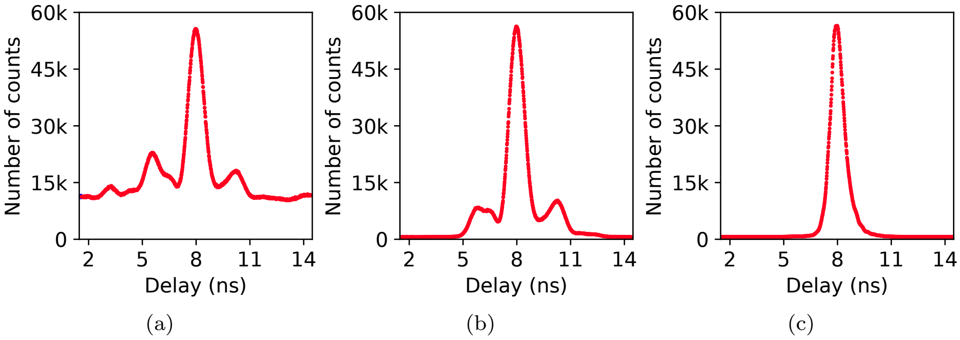

(a) (b) (c)

Figure 8: SPDC spectra: **(a)** when no spectral filtering is applied the spectrum obtained by a time-of-flight measurement shows a main peak and side lobes compatible with the behavior described for SPDC but with a strong background. **(b)** Applying a bandpass filter with 8 nm FWHM the background is suppressed but besides the main spectral peak we still see side lobes due to phase-matching. **(c)** Using a 1.8 nm FWHM filter we are able to suppress the side-lobes of the spectrum, which improves the photon spectral purity.

We want the photons produced by our SPDC to be indistinguishable and spectrally single mode. In order to have a single spectral mode, the JSA of the process must be separable, however we expect the JSA to be like the one of Fig. 6c, where the side-lobes of the phase-matching function hinder spectral separability. To confirm this we must devise a way to "see" the photon spectrum. We achieved this using a *time of flight* method [129]: signal and idler photons are separated and sent to two dispersive fibers where different wavelengths experience different delays. Therefore, we can obtain a readout of the photon spectrum by recording an histogram of the photon arrival times to the detector at the end of the dispersive fiber. For the fibers we use a relative delay of 1 ns corresponds to a wavelength difference of 0.862 nm.
We have seen that after the ppKTP waveguide we perform spectral filtering, now let us consider the unfiltered case where the photon spectrum is untouched. In this case, using the method described above, we obtain the spectrum of Fig. 8a, where we already see the behavior we were expecting from the JSA: a prominent central peak and lower phase matching peaks, but besides this we see a flat background coming from other fluorescence processes taking place in the waveguide substrate.
In order to apply spectral filtering and eliminate the side-lobes we would like to determine the width of the central peak. To do this we apply an intermediate bandpass filter with FWHM of 8 nm to remove the background. The effect of this filter can be observed in Fig. 8b, where we see that the background is no more present. The filter transmission window is centered adjusting the light incidence angle in order to maximize the central peak. In this loosely filtered spectrum we can still observe side peaks and having removed the background we are able to determine the main peak FWHM, which we find to be equal to 1.1 nm. At this point we apply an even narrower filtering using the 1.8 nm FWHM filter that was mentioned in the previous section. This filter has a transmission of 90% and as the other ones it is angle tuned to be centered onto the main peak, the recorded spectrum obtained with the final filter is show in Fig. 8c, where we finally see no side-lobes and the photons are now expected to be spectrally single mode. At this point what is left to ensure is photon indistinguishability.

4.1.4 Photon indistinguishability

Hong-Ou-Mandel (HOM) interference is a standard means of probing photon indistinguishability. First demonstrated by Hong *et al.* in [130], HOM interference in its original form can be observed when two indistinguishable photons impinge on a balanced beam splitter like the one shown in Fig. 9a. Since the beam splitter is balanced, the photonic creation operators associated to its inputs and outputs $\hat{a}^\dagger$ and $\hat{b}^\dagger$ evolve in the following manner:

$$\begin{aligned} \hat{a}^\dagger &\to \frac{\hat{a}^\dagger + \hat{b}^\dagger}{\sqrt{2}}, \\ \hat{b}^\dagger &\to \frac{\hat{a}^\dagger - \hat{b}^\dagger}{\sqrt{2}}. \end{aligned} \tag{90}$$

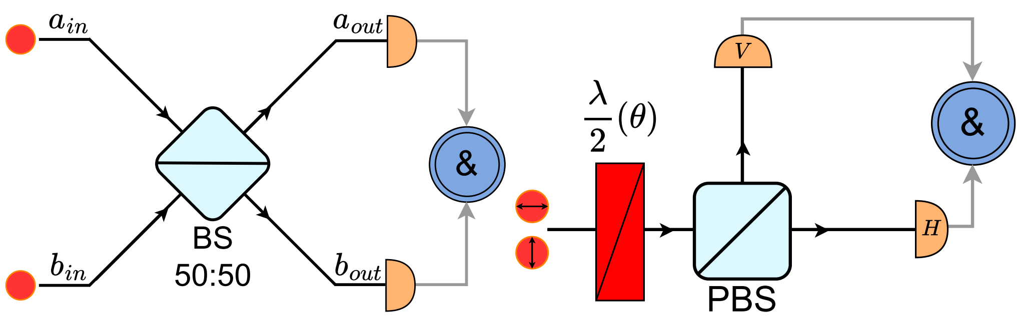

(a) (b)

Figure 9: **(a):** Hong-Ou-Mandel interference scheme. **(b):** Polarization Hong-Ou-Mandel interference scheme.

If the two photons are perfectly indistinguishable and enter the beam splitter as shown in Fig. 9a we can write their input state in the photon number basis as: $|\psi\rangle_{in} = |1\rangle_a|1\rangle_b = \hat{a}^\dagger\hat{b}^\dagger|\varnothing\rangle$, with $|\varnothing\rangle$ joint vacuum state for modes a and b. Following Eq. (90), the beam splitter transforms this state in the new one:

$$\begin{aligned} \hat{a}^\dagger\hat{b}^\dagger|\varnothing\rangle \rightarrow &\frac{1}{2}(\hat{a}^\dagger+\hat{b}^\dagger)(\hat{a}^\dagger-\hat{b}^\dagger)|\varnothing\rangle = \\ =&\frac{(\hat{a}^\dagger)^2-\hat{a}^\dagger\hat{b}^\dagger+\hat{b}^\dagger\hat{a}^\dagger-(\hat{b}^\dagger)^2}{2}|\varnothing\rangle = \frac{(\hat{a}^\dagger)^2-(\hat{b}^\dagger)^2}{2}|\varnothing\rangle = \\ =&\frac{|2\rangle_a|0\rangle_b-|0\rangle_a|2\rangle_b}{\sqrt{2}}, \end{aligned} \tag{91}$$

where we see that being the two particles indistinguishable, the terms containing a product of $\hat{a}^\dagger$ and $\hat{b}^\dagger$ cancel out leaving a state where photons bunch either on mode a or b. Since there are no state contributions of the form $|1\rangle_a|1\rangle_b$ we expect to see no coincidences between two detectors located at the outputs of the beam splitter.
If instead the two particles can be distinguished in one of their degrees of freedom, say for instance their arrival time, we have the following evolution:

$$\begin{aligned} \hat{a}_t^\dagger\hat{b}_{t+\tau}^\dagger|\varnothing\rangle \rightarrow &\frac{1}{2}(\hat{a}_t^\dagger+\hat{b}_t^\dagger)(\hat{a}_{t+\tau}^\dagger-\hat{b}_{t+\tau}^\dagger)|\varnothing\rangle = \\ =&\frac{\hat{a}_t^\dagger\hat{a}_{t+\tau}^\dagger-\hat{a}_t^\dagger\hat{b}_{t+\tau}^\dagger+\hat{b}_t^\dagger\hat{a}_{t+\tau}^\dagger-\hat{b}_t^\dagger\hat{b}_{t+\tau}^\dagger}{2}|\varnothing\rangle, \end{aligned} \tag{92}$$

where we imply that photons on mode a and b reach the beam splitter at times t and $t+\tau$, respectively.
In this expression the cancellation seen in Eq. (91) is not possible since in the creation operators in the two terms refer to different times. Hence, in the fully distinguishable case the same two detectors will be able to record coincidences between a and b. If we were able to scan the delay τ among the two photons while recording coincidences, we would expect a sharp transition from distinguishable and indistinguishable case

witnessed by the drop in coincidences. In all practical cases, photons feature a temporal distribution with finite width, which, for instance, for photons with a spectrum similar to the one of Fig. 8c this is expected to be almost Gaussian. In this case when the temporal profiles of the two photons are equal and perfectly overlapped we expect to be still in the fully indistinguishable case, conversely, if the temporal separation τ is large enough to have no significant overlap we will be again in the distinguishable case. Between the two extremes, there is an intermediate regime where the two temporal distributions will not be perfectly overlapped but still almost indistinguishable. As we can continuously go from the distinguishable to the indistinguishable case we expect to observe a smooth transition between being able to see coincidences to not seeing them at all. This transition is commonly known as *HOM-dip* and its visibility, defined as:

$$V_{HOM} = \frac{C(\tau \to \infty) - C(\tau = 0)}{C(\tau \to \infty)}, \tag{93}$$

serves as an indistinguishability quantifier. $C(\tau = 0)$ and $C(\tau \to \infty)$ represent respectively coincidences when photons are perfectly synchronized and when their temporal separation is sufficiently large to distinguish them. In the ideal case $C(\tau = 0)$ is expected to be exactly zero, however this is the case only if the two photons have exactly the same temporal distribution.

Even if the two temporal profiles are perfectly equal, but the photons are partially distinguishable in another degree of freedom , this term is larger than zero.

Using this fact we can devise an HOM interference experiment where photons are temporally indistinguishable, but their polarization state can be used to perform HOM interference.

This is shown in Fig. 9b, where two photons in the joint polarization state $|H\rangle|V\rangle = \hat{a}_H^\dagger \hat{a}_V^\dagger |\varnothing\rangle$ pass through a $\frac{\lambda}{2}$-waveplate set at an angle θ resulting in the evolution for the creation operators:

$$\begin{aligned} \hat{a}_H^\dagger &\to \cos(2\theta)\hat{a}_H^\dagger + \sin(2\theta)\hat{a}_V^\dagger, \\ \hat{a}_V^\dagger &\to \sin(2\theta)\hat{a}_H^\dagger - \cos(2\theta)\hat{a}_V^\dagger. \end{aligned} \tag{94}$$

The input state will therefore evolve to:

$$\begin{aligned} \hat{a}_H^\dagger \hat{a}_V^\dagger |\varnothing\rangle \to &(\cos(2\theta)\hat{a}_H^\dagger + \sin(2\theta)\hat{a}_V^\dagger)(\sin(2\theta)\hat{a}_H^\dagger - \cos(2\theta)\hat{a}_V^\dagger)|\varnothing\rangle = \\ =&\{\cos(2\theta)\sin 2\theta((\hat{a}_H^\dagger)^2 - (\hat{a}_V^\dagger)^2) - [\cos^2(2\theta) - \sin^2(2\theta)]\hat{a}_H^\dagger \hat{a}_V^\dagger\}|\varnothing\rangle = \\ =&\sin 4\theta(|H\rangle|H\rangle - |V\rangle|V\rangle) - \cos 4\theta|H\rangle|V\rangle. \end{aligned} \tag{95}$$

After the waveplate, a polarizing beam splitter separates H and V photons and send them to two detectors. Here too we can record coincidences between the two outputs and following from Eq. (95) the probability of recording a coincidence is given by:

$$P_{HV}(\theta) = \cos^2(4\theta). \tag{96}$$

Therefore, scanning θ, coincidences are expected to oscillate between a maximum value and zero. In fact, for each value of θ which is an integer multiple of $\frac{\pi}{4}$, we have $P_{HV}(\theta) = 1$. For these values of θ the photon polarization is either left untouched or swapped up to a common phase, therefore the two photons remain perfectly distinguishable. If instead $\theta = (2n+1)\frac{\pi}{8}$, P_{HV} drops to zero. In this case the photon's polarization is always rotated to an even superposition of $|H\rangle$ and $|V\rangle$, therefore we will not be able to tell which photon is transmitted or reflected by the polarizing beam splitter. This renders the two particle perfectly indistinguishable and makes impossible to observe coincidences.
Also in this case we can calculate the degree of indistingushability from the interference visibility, which we define as: $V_{p-HOM} = 1 - \frac{C_{min}}{C_{max}}$.
In the following we refer to these two versions of HOM interference as *time* and *polarization* HOM. We conclude this section by showing the setups used to perform time and polarization HOM interference.

Time HOM

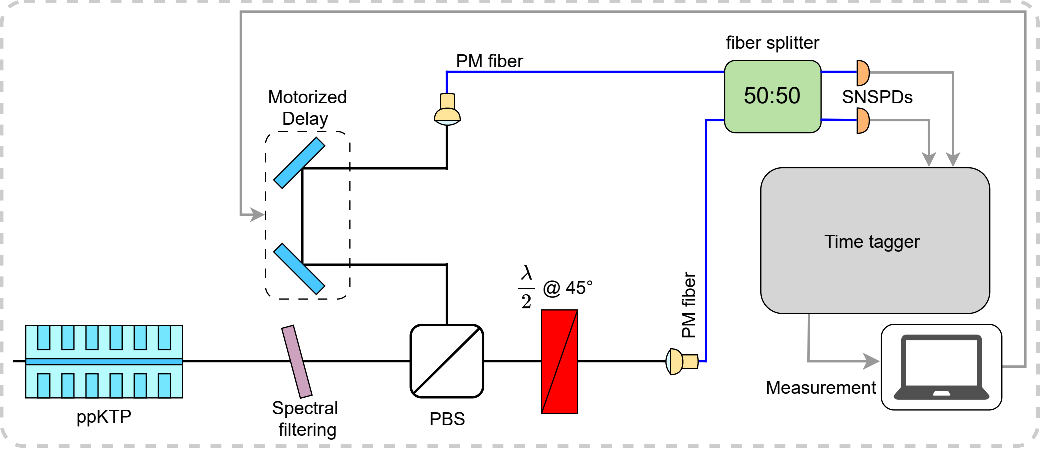

Figure 10: **Time-HOM setup:** Photon pairs form the source are separated by a polarizing beam splitter (PBS). The H-polarized photon goes through a waveplate that transforms its polarization to V before coupling it to a single mode polarization maintaining (PM) fiber. The V-polarized photon goes to a delay line before being coupled to a single mode PM fiber too. Both fibers are connected to a 50:50 PM splitter, whose outputs are connected to two SNSPDs. Using a time tagger and a computer we record coincidences between the two detectors as we vary the length of the delay line.

In order to perform time HOM interference using signal-idler pairs from the KTP waveguide we use the setup shown in Fig. 10. After being generated and spectrally filtered the two photons directly encounter a polarizing beam splitter without passing through the KTP compensation crystal. The polarizing beam splitter separates them and sends the $|H\rangle$ one to a $\frac{\lambda}{2}$-waveplate, while the $|V\rangle$ one is sent to a motorized delay line.
The waveplate is set with its axis at 45° in order to turn the $|H\rangle$ photon into $|V\rangle$ and

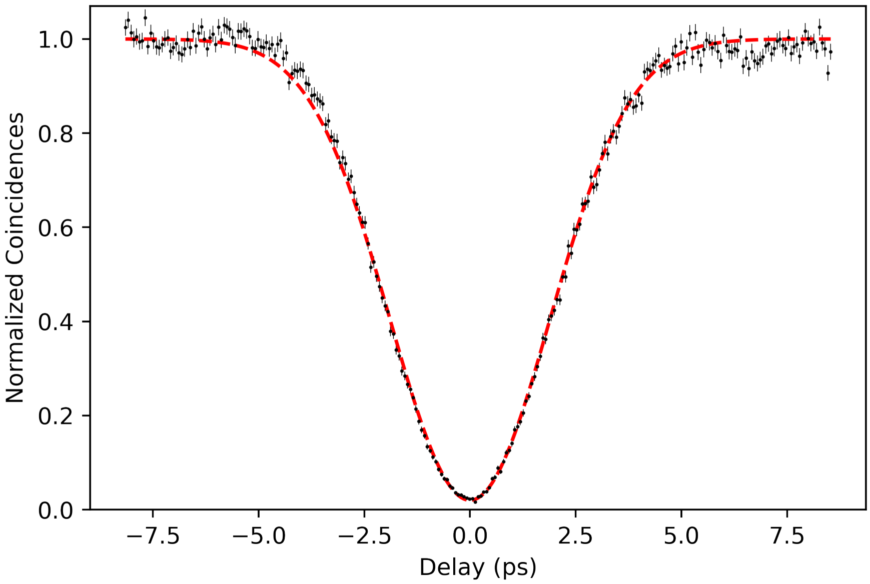

Figure 11: Using the setup shown in Fig. 10 we record the signal-idler time HOM dip obtaining a visibility of $(98.01 \pm 0.24)\%$.

ensures that signal and idler are indistinguishable in polarization. The motorized stage is used to vary the delay between the two particles and scan their temporal indistinguishability. Both photons are coupled into two polarization maintaining single mode fibers of the same length, which are connected to a 50:50 fiber splitter whose outputs are connected to two SNSPDs. Signals coming from the two detectors are sent to a time-tagger set to evaluate coincidences between the two detection channels. Using the motorized stage we scan the relative delay between the photons in discrete steps, for each delay we record the number of coincidences between the two detectors. The complete scan results in the plot shown in Fig. 11, which shows the normalized coincidences as a function of the delay. In order to calculate the interference visibility we fit a Gaussian function to the experimental data and we use the maximum and minimum of this function to evaluate V_{HOM} obtaining a measured visibility of $(98.01 \pm 0.24)\%$. This value signifies an excellent degree of indistinguishability for the two photons and shows how the source is operating at the degeneracy point.
As we have seen before, in the general source setup we also include a KTP compensation crystal to counteract the birefringence-induced temporal walk-off of signal and idler. On average photons are generated in the middle of the ppKTP waveguide and see only half of it, thus the expected length for the compensation crystal would be 12.5 mm. However, this assumption relies on the fact that the effective poled length coincides with the total length of the source. If this is not the case, a crystal 12.5 mm long would still be optimal only under the assumption that the

unpoled regions on both sides of the source have the same length. To test this and find the optimal length we use polarization HOM.

Polarization HOM

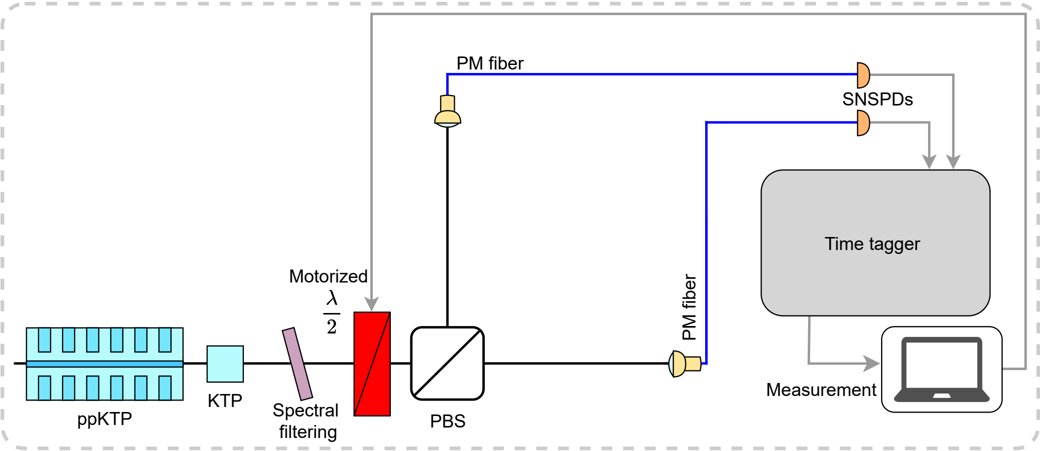

(a)

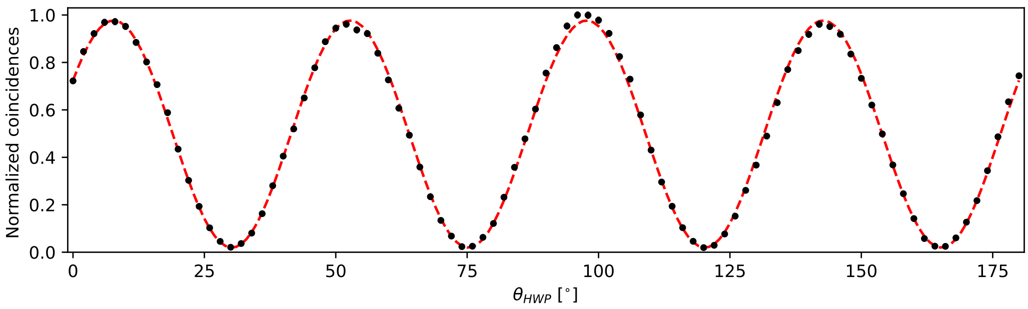

(b)

Figure 12: **(a):** Setup used to perform polarization HOM interference. In this setup we synchronize signal and idler using a KTP crystal positioned after the waveguide. The H-V photon pair goes through a motorized waveplate before impinging on a polarizing beam splitter. Two PM fibers collect photons coming from the polarizing beam splitter ports and route them to two SNSPDs. A time tagger and a computer collect coincidences between the two detectors while scanning the waveplate angle. **(b):** After finding the optimal length for the KTP compensation crystal we perform the polarization HOM scan shown in the plot finding a visibility of $(98 \pm 1)\%$.

We perform polarization HOM interference in the setup shown in Fig. 12. In this case, the KTP compensation crystal is positioned between waveguide and spectral filter. A PBS is used to separate H and V photons and send them to two SNSPDs connected to a time tagger. A motorized $\frac{\lambda}{2}$ positioned between spectral filter and PBS is used to scan the photon indistinguishability in polarization.

The KTP crystal must ensure a perfect temporal overlap of signal idler by compensating the walk-off from the waveguide. In order to optimize the crystal length

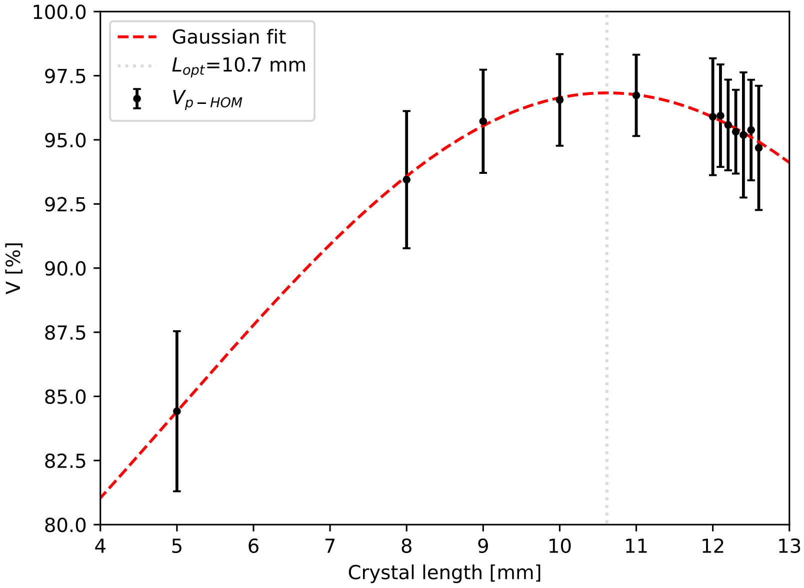

Figure 13: In order to optimize the length of the KTP compensation crystal we have performed polarization HOM in the setup shown in Fig. 12a, the plot shows interference visibility as a function of the crystal length. From a Gaussian fit we find that maximum visibility is expected for a length of 10.7 mm.

we have used KTP crystals of different lengths ranging from 5.0 mm to 12.6 mm and recorded the polarization HOM curve for each of them. From the different scans we obtain the visibilities shown in Fig. 13, which, following from Eq. (96), are calculated fitting a cos^2 function to the recorded coincidences. As the plot shows we find that photon indistinguishability increases for crystal lengths for 5 mm to 10 mm and then decreases again. As all the scans have been performed in the same experimental conditions in terms of spectral indistinguishability, the visibility trend is only due to the influence of the crystals on the temporal walk-off.

Fitting a Gaussian function to the points shown in Fig. 13 we find that the optimal HOM interference visibility is expected for a crystal length of 10.7 mm. Therefore, we acquired a KTP crystal of this length and performed a new scan of the two photon interference after a careful optimization of the source's spectral operation point. With this we obtain the interference trace shown in Fig. 12b, corresponding to a visibility of $(98 \pm 1)\%$ which is comparable to the one observed scanning the photon temporal delay. Thus, the 10.7 mm is correctly compensating the temporal indistinguishability induced by the waveguide birefringence.

4.2 Spatial multiplexing setup

At this point we present the system we have used in this work in order to realize of a path-encoded optical interferometer.
To this aim, we start by describing the concept behind path-encoding in optical implementations. After this we present the platform with a particular focus on how we can employ it to implement an Hadamard walk. We conclude this section by showing how in addition to the target unitary, we can program the network to implement a routing to a desired channel allowing an efficient readout of the network's output.

4.2.1 Implementing unitaries in path-encoded interferometers

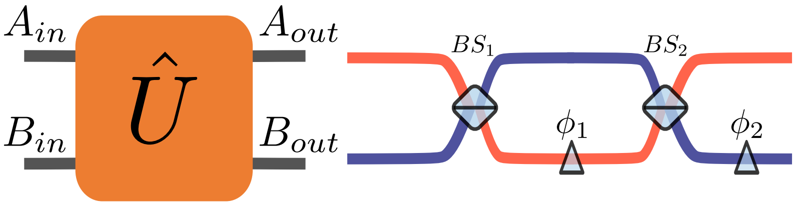

(a) (b)

Figure 14: **(a)**:2×2 path encoded unitary. **(b)**:Photonic implementation of a generic 2×2 path encoded unitary.

In this approach information is encoded in the path that a photon takes in entering and exiting an optical interferometer.
The minimal unit in this scheme is constituted by a system with two input and output modes as the one shown in Fig. 14a, where the input modes A_{in} and B_{in} are mapped to the two outputs A_{out} and B_{out} by the unitary operation $\hat{U}$.
In terms of quantum information, the $|0\rangle$ and $|1\rangle$ logical states are encoded by a single photon in the upper and lower mode, respectively.
In this context, $\hat{U}$ implements a generic single qubit gate and, as we have already seen in subsection 3.3.2, this can be achieved combining Hadamard and phase gates.
Translated into optical components this corresponds to the scheme shown in Fig. 14b, where BS_1 and BS_2 are 50:50 beam splitters and implement $\hat{H}$, whose action can be parametrized as follows:

$$\begin{aligned}\hat{MZ}(\phi_1,\phi_2) = \hat{\phi}_2\hat{BS}_2\hat{\phi}_1\hat{BS}_1 = \begin{pmatrix}1 & 0\\ 0 & e^{i\phi_2}\end{pmatrix}\frac{1}{\sqrt{2}}\begin{pmatrix}1 & 1\\ 1 & -1\end{pmatrix}\begin{pmatrix}1 & 0\\ 0 & e^{i\phi_1}\end{pmatrix}\frac{1}{\sqrt{2}}\begin{pmatrix}1 & 1\\ 1 & -1\end{pmatrix} = \\ = \frac{1}{2}\begin{pmatrix}1 & 0\\ 0 & e^{i\phi_2}\end{pmatrix}\begin{pmatrix}1+e^{i\phi_1} & 1-e^{i\phi_1}\\ 1-e^{i\phi_1} & 1+e^{i\phi_1}\end{pmatrix} = e^{\frac{\phi_1}{2}}\begin{pmatrix}1 & 0\\ 0 & e^{i\phi_2}\end{pmatrix}\begin{pmatrix}\cos\frac{\phi_1}{2} & -i\sin\frac{\phi_1}{2}\\ -i\sin\frac{\phi_1}{2} & \cos\frac{\phi_1}{2}\end{pmatrix}\end{aligned} . \tag{97}$$

Ignoring the global phase $\frac{\phi_1}{2}$, the rightmost matrix can be understood as the action of a variable beam splitter whose reflectivity is controlled by ϕ_1. The next operation

imparts a relative phase ϕ_2, which together with the variable beam splitter constitutes the most general operation between only two optical modes.
It has been shown by Reck *et. al.* [90] and by Clements *et. al.* [89] that it is possible to construct an interferomter of arbitrary size combining a sequence of beam splitters and phase shifters. In particular, following [89], in order to extend this approach to larger systems we may define the $N \times N$ operation:

$$\hat{T}_{n,m}(\phi_1,\phi_2) = \begin{pmatrix} 1 & 0 & \cdots & \cdots & \cdots & \cdots & 0 \\ 0 & 1 & & & & & \vdots \\ \vdots & & \ddots & & & & \vdots \\ \vdots & & & \hat{M}Z(\phi_1,\phi_2) & & & \vdots \\ \vdots & & & & \ddots & & \vdots \\ \vdots & & & & & 1 & 0 \\ 0 & \cdots & \cdots & \cdots & \cdots & 0 & 1 \end{pmatrix}, \tag{98}$$

which can be understood as $\hat{M}Z(\phi_1,\phi_2)$ applied only to mode n and m of the $N \times N$ system. In order to decompose any unitary operation $\hat{U}$ in terms of several applications of $\hat{T}_{n,m}$ we must take into account the fact that, as shown in [90], it is always possible to find values of ϕ_1 and ϕ_2 such that:

- $\hat{T}_{n,m}\hat{U}$ has an arbitrary zero element in its $n-th$ or $m-th$ row,
- $\hat{U}\hat{T}^{-1}_{n,m}$ has an arbitrary zero element in its $n-th$ or $m-th$ column,

therefore, $\hat{U}$ may be decomposed by successively applying $\hat{T}$ and $\hat{T}^{-1}$ from left and right to the original operation in order to nullify its lower (or upper) off-diagonal elements.
To show how this works, we might consider the case of a 3×3 operation, whereby the optical network would now be the one shown in Fig. 15, where at each crossing we have

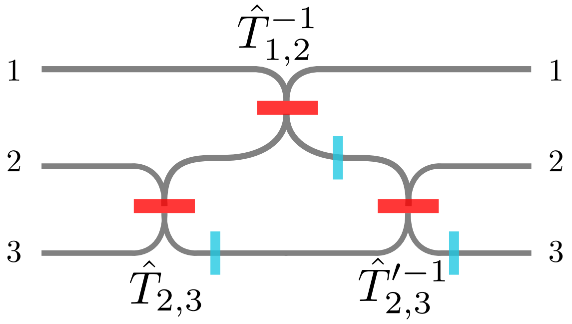

Figure 15: Configuration for a universal 3×3 interferometer

a unit cell parametrized by the aforementioned $\hat{M}Z$ operation, whereby the red horizontal bars represent a variable beam splitter and the vertical light blue bars a phase shifter. Given a 3×3 unitary we may look for phases such that:

1) $\hat{T}_{2,3}\hat{U}$ has its $(1,3)$ element equal to zero, which physically corresponds to set the splitting ratio and phase for the first unit cell between modes 2 and 3,

2) $\hat{T}_{2,3}\hat{U}\hat{T}^{-1}_{1,2}$ has its $(1,2)$ element equal to zero, which physically corresponds to set the splitting ratio and phase for the unit cell between modes 1 and 2,

2) $\hat{T}_{2,3}\hat{U}\hat{T}^{-1}_{1,2}\hat{T}'^{-1}_{2,3}$ has its $(2,3)$ element equal to zero, which physically corresponds to set the splitting ratio and phase for the second unit cell between modes 2 and 3,

where for brevity we omit the phase dependency in all $\hat{T}$ and $\hat{T}^{-1}$. Provided that the required phases are set we are left with the upper triangular matrix:

$$\hat{D} = \hat{T}_{2,3}\hat{U}\hat{T}^{-1}_{1,2}\hat{T}'^{-1}_{2,3} \tag{99}$$

and therefore we can rewrite $\hat{U}$ as:

$$\hat{U} = \hat{T}^{-1}_{2,3}\hat{D}\hat{T}'_{2,3}\hat{T}_{1,2}. \tag{100}$$

Since all the performed operations are unitary, $\hat{D}$ must be unitary too and since $\hat{D}$ must be both unitary and triangular, we must conclude the $\hat{D}$ is a diagonal matrix of the form: $\hat{D}_{i,j} = \delta_{i,j}e^{i\varphi_i}$. For any matrix $\hat{M}$ it is possible to show that $\hat{M}\hat{D} = e^{i\Delta}\hat{D}\hat{M} = \hat{D}'\hat{M}$, with $\hat{D}'$ of the same form of $\hat{D}$.

Hence, $\hat{U}$ can be finally written as:

$$\hat{U} = \hat{D}'\hat{T}^{-1}_{2,3}\hat{T}'_{2,3}\hat{T}_{1,2}. \tag{101}$$

This shows that the arrangement shown in Fig. 15 can implement any 3×3 unitary up to a diagonal matrix of phases $\hat{D}'$. These phases have no physical importance unless the output modes are interfered outside the network.

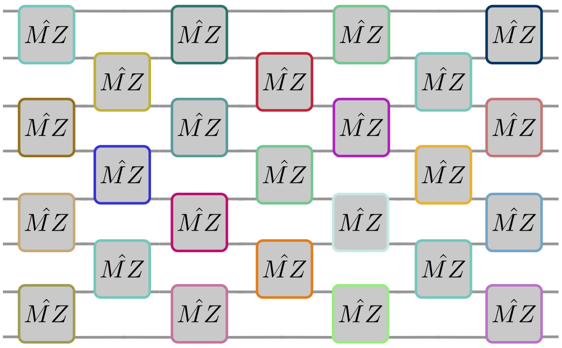

Figure 16: Interferometer realizing an N×N unitary combining multiple unit cells like the one of Fig. 14b.

This approach may be extended to any $N \times N$ optical network, which results in a rectangular arrangement of many 2×2 unit cells disposed across N layers like shown in Fig. 16, where each component represents a unit cell consisting of a variable beam splitter and a phase shifter.

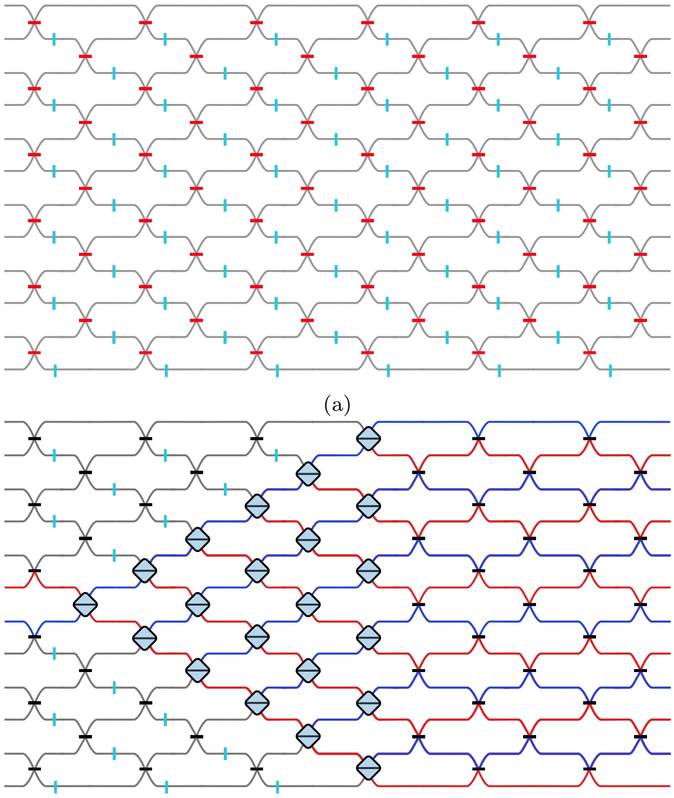

(a)

(b)

Figure 17: **(a):** Arrangement of the variable beam splitters and phase shifters within the 12×12 photonic network. Splitting ratios and phases are set thermally. The network uses a Clements scheme [89] to implement an arbitrary unitary operation. **(b):** Hadamard walk overlaid on the network structure. Given the system boundaries the walk is restricted to a maximum of six steps.

4.2.2 12x12 photonic processor

After discussing how a unitary transformation can be realized in an optical interferometer, now we present the platform used to perform some of the experiments that discussed in the next chapter.

The platform consists of a 12×12 photonic processor based on silicon nitride on insulator waveguides arranged as shown in Fig. 17a. The red and blue bars appearing at each mode crossing represent two thermal phase shifters that implement the unit cell of Eq. (97). The system features a total of 160 independent thermal phase shifters which can be set using a dedicated software provided by the vendor. In order to implement a unitary $\hat{U}$, each phase may be addressed individually. Alternatively, the software can automatically program all the phase shifters providing $\hat{U}$ as input of a routine that runs the decomposition discussed before.

Since phases are set thermally, the device is temperature stabilized by means of a closed-loop water-cooling system designed to keep the chip at a working temperature of $28°C$. All system parameters can be read out using the provided software. Optical

interfacing is provided via twelve input and output single-mode fibers.
The system features polarization sensitive losses and shows the highest transmission efficiency for vertically polarized input light.
For this reason, the input fibers are polarization maintaining as well as any external fibers used to feed light to the system. When the correct polarization is sent to the processor, it shows a total transmission efficiency of $\approx 50\%$.
In order to realize a path encoded Hadamard walk, since the system has a finite size it is not possible to implement an arbitrary large amount of steps without incurring in boundary effects. The unitary implemented by the system acts on a maximum of 12 input modes and the dimension of the Hilbert subspace occupied by the walk cannot exceed the number of available modes. Therefore, since $dim(\mathcal{H}_{QW}) = dim(\mathcal{H}_{pos}) \cdot dim(\mathcal{H}_{coin})$ and $dim(\mathcal{H}_{coin}) = 2$, the maximum dimension of the position subspace is limited to six.
This is shown in Fig. 17b where the 50:50 beam splitter network that implements the walk is overlaid to the processor schematics. From this figure we see that the two input coins need an initial redirection layer to be sent to the beam splitter that realizes the first step of the walk. After traversing six layers of beam splitters, the input light reaches the chip's boundaries and therefore the walk implemented by the network cannot exceed six steps. With this we have stated all the important properties of the chip, now we show how they can be exploited to not only implement the quantum walk unitary but also a routing that allows to prepare and measure the walk efficiently.

4.2.3 Unitary Routing

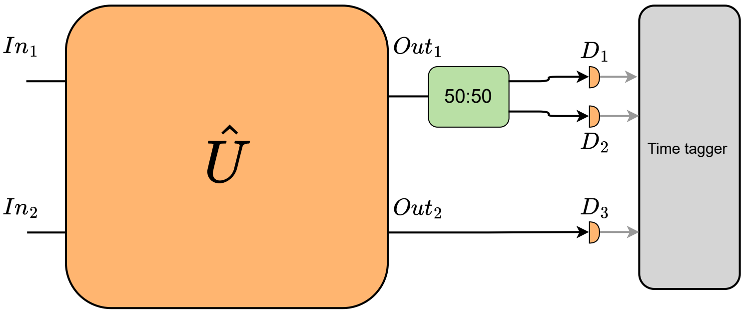

Figure 18: Unitary routing sketch. Detection of twofold events is possible programming the network to route the desired outputs to the ones physically connected to the detection unit.

In all the experiments we conducted with this platform, two photons produced by SPDC in the source described in 4.1.2 are sent to the photonic processor where they undergo a transformation. After the transformation we read out the outcome by evaluating two-fold coincidences among the network outputs, whereby we are interested both in events featuring photons on distinct modes as well as events where the two particles bunch on the same output.
In principle, this would require a setup with a dedicated detector for each output, where each detection unit can also distinguish the number of impinging photons.

For our experiments only three SNSPDs were available, which is enough to evaluate coincidences among two distinct outputs and self coincidences by means of probabilistic splitting. However, a way of reconnecting the network outputs to the detection is required in order to reconstruct the complete two-photon output.
Manual reconnection would be theoretically possible however undesirable as it would negatively impact on measurement times and introduce measurement inaccuracies. Alternatively, it would be possible to use a fiber switch that can be programmed to connect the various output to the detectors in an automatized fashion.
Instead of adding detection units or peripherals, we adopt a scheme that relies on the processor capability of implementing an arbitrary unitary operation to efficiently detect the system output with the available resources.
To this aim we may consider the following operation:

$$\hat{R}_{n,m} = |n\rangle\langle m| + |m\rangle\langle n| + \sum_{i\neq n,m} |i\rangle\langle i|, \tag{102}$$

where $|n\rangle$ represents a single photon on mode n. Notably, this operation has the following properties:

$$\begin{aligned} &\hat{R}_{n,m}\hat{R}^{\dagger}_{n,m} = \mathbb{I} \ \ \forall\, n, m \\ &\hat{R}_{n,m}|n\rangle = |m\rangle, \ \ \hat{R}_{n,m}|m\rangle = |n\rangle, \end{aligned} \tag{103}$$

which means that for any given combination of n and m, $\hat{R}$ is unitary and operates a permutation of the modes m and n. Given that $\hat{U}$ is the evolution we want to probe, if we program the network to implement the unitary operation:

$$\hat{U}_{n,m} = \hat{R}_{n,m}\hat{U} \tag{104}$$

the network output intensities will be the unchanged except for modes m and n.
In fact, $\hat{R}$ routes the intensity that would have been on mode n to mode m and vice-versa. If we keep the first index fixed, say to $n = 1$, while we change the second index we can probe the evolutions:

$$\hat{U}_i = \hat{U}_{0,i}. \tag{105}$$

For each of them, measuring light intensity at $n = 1$ is equivalent to the case where the network implements $\hat{U}$ and we measure on mode $i + 1$. Therefore, we can measure the output intensities for all modes keeping a single detector connected to output 1 and looping through the routed unitaries.
In order to extend this to the two photon case, we can consider the setup scheme shown in Fig. 18 and the operation:

$$\hat{U}_{n,m} = \hat{R}_{1,n}\hat{R}_{2,m}\hat{U} \tag{106}$$

which routes photons that were on mode n and m to outputs 1 and 2, respectively.

As shown in the setup sketch, output 1 is split using a 50:50 fiber splitter and sent to two detectors. If two photons come out of output 1, they will be separated with a probability of $\frac{1}{2}$, therefore the self coincidences for mode n can be obtained doubling the amount of coincidence events between detector 1 and 2. Instead, coincidences between mode n and m are obtained summing coincidences between detector 1 and 3 and 2 and 3.
The full coincidence matrix is then recovered probing all the $\hat{U}_{n,m}$ for $n, m = 1, \ldots, 12$, which can be done automatically using the processor driving software.
In conclusion, this allows us to implement a complex path encoded optical network and perform an efficient readout of the complete system output both in the single- and two-photon cases.

4.3 Time multiplexing setup

After dealing with the path encoded system, we now consider the time-multiplexed architecture used to perform part of the experiments described in this thesis. This setup is based on well established architectures [75, 93, 131, 94, 95, 124], and it consists of a time-multiplexed feedback loop featuring fiber delays and fast electro-optical modulators. In the present work, the system used in the referenced studies has been adapted and modified according to the requirements of each experiment. While the setup used to implement open dynamics is almost analogous to the one of previous works, to study the generation of entanglement, the system has been modified adding the tomography setup described in section 4.4. In experiments where we use this architecture to implement single- and two-qubit gates we modified the system using an electro-optical modulator capable of operating arbitrary polarization operations within in the feedback loop.

In this section we provide a description of the current state of the time-multiplexed loop. To this aim we start by illustrating the concept behind the time-multiplexed scheme. Later we recapitulate the operating principle of the electro-optical modulators, which constitute a fundamental part of the time-multiplexed architecture. Later we describe the setup in a level of detail which we deem appropriate to its reproduction and to show the main differences with respect to its previous iterations.

4.3.1 Time-multiplexed interferometric scheme

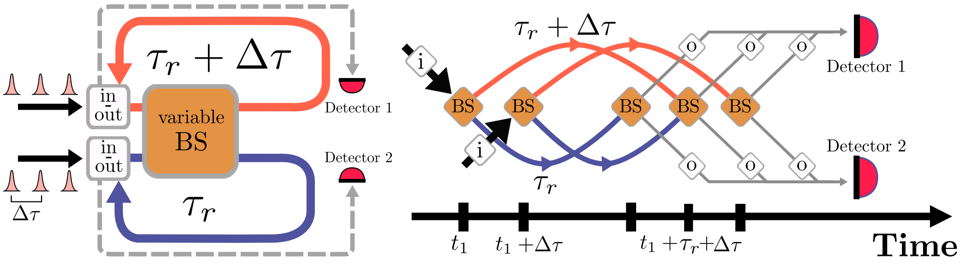

(a) (b)

Figure 19: **(a):** Time-multiplexed interferometric scheme. **(b):** Time-bin structure arising from the looped architecture.

This interferometric approach is based on the implementation of a unitary transformation between input and output time-multiplexed modes. These are encoded by a sequence of time-bins separated by a time $\Delta\tau$.

A transformation on consecutive time-bins can be implemented adopting the scheme shown in Fig. 19a, where we identify a structure featuring a short and a long delay loop with travel times τ_r and $\tau_r + \Delta\tau$. The two loops are connected by a variable beam splitter whose reflectivity may be set independently for any time-bin. Photons distributed on a stream of time-bins may enter or exit the looped architecture thanks to the action of two devices located within the loops (white in-out boxes in Fig. 19a).

A single roundtrip in this interferometer allows to interfere neighboring time-bins. This can be seen from Fig. 19b, where we consider two time-bins which are in-coupled and reach the variable beam splitter a times t_1 and $t_1 + \Delta\tau$. Photons travelling the short loop (blue) reach the next beam splitter after a time τ_r, while those travelling the long loop (red) after a time $\tau_r + \Delta\tau$. By equalling the time difference between loops and time-bins we ensure that photons, that were initially separated by $\Delta\tau$, can be recombined one roundtrip at $t = t_1 + \tau_r + \Delta\tau$, where they interfere when returning to the central beam splitter. Following this principle, time-bins spaced by $n\Delta\tau$ can be interfered performing n roundtrips in the interferometer. A readout of the output is possible using a detector for each loop capable of resolving the output time-bin stream.

In order to work, this approach relies on an internal degree of freedom that can be used on each time-bin in order to realize both variable beam splitter and in-(out-)coupling. In our setup this is constituted by the polarization of light travelling in the looped architecture.

4.3.2 Active polarization manipulation

In order to actively manipulate light polarization we employ electro-optical modulators based on Pockels effect, *i.e.* the change of refractive index along a certain crystal axis induced by an electric field [132]. This effect can be combined with natural birefringence in order to build a Pockels cell, which is a device that can alter light polarization depending on an externally applied voltage.
The electro-optical modulators used in this setup are based on Rubidium Titanyl Phospate (RTP) crystals arranged as shown in Fig. 20. The two crystals have the same length, but their optical axes are rotated by 90° with respect to each other. Natural birefringence in RTP causes light polarized along the slow axis to experience a higher refractive index than the one seen by light polarized parallel to the fast axis. Hence, there will be a relative phase shift $e^{i\phi}$ between the two polarizations. If a voltage V is applied along the crystal fast axis, Pockels effect induces a change in refractive index and a phase shift $e^{i\phi_V}$ is imparted to light polarized in this direction. Within the Pockels cell this is used such that the first and second crystal experience voltages $\pm V$, respectively. Therefore, in the crystal's reference frame we can model the action of the cell as follows:

$$\begin{aligned} \hat{U}_{cell} &= \begin{pmatrix} e^{i\phi} & 0 \\ 0 & e^{-i\phi_V} \end{pmatrix} \begin{pmatrix} e^{i\phi_V} & 0 \\ 0 & e^{i\phi} \end{pmatrix} = \\ &= e^{i(\phi+\phi_V)} \begin{pmatrix} 1 & 0 \\ 0 & e^{-2i\phi_V} \end{pmatrix}, \end{aligned} \tag{107}$$

which up to a common phase factor, can be interpreted as a waveplate that introduces a voltage-dependent phase shift between the two polarizations.
As it can be seen from Fig. 20, the crystals are rotated by 45° around the light propagation direction and therefore in the reference frame defined by the horizontally

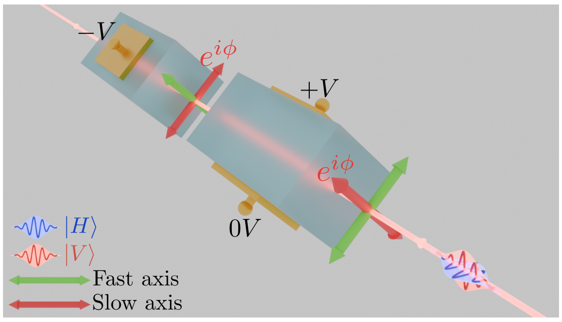

Figure 20: Schematics of a Pockels cell, when no voltage is applied to the cell light goes thorough two birefringent crystals of the same length but with slow and fast axis flipped, thus no change in polarization happens. When a voltage V is applied the crystals respectively impart a phase shift ϕ_V and $-\phi_V$ to the $|D\rangle$ and $|A\rangle$ polarized states. As a result $|H\rangle$ and $|V\rangle$ are put into a superposition that depends on the applied voltage.

and vertically polarized states $|H\rangle$ and $|V\rangle$ the transformation is represented by:

$$\begin{aligned}\hat{U}(V) &= \hat{R}(45°)\hat{U}_{cell}\hat{R}(-45°) = \\ &= \frac{e^{i(\phi+\phi_V)}}{2}\begin{pmatrix}1 & -1\\ 1 & 1\end{pmatrix}\begin{pmatrix}1 & 0\\ 0 & e^{-2i\phi_V}\end{pmatrix}\begin{pmatrix}1 & 1\\ -1 & 1\end{pmatrix} = \\ &= \frac{e^{i(\phi+\phi_V)}}{2}\begin{pmatrix}1+e^{-2i\phi_V} & 1-e^{-2i\phi_V}\\ 1-e^{-2i\phi_V} & 1+e^{-2i\phi_V}\end{pmatrix} = e^{i\phi}\begin{pmatrix}\cos\phi_V & i\sin\phi_V\\ i\sin\phi_V & \cos\phi_V\end{pmatrix},\end{aligned} \tag{108}$$

where $\hat{R}(\theta)$ is a 2-dimensional rotation matrix taking the form $\hat{R}(\theta) = \begin{pmatrix}\cos\theta & -\sin\theta\\ \sin\theta & \cos\theta\end{pmatrix}$. From Eq. (108), $|H\rangle$ and $|V\rangle$ are transformed, up to a common phase factor, as follows:

$$\begin{aligned}|H\rangle &\to \cos\phi_V|H\rangle + i\sin\phi_V|V\rangle\\ |V\rangle &\to \sin\phi_V|H\rangle - i\cos\phi_V|V\rangle.\end{aligned} \tag{109}$$

When no voltage is applied $\phi_V = 0$, thus the Pockels cell does not affect the incoming polarization. If V is such that ϕ_V is an odd multiple of $\frac{\pi}{2}$ we have $\hat{U}(V) \propto \begin{pmatrix}0 & 1\\ 1 & 0\end{pmatrix}$, hence the cell flips $|H\rangle$ and $|V\rangle$.
In all other cases from Eq. (109) we see that the device rotates $|H\rangle$ and $|V\rangle$ in a superposition of the two polarizations.
In our setup, this is used both to deterministically in- and out-couple photons and to implement a variable beam splitter operation.

4.3.3 Polarization based time-multiplexed setup

The time-multiplexed setup used in this work is depicted in Fig. 21. The setup input is located at a polarizing beam splitter (PBS 1), where H- and V- polarized photons coming from the SPDC source are coupled to two single mode fibers using fiber

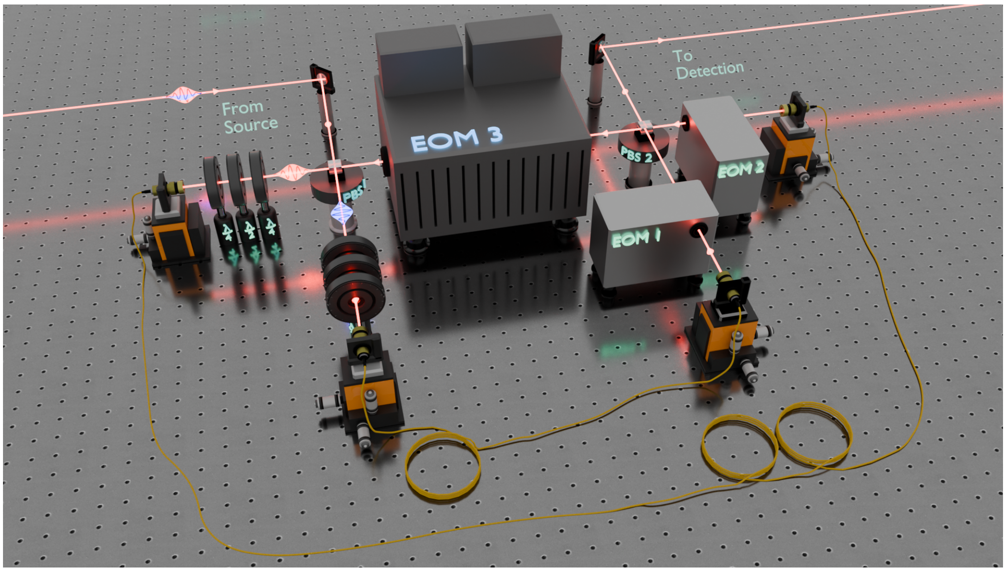

Figure 21: Time-multiplexed setup: photons at 1545 nm with H and V polarization enter the setup and are directed to the short and long single mode fiber, respectively. After travelling though the fibers they have accumulated a relative delay of 170 ns. EOM 1 and EOM 2 flip the photon polarizations in order to redirect both to the feedback where EOM 3 acts on their polarization states before travelling again to the fibers. At each roundtrip EOM 3 can implement an arbitrary series of operations which realize the optical interferometer. After the desired amount of roundtrips EOM 1 and 2 act again on the photon polarization to send the output time-bin stream to the detection unit described in section 4.4.

collimators.
The two fibers serve as delay loops and have lengths of 1085 and 1120 m, thus they introduce a relative delay between the two polarizations of $\Delta\tau = 170.05\ ns$. This parameter sets the temporal separation of the time-bins propagating within the setup and constitute the position separation of the walk.
Since single mode fibers can introduce a polarization rotation due to bending and imperfections, before each collimator we use a combination of two $\frac{\lambda}{4}$- and a $\frac{\lambda}{2}$-waveplates to pre-compensate changes in the polarization travelling in the delay loops. At the fiber outputs, two fiber collimators equal to the input ones, send H and V photons to two electro-optical modulators (EOMs 1 and 2). These are capable of rotating their polarization state only by 90°, and are used as in- and out-coupling units. Following from the action of these EOMs, a second polarizing beam splitter (PBS 2) directs photons to a third electro-optical modulator (EOM 3) located in the setup's feedback. EOM 3 constitutes the main addition to the setup with respect to the one showed in [124]. In fact, the EOM used here can implement an arbitrary polarization rotation, while the one used in the referenced work could only perform polarization flips. This ability of performing an arbitrary operation on the polarization of each time-bin allows us to realize the variable beam splitter shown in Fig. 19a. After EOM 3, all time-bins come back to PBS 1 where they are sent again to the delay fibers to perform the next roundtrip.

In this evolution we recognize the same structure of a discrete time quantum walk on a line, where the coin operation is carried out by EOM 3 and the shift operation corresponds to travelling in the delay fibers. Therefore, a step of the walk corresponds to one roundtrip in the interferometer. After performing the desired amount of roundtrips, photons are out-coupled using again EOMs 1 and 2 and are sent to the detection setup described in section 4.4.

4.3.4 Setup alignment

The efficiency of the setup is dictated by the alignment of inputs and outputs of the delay fibers. As shown in Fig. 21, all fiber collimators used to couple photons in the delay loops are mounted in a mirror mount positioned on a flexure stage. As demonstrated in [133], this arrangement provides all the degrees of freedom required to position a light beam, and we adopted it to eliminate the need of mirror pairs in front of each fiber input present in all previous implementations.

The setup efficiency consists of the average of four different fiber couplings, namely the two self-coupling efficiencies from a loop to itself and the two cross-coupling form a loop to the other. These can be measured during the setup alignment by setting the compensation units in front of the input collimators to flip polarization instead of preserving it. This causes light to travel always twice through the setup. In particular, as shown in Figs. 22a and 22b, when entering in a V-polarized state, light performs a roundtrip in the long delay line and, because of the action of the compensation waveplates, exits horizontally polarized. Therefore, PBS 2 transmits it to the feedback, where it goes through a $\frac{\lambda}{2}$-waveplate. If this is set to 0° (Fig. 22a), all light is sent to the long fiber for a second time and, as it exits in a V-polarized state, PBS 2 directs it outside the setup. Adjusting position and angle of the fiber collimator located at the output of the long loop we can optimize the amount of light that travels twice in the short fiber. Instead, setting the waveplate in the feedback at 45° (Fig. 22b), after performing a roundtrip in the long fiber, light is directed to the short one and then out. In this setting it is possible to optimize the amount of light traveling first in the long and then in the short loop adjusting the position of the collimator located at the input of the short fiber.

Similarly, as shown in Figs. 23a and 23b, entering in an H-polarized state, light travels first in the short fiber and can be directed to the short or long loop setting the waveplate at 0° or 45°, respectively. The self coupling from the short loop to itself can be optimized adjusting the collimator located before EOM 1. Instead, the remaining coupling from short to long loop can be optimized using the collimator connected to the input of the long fiber. In all configurations we identify I_{ref} and I_{out} as the light intensities measured in the feedback and outside the setup, respectively. From these two quantities we evaluate the coupling efficiency as $\frac{I_{out}}{I_{ref}}$, and by aligning the setup iteratively we equalize the four couplings and reach an average efficiency of 81%.

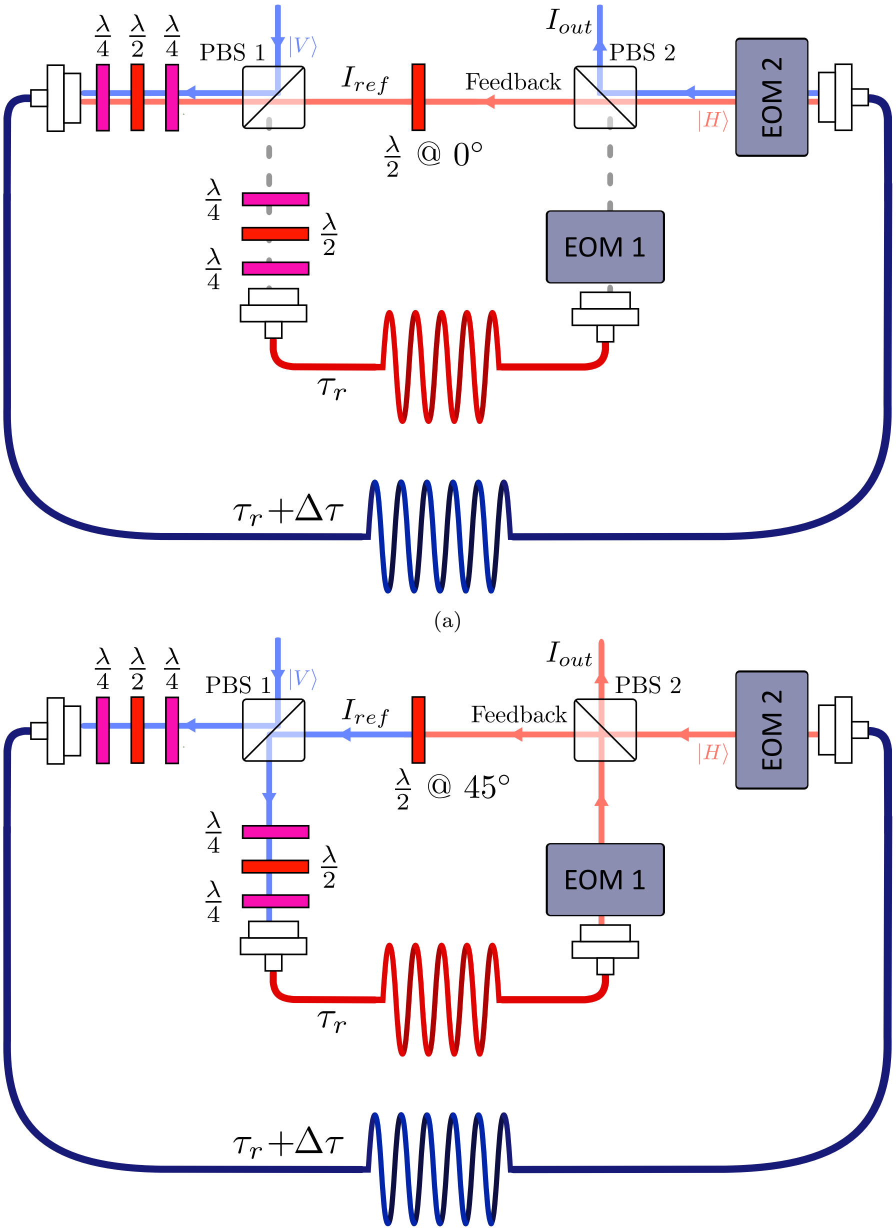

(a)

(b)

Figure 22: **(a):** Sketch of the beam path and input polarization for the optimization of the self coupling of the long loop. **(b):** Sketch of the beam path and input polarization for the optimization of the coupling from long to short loop.

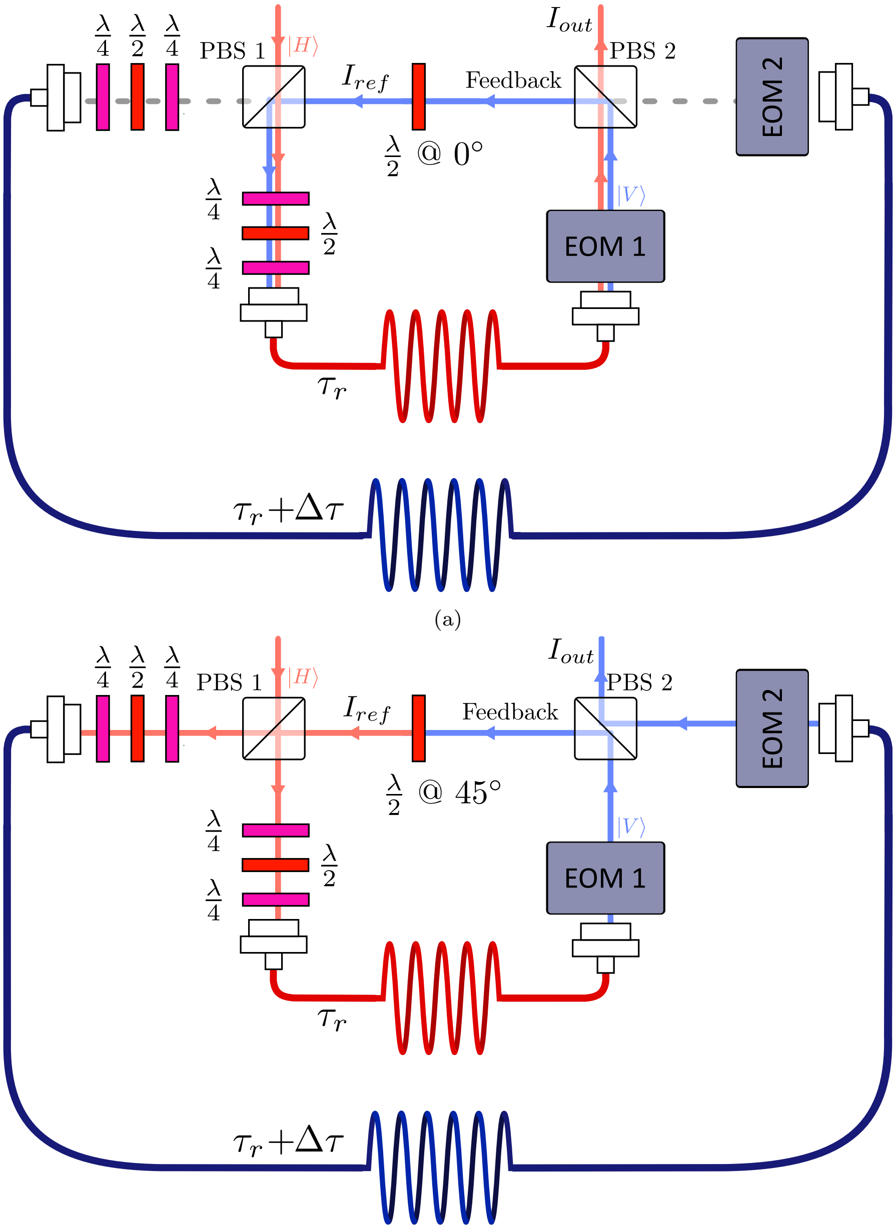

(a)

(b)

Figure 23: **(a):** Sketch of the beam path and input polarization for the optimization of the self coupling of the short loop. **(b):** Sketch of the beam path and input polarization for the optimization of the coupling from short to long loop.

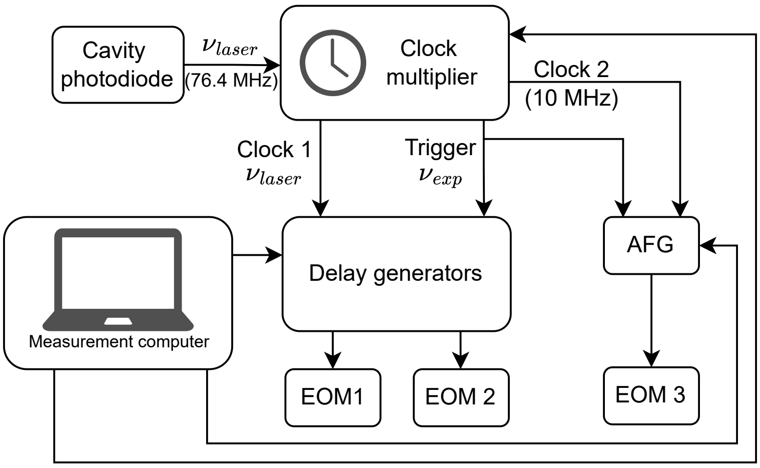

Figure 24: Scheme of the electronic signals used to drive the active time-multiplexed setup. A signal at ν_{laser} from the laser used to pump the photon source is fed to a clock multiplier which is set to output a clock and a trigger signal both for the delay generators that drive EOM 1 and 2 and for the arbitrary function generator driving EOM 3.

4.3.5 Electronic signals and synchronization

The presented scheme strongly relies on the exact synchronization of the involved active elements. We now discuss how this is achieved in terms of the required electrical control signals, which are schematically represented in Fig. 24. This time-multiplexed setup has been used in combination with the single photon source discussed in subsection 4.1.2, therefore all signals must be stably referenced to the laser pulses used to pump the ppKTP waveguide. This is done by taking the signal from a photodiode placed inside the laser cavity, which outputs a signal with a frequency $\nu_{laser} = 76.4\ MHz$. The photodiode signal is fed to a clock multiplier, this device allows to generate signals with a frequency proportional to the input one which are temporally stable with respect to the produced laser pulses. With this device we produce three different signals: two clocks (Clock 1 and Clock 2) and a trigger. The trigger signal with frequency ν_{exp} corresponds to the repetition rate at which the photon source is pumped. As highlighted in subsection 4.1.2, this is achieved performing pulse picking with an electro-optical modulator analogous to EOM 1 and 2. EOM 1 and 2 are driven by delay generator cards (additional details can be found in [124]) while EOM 3 is driven by the signal provided by an arbitrary function generator (AFG). Both delay generators and AFG receive the same trigger signal from the clock multiplier and upon a trigger event they repeat the switching sequence programmed by the computer used to run the experiment. Similarly, this signal is also sent to the delay generator used to control the pulse picking electro-optical modulator in the source and to the time tagging module used in combination with SNSPDs to perform detection.

All the delay generators receive a clock signal (Clock 1) with frequency equal to ν_{laser}. The second clock (Clock 2), with a frequency of 10 MHz, is sent to the AFG and together with the trigger is required to run EOM 3.

Different number of roundtrips in the setup correspond to a different length of the temporal window between one experiment and the following one, therefore ν_{exp} must be adjusted accordingly using the measurement computer to reprogram the clock multiplier.

As we have already stated we send a separated trigger to the delay generator for pulse picking, the same is true for its clock, this is done because the EOM in the source is driven by a delay generator physically separated from the ones used for EOMs 1 and 2. This configuration is adopted in order to limit crosstalk among pulse picking and active in-/out-coupling.

Once it is ensured that all clocks and triggers are temporally stable and provided that a laser pulse is correctly picked, the action of all EOMs must be properly timed to act on the incoming photons. This is achieved by applying appropriate delays to the signals generated by delay generators and AFG, therefore we use the measurement computer to adjust the delay of each switching pattern in order to match it with the arrival times of H and V photons to EOM 1, 2 and 3.

4.4 Polarization tomography setup

We have seen how in the active time-multiplexed setup the internal degree of freedom is encoded in the photon's polarization state. A part of this work is devoted to the investigation of quantum walks featuring two walkers, implemented by two single photons entering the setup in a given polarization state. Implementations of the time-multiplexed architecture, as the one shown in [124], feature detection units where both coin and position degrees of freedom can be resolved, which is sufficient to reconstruct the walk's output probabilities. In this work, we extend the detection capabilities of the setup in order to be able of reconstructing the quantum state of a pair of walkers in their joint coin degree of freedom.
To this aim, starting from the concepts presented in subsection 3.3.4, we now discuss the working principle and the detection setup built and used to perform the experiments described in sections 5.3 and 5.4.

4.4.1 Polarization state tomography

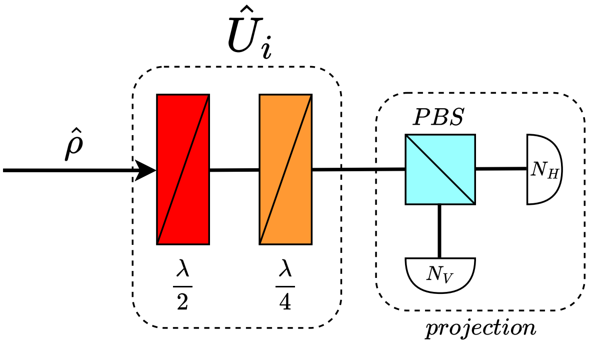

Figure 25: Sketch of a polarization tomography setup for a single qubit

Given the bidimensional nature of the polarization space, it is possible to treat the polarization state of a single photon as a qubit. Performing tomography on a qubit in a state represented by a generic density operator $\hat{\rho}$ requires to implement a series of projective measurements, where N copies of $\hat{\rho}$ undergo a transformation $\hat{U}_i$ before being projected onto the computational basis.
The aim of the measurements is to obtain the expectation value of the Pauli operators, which according to Eq. (46), give the coordinates of the Bloch vector associated to the state.
For this reason, we must devise a set of operations $\{\hat{U}_x, \hat{U}_y, \hat{U}_z\}$ which must transform the eigenbasis of the Pauli operators into the states of the computational basis. We choose the computational basis to be the one formed by the horizontally and vertically polarized states ($\{|H\rangle, |V\rangle\}$), accordingly the $|\pm\rangle$ basis is given by the diagonally and

	$\frac{\lambda}{2}$	$\frac{\lambda}{4}$
$\hat{\sigma}_{\mathbf{x}}$	22.5°	0°
$\hat{\sigma}_{\mathbf{y}}$	45°	−45°
$\hat{\sigma}_{\mathbf{z}}$	0°	0°

Table 1: Tomographic settings for the reconstruction of the polarization state of a photon.

anti-diagonally polarized states ($\{|D\rangle, |A\rangle\}$), while $|\pm i\rangle$ contains the right- and left-circular polarization states ($\{|R\rangle, |L\rangle\}$).
These three sets constitute the Pauli bases in the polarization space, therefore the transformations $\hat{U}_i$ are implemented by components acting in the polarization space, whereby tomography can be performed according to the scheme shown in Fig. 25.
The unknown polarization encoded state $\hat{\rho}$ is initially sent through a $\frac{\lambda}{2}$- followed by a $\frac{\lambda}{4}$- waveplate. The tomographic unitaries $\hat{U}_i$ result from the combined action of these two components on $\hat{\rho}$, in particular using the angle settings listed in table 1 we implement the operations:

$$\hat{U}_x = \frac{1}{\sqrt{2}}\begin{pmatrix}1 & 1\\ i & -i\end{pmatrix}, \; \hat{U}_y = \frac{e^{i\frac{3}{4}\pi}}{\sqrt{2}}\begin{pmatrix}1 & -i\\ -i & 1\end{pmatrix}, \; \hat{U}_z = \begin{pmatrix}1 & 0\\ 0 & -i\end{pmatrix}. \tag{110}$$

These operations transform the vectors of the respective Pauli bases into the vectors of the computational basis up to a multiplicative phase factor. Such a phase is irrelevant because the action of $\hat{U}_i$ is followed by a projection onto the computational basis. This is achieved by using a polarizing beam splitter, which separates $|H\rangle$ and $|V\rangle$ and directs them to two detectors. The Bloch vector associated to $\hat{\rho}$ is reconstructed collecting the number of H and V counts for each basis and substituting them into Eqs. (57-59).

This approach can be extended to the case of two photons combining two units like the one shown in Fig. 25, thus obtaining the structure shown in Fig. 26. We are now interested in evaluating the expectation values $\langle\hat{\sigma}_i \otimes \hat{\sigma}'_j\rangle$, which, considering the respective eigenstates $|i_\pm\rangle$ and $|j'_\pm\rangle$, may be written as:

$$\begin{aligned}\langle\hat{\sigma}_i \otimes \hat{\sigma}'_j\rangle &= \langle(|i_+\rangle\langle i_+| - |i_-\rangle\langle i_-|) \otimes (|j'_+\rangle\langle j'_+| - |j'_-\rangle\langle j'_-|)\rangle = \\ &= \langle|i_+j'_+\rangle\langle i_+j'_+| - |i_+j'_-\rangle\langle i_+j'_-| - |i_-j'_+\rangle\langle i_-j'_+| + |i_-j'_-\rangle\langle i_-j'_-|\rangle = \\ &= P_{i_+j'_+} - P_{i_+j'_-} - P_{i_-j'_+} + P_{i_-j'_-},\end{aligned} \tag{111}$$

where $P_{i_+j'_+}$, $P_{i_+j'_-}$, $P_{i_-j'_+}$ and $P_{i_-j'_-}$ are the probabilities for the two photons to be in each of the eigenstates of $\hat{\sigma}_i \otimes \hat{\sigma}'_j$.
To obtain these probabilities experimentally we must first separate the two photons. This is accomplished probabilistically by the balanced beam splitter shown in Fig. 26. After the beam splitter two sets of waveplates implement the tomographic operations $\hat{U}_i$ and $\hat{U}'_j$, which perform the rotation from local Pauli basis to the computational one. After this, two polarizing beam splitters separate the $|H\rangle$ and $|V\rangle$ contributions for

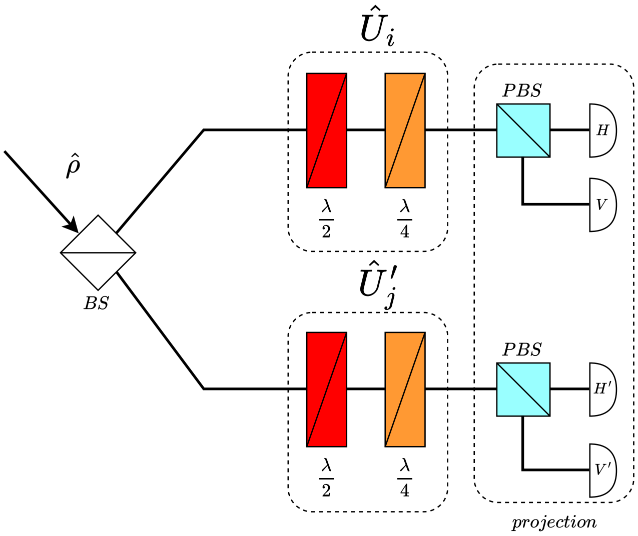

Figure 26: Sketch of the tomographic setup required to reconstruct the joint polarization state of two photons.

each photon and direct them to the four detectors here indicated with H, V, H' and V', corresponding to the outcomes $|i_+\rangle$, $|i_-\rangle$, $|j'_+\rangle$ and $|j'_-\rangle$.
In order to determine the probabilities appearing in Eq. (111), now we must record coincidences between pairs of detectors, namely the pairs HH', HV', VH', VV', resulting in the numbers of counts: $N^{(ij)}_{HH'}$, $N^{(ij)}_{HV'}$, $N^{(ij)}_{VH'}$ and $N^{(ij)}_{VV'}$.
The expectation value $\langle\hat{\sigma}_i \otimes \hat{\sigma}'_j\rangle$ is obtained combining these coincidences as follows:

$$\langle\hat{\sigma}_i \otimes \hat{\sigma}'_j\rangle = \frac{N^{(ij)}_{HH'} - N^{(ij)}_{HV'} - N^{(ij)}_{VH'} + N^{(ij)}_{VV'}}{N^{(ij)}_{HH'} + N^{(ij)}_{HV'} + N^{(ij)}_{VH'} + N^{(ij)}_{VV'}}. \tag{112}$$

Sticking to the form of an N-qubit density operator (see Eq. (60)), $\hat{\rho}$ also contains terms proportional to $\mathbb{I} \otimes \hat{\sigma}'_j$ and $\hat{\sigma}_i \otimes \mathbb{I}'$, whose expectation values are obtained considering that $\mathbb{I}$ is diagonal in any of the Pauli bases, therefore:

$$\begin{aligned}\langle\mathbb{I} \otimes \hat{\sigma}'_j\rangle &= \langle(|i_+\rangle\langle i_+| + |i_-\rangle\langle i_-|) \otimes (|j'_+\rangle\langle j'_+| - |j'_-\rangle\langle j'_-|)\rangle = \\ &= \langle|i_+j'_+\rangle\langle i_+j'_+| - |i_+j'_-\rangle\langle i_+j'_-| + |i_-j'_+\rangle\langle i_-j'_+| - |i_-j'_-\rangle\langle i_-j'_-|\rangle = \\ &= P_{i_+j'_+} - P_{i_+j'_-} + P_{i_-j'_+} - P_{i_-j'_-}\end{aligned} \tag{113}$$

and

$$\begin{aligned}\langle\hat{\sigma}_i\otimes\mathbb{I}\rangle &= \langle(|i_+\rangle\langle i_+| - |i_-\rangle\langle i_-|)\otimes(|j'_+\rangle\langle j'_+| + |j'_-\rangle\langle j'_-|)\rangle = \\ &= \langle|i_+j'_+\rangle\langle i_+j'_+| + |i_+j'_-\rangle\langle i_+j'_-| - |i_-j'_+\rangle\langle i_-j'_+| - |i_-j'_-\rangle\langle i_-j'_-|\rangle = \\ &= P_{i_+j'_+} + P_{i_+j'_-} - P_{i_-j'_+} - P_{i_-j'_-},\end{aligned} \tag{114}$$

which in terms of the measured coincidences corresponds to:

$$\langle\mathbb{I}\otimes\hat{\sigma}'_j\rangle = \frac{N^{(ij)}_{HH'} - N^{(ij)}_{HV'} + N^{(ij)}_{VH'} + N^{(ij)}_{VV'}}{N^{(ij)}_{HH'} + N^{(ij)}_{HV'} + N^{(ij)}_{VH'} + N^{(ij)}_{VV'}}, \tag{115}$$

$$\langle\hat{\sigma}_i\otimes\mathbb{I}'\rangle = \frac{N^{(ij)}_{HH'} + N^{(ij)}_{HV'} - N^{(ij)}_{VH'} - N^{(ij)}_{VV'}}{N^{(ij)}_{HH'} + N^{(ij)}_{HV'} + N^{(ij)}_{VH'} + N^{(ij)}_{VV'}}. \tag{116}$$

4.4.2 Tomography setup

At this point we have a complete conceptual scheme of how the tomography setup is supposed to operate and what quantities must be recorded. Fig. 27 shows a sketch of the setup that we have built to implement this scheme. Photon pairs whose state is distributed on a series of time-bins come from the time-multiplexed setup and are directed to a 50 : 50 beam splitter where they are separated probabilistically and sent

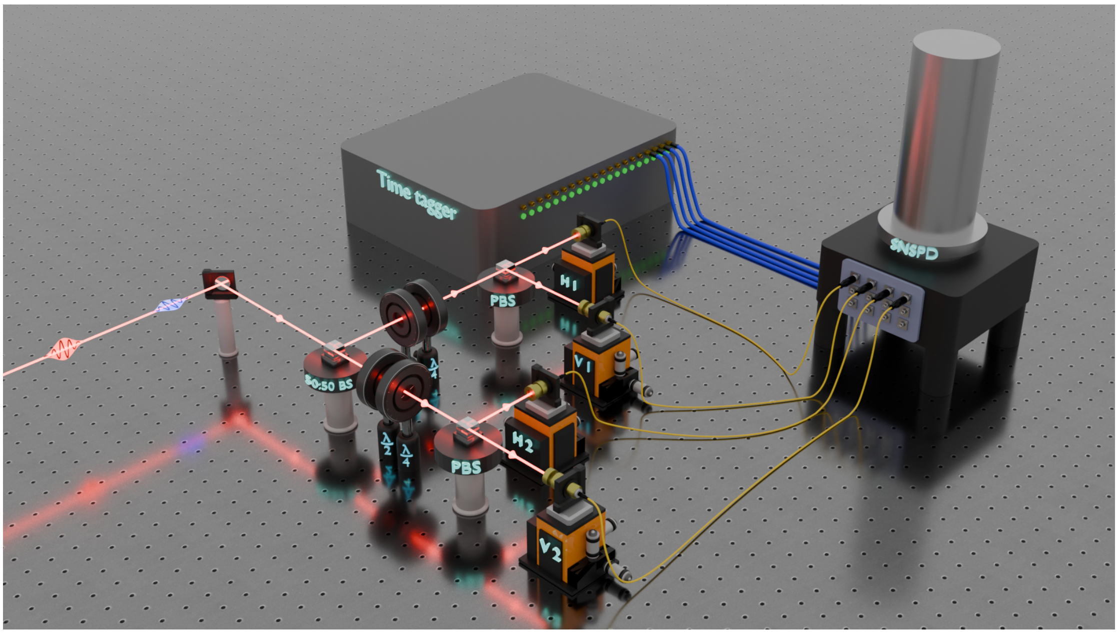

Figure 27: Sketch of the tomography setup. Two photons distributed over two time-bins are separated probabilistically by a 50:50 beam splitter (50:50 BS) and sent to two tomographic stages where waveplates ($\frac{\lambda}{2}$ and $\frac{\lambda}{4}$) and polarizing beam splitters (PBS) implement the projection in one of the Pauli bases. The state is reconstructed recording time stamps relative to the two time-bins from the four detectors and correlating them to reconstruct the joint outcome probabilities.

to the two tomographic units. Here the two waveplates are installed in four motorized rotation stages that allow to set them to the angles listed in Tab. 1 in order to implement the correct unitary transformation. The adoption of motorized stages allows to automate the basis selection process and improves its reproducibility. After the waveplates two polarizing beam splitters separate H- and V-polarized photons and send them to the four detection units H1, V1, H2, V2, where they are coupled to single mode fibers with an efficiency of ≈ 85%. The fibers are connected to four SNSPDs with efficiency ≥ 90%, whose output is connected to a time tagging module. Using the time tagger we record time-stamps relative to the time-bins expected from the time-multiplexed setup output. This is achieved starting from the experimental trigger signal, which is feed to a physical channel of the time tagger and is used to generate a series of delayed virtual channels whose delay corresponds to the time between a trigger event and the time-bin under observation. By recording time-stamps corresponding to coincidences between the delayed triggers and the physical channels we obtain only events relative to the time-bins generated in the time-multiplexed setup.
The coincidences necessary to reconstruct the expectation values of Pauli operators are calculated correlating time-stamps from the $H1$, $V1$, $H2$ and $V2$ channels according to Eqs. (112), (115) and (116).

The density operators can be reconstructed only with a tomographycally complete set of measurements, *i.e.* a set of measurements that allows to reconstruct $\langle \hat{\sigma}_i \otimes \hat{\sigma}'_j \rangle$ for $i, j \in \{x, y, z\}$. To see what settings are required in our cases let us consider a case where we are interested in the polarization state of two photons occupying time-bins t_1 and t_2. If $t_1 \neq t_2$, upon reaching the input beam splitter the four scenarios shown in Fig. 28 can occur with equal probability. Therefore, post-selecting on events compatible with a) and b) can be used to obtain $\langle \hat{\sigma}_i \otimes \hat{\sigma}'_j \rangle$ and $\langle \hat{\sigma}_j \otimes \hat{\sigma}'_i \rangle$. If instead we post-select on events compatible with c) and d), since we are considering a case where photons are temporally separated, we can obtain $\langle \hat{\sigma}_i \otimes \hat{\sigma}'_i \rangle$ and $\langle \hat{\sigma}_j \otimes \hat{\sigma}'_j \rangle$. Therefore, employing the

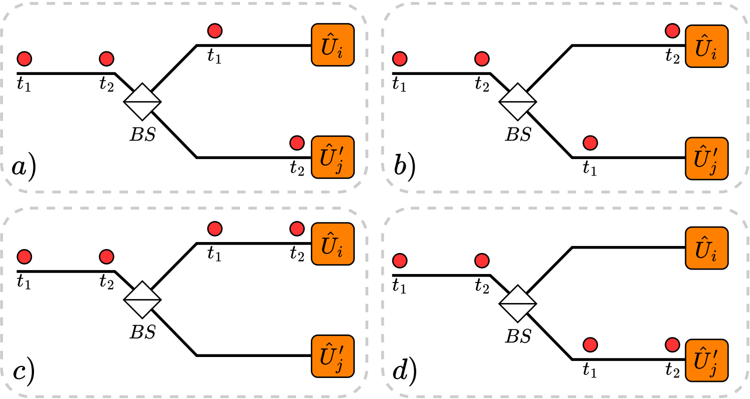

Figure 28: Possible outcomes in the tomography setup for two photons localized in time-bins t_1 and t_2.

settings: $\hat{U}_z\hat{U}'_x$, $\hat{U}_z\hat{U}'_y$ and $\hat{U}_x\hat{U}'_y$ the following expectation values are accessible:

	$\hat{U}_z\hat{U}'_x$	$\hat{U}_z\hat{U}'_y$	$\hat{U}_x\hat{U}'_y$
a)	$\langle\hat{\sigma}_z \otimes \hat{\sigma}'_x\rangle$	$\langle\hat{\sigma}_z \otimes \hat{\sigma}'_y\rangle$	$\langle\hat{\sigma}_x \otimes \hat{\sigma}'_y\rangle$
b)	$\langle\hat{\sigma}_x \otimes \hat{\sigma}'_z\rangle$	$\langle\hat{\sigma}_y \otimes \hat{\sigma}'_z\rangle$	$\langle\hat{\sigma}_y \otimes \hat{\sigma}'_x\rangle$
c)	$\langle\hat{\sigma}_z \otimes \hat{\sigma}'_z\rangle$	$\langle\hat{\sigma}_z \otimes \hat{\sigma}'_z\rangle$	$\langle\hat{\sigma}_x \otimes \hat{\sigma}'_x\rangle$
d)	$\langle\hat{\sigma}_x \otimes \hat{\sigma}'_x\rangle$	$\langle\hat{\sigma}_y \otimes \hat{\sigma}'_y\rangle$	$\langle\hat{\sigma}_y \otimes \hat{\sigma}'_y\rangle$

Table 2: Combinations of tomographic unitaries and respective accessible expectation values.

Where we see that the three settings are more than enough to reconstruct the nine possible combinations of Pauli operators. However, if we now consider the case $t_1 = t_2$, since the SNSPDs used cannot resolve the number of photons that have impinged on a single detector, cases *c*) and *d*) become unusable. In order to be able of reconstructing states where two photons populate the same time-bin we must also measure the settings $\hat{U}_z\hat{U}'_z$, $\hat{U}_x\hat{U}'_x$ and $\hat{U}_y\hat{U}'_y$ and only look at events where the two photons have been separated by the input beam splitter. Thus, in the case $t_1 = t_2$, $\hat{\rho}$ can be reconstructed adopting a total of six settings for the waveplates.

5 Results

After showing the experimental platforms employed to generate, evolve and detect states of one and two photons, now we describe how they have been combined in order to show the results of this work. In subsection 5.1.1 we show how using unitary routing in the path encoded platform we gain a better control on classical and quantum interference happening within the integrated device. After this, in subsection 5.1.2, we provide experimental results about path encoded Hadamard walks of one and two photons. Then, in subsection 5.1.3, we show how the unitary routing can be extended to perform on-chip tomography of a two qubit state.
In section 5.2 we present results on the study of lossy dynamics both in the path encoded platform an in the time-multiplexed one, in doing this we show how we can simulate coupling to an external environment both in a spatial and temporal fashion. With this we have the opportunity of comparing the capabilities of the two platforms and given the higher scalability of the time-multiplexed one we proceed to show results obtained only using the active time-multiplexed setup. In this framework, in section 5.3, we see how the setup has been used to generate polarization entanglement using and Hadamard walk and measurement induced nonlinearities. Finally, in section 5.4 we take step towards time-multiplexed gate based quantum computation showing how we applied the temporal encoding to the realization of a post-selected photonic CNOT gate.

5.1 Path encoded unitary implementations

Now we present results pertaining the use of unitary routing for the implementation of Hadamard walks of one and two photons in the photonic processor presented in section 4.2.

We start by showing the platform behavior in terms of classical and quantum interference when no routing is adopted. We compare these results with the routed case and show that adopting this approach we can optimize single- and two-photon interference.

Furthermore, we show Hadamard walks of one photon up to six steps featuring similarities with respect to the theoretical expectations up to 99.5% and a six steps two photon walk showing 90.0% similarity with respect to theory.

At the end of this section we extend the concept of unitary routing and show that, following a similar approach, we can generate two-qubit path encoded states and perform state tomography directly on chip.

5.1.1 Classical and quantum interference

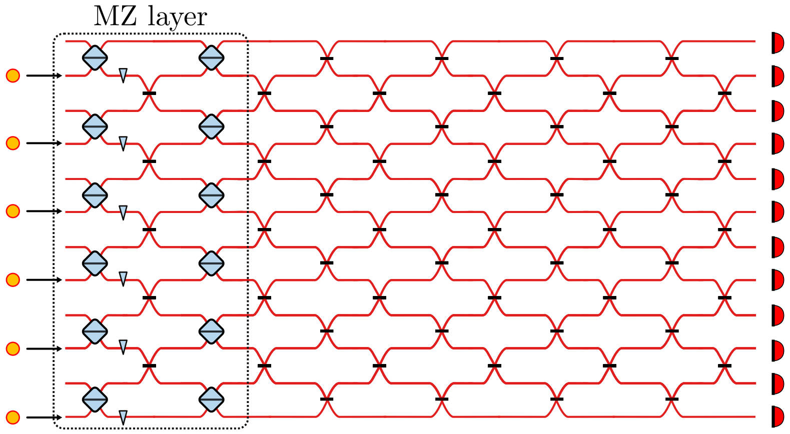

Figure 29: Schematics of the interferometer implementing a series of Mach-Zehnder interferometers involving pairs of inputs.

As a first analysis we investigate classical wave interference in the photonic network. To this aim we program the chip's phase shifters to implement the interferometer shown in Fig. 29, where the beam splitters in the first and third layer are set implement a 50:50 splitting. In the first layer we also set a value for the phase between the beam splitter outputs. All other phases are set to zero and the crossings marked with a horizontal black line indicate a reflection. With these settings we implement six Mach-Zehnder interferometers among mode pairs (1,2), (3,4), (5,6), (7,8), (9,10) and (11,12). Connecting a single mode fiber to inputs 2, 4, 6, 8, 10 and 12, we send a CW laser with a wavelength of 1550 nm to each Mach-Zehnder. For each input we scan the phase applied after the first 50:50 beam splitter and measure the intensities transmitted to the two outputs, repeating this procedure for each interferometer we record the interference traces shown in Fig. 30.

Each plot shows the normalized intensities recorded in all outputs as a function of the applied phases in the range $[0, \pi]$. The experimentally measured trends are shown in comparison with the theoretically expected interference patterns. As already shown in Eq. (97), when a phase ϕ is applied to one of the interferometer arms light is redistributed on the outputs according to the transformation:

$$\hat{U} = \begin{pmatrix} \cos\frac{\phi}{2} & -i\sin\frac{\phi}{2} \\ -i\sin\frac{\phi}{2} & \cos\frac{\phi}{2} \end{pmatrix}, \tag{117}$$

and as we enter all Mach-Zehnders from only one input the expected intensities for each output pair follow the phase dependency:

$$I^{out}_{n,n+1} \propto \begin{pmatrix} \cos^2\left(\frac{\phi}{2}\right) \\ \sin^2\left(\frac{\phi}{2}\right) \end{pmatrix}, \tag{118}$$

All plots shown in Fig (30), qualitatively show this behavior, however with deviations from the expected trends (red and blue dashed lines in the figure).

To quantify the deviation from the ideal behavior for all interference scan we calculate the similarity between experiment and theory, which are calculated as:

$$S = \frac{\sum_i I^{theo}(\phi_i) I^{exp}(\phi_i)}{\sqrt{\sum_i I^{theo}(\phi_i)^2 \sum_j I^{exp}(\phi_j)^2}} \tag{119}$$

Fig. 31 shows the obtained similarities for all pairs of input-output combinations. Comparing the values, modes located at the center of the network tend to show lower similarities than the ones located at the edges of the network. In our case this effect is particularly detrimental as, in order to perform a walk with the maximum amount of steps we need to feed photons to inputs $(6, 7)$, which are located in the region showing the lowest similarities.

This picture is confirmed also when looking at quantum interference. To show this we program the network as shown in Fig. 32. In this case, we send photon pairs from the source to each mode pair where we set a 50:50 beam splitter to perform HOM interference. This is achieved using the setup shown in Fig. 33, where a PBS separates signal and idler pairs form the source and sends them to two polarization maintaining single mode fibers connected to the selected input pair of the network. A $\frac{\lambda}{2}$ at 45° ensures that both photons are indistinguishable in polarization.

For each input pair we use the delay line positioned in the path of one of the photons to scan the temporal indistinguishability of the two particles. Using two SNSPDs, we record coincidences among each beam splitter output pair as a function of the temporal delay, and we use the visibilities of the obtained HOM dips to quantify the quality of quantum interference.

The obtained visibilities are shown in Fig. 34, where we must notice that all values are

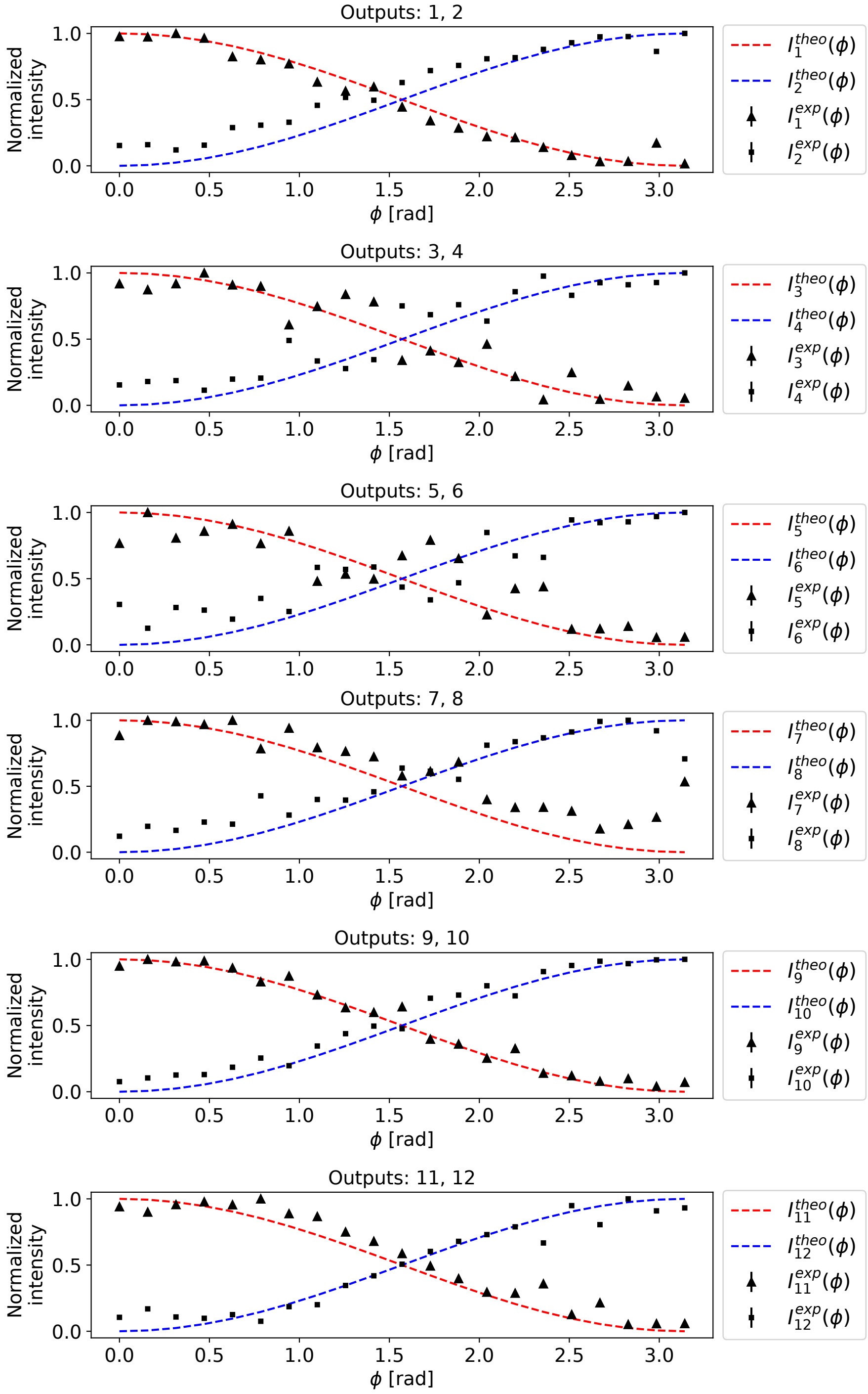

Figure 30: Interference traces for each output of the Mach-Zehnder board. Light is sent to the even-numberd inputs. As the phase is changed we see how interference affects intensities in the two outputs.

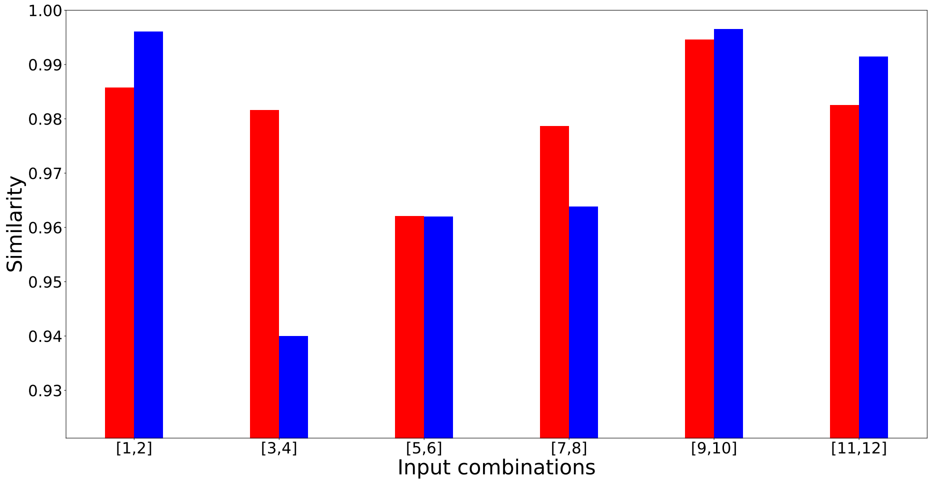

Figure 31: Similarities between the interference trends of Fig. 30. Red and blue bars respectively indicate odd and even outputs.

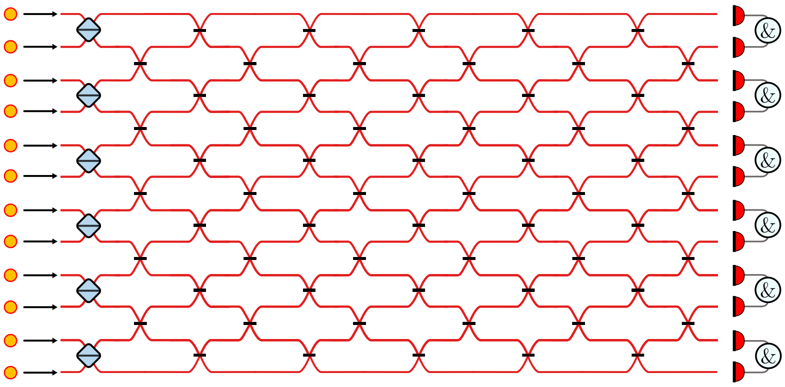

Figure 32: Schematics of the interferometer implementing a series 50:50 beam splitters. For each input pair we use single mode fibers to send signal and idler pairs from the source to each beam splitter. Each mode pair is connected to two SNSPDs used to record coincidences between outputs of each beam splitter.

sensitively lower than the ones reported in subsection 4.1.4 for time and polarization HOM. This is due to the fact that the 1.8 *nm* bandpass filter was not available at the time of this analysis, therefore, photons feature a lower indistinguishability because of spurious spectral features.

However, all the HOM scans have been conducted in the same experimental condition from a spectral point of view. Given this consideration, the network's behavior is the only factor influencing the interference visibility, which, in this case too, appears to be worse in the central region of the network.

This behavior is particularly disadvantageous and would severely limit the quality of

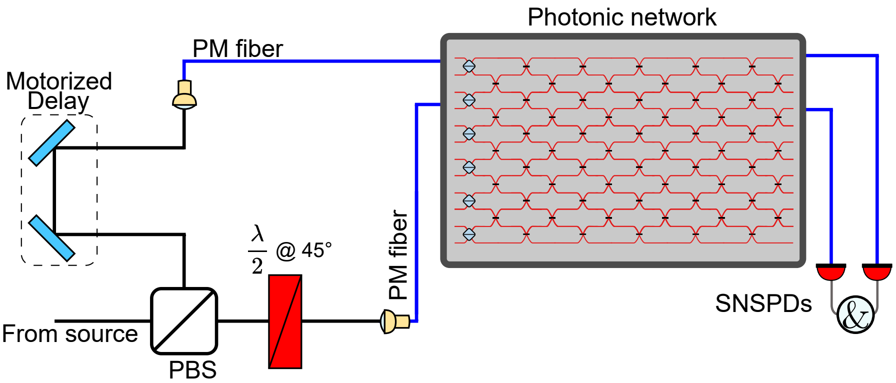

Figure 33: Setup used to perform HOM interference in the photonic network. Photons from the source are separated using a PBS and are sent to the chip using polarization maintaining single mode fibers. A $\frac{\lambda}{2}$ at 45° ensures that both photons are indistinguishable in polarization. A delay line in one of the two arms allows to scan the temporal delay of the two photons. Two SNSPDs connected to the network allow to record coincidences among selected output pairs.

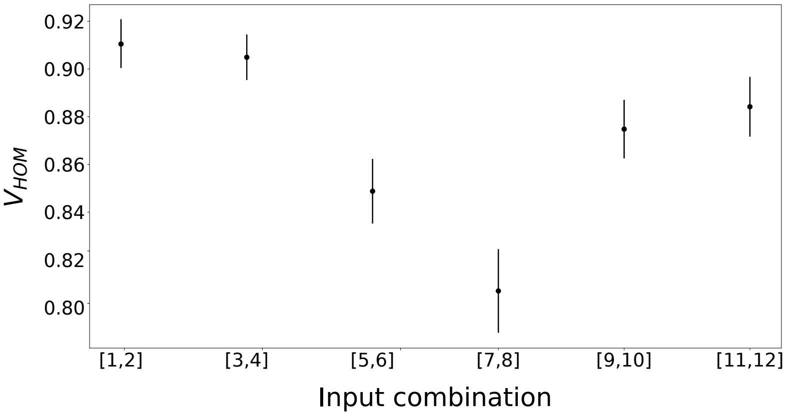

Figure 34: HOM dip visibilities obtained interfering two photons at each input of the photonic network.

the walk both in its single- and two-photon implementations.

In order to overcome these issues and efficiently use the available detectors we resort to the unitary routing discussed in subsection 4.2.3 both in input and output. Since we require photons to start at the center of the network we consider the following global evolution:

$$\hat{R}_{out}(i \rightarrow out_1, j \rightarrow out_2)\hat{U}\hat{R}_{in}(in_1 \rightarrow 6, in_2 \rightarrow 7),$$

where $in_{1,2}$ and $out_{1,2}$ are the inputs and outputs that are physically connected to the network.
In order to determine the best input-output combination we perform again HOM interference, thus $\hat{U}$ is set to be a 50:50 beam splitter between modes 6 and 7. Fig. 35 shows a conceptual scheme of what the routing does in this case. Once the two physical

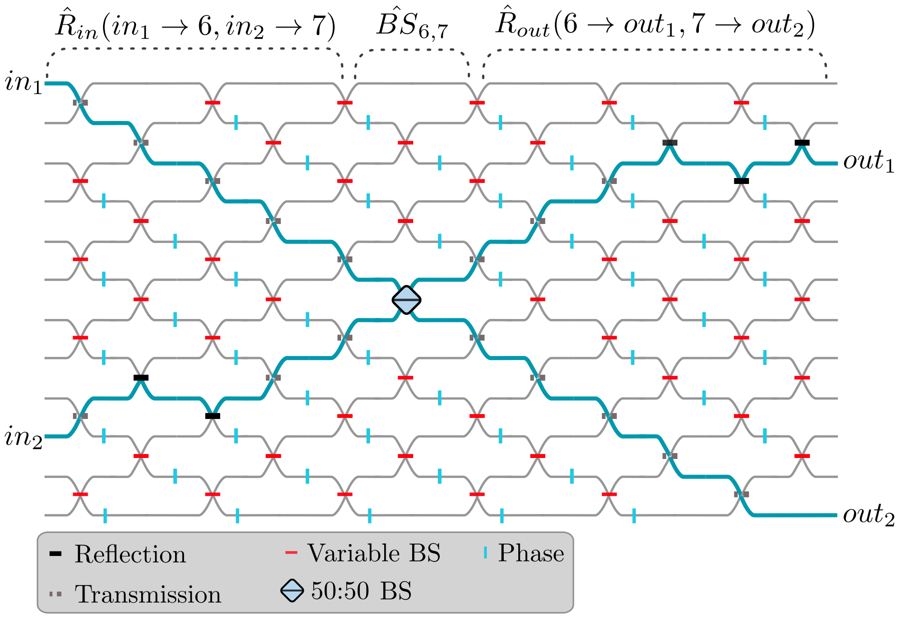

Figure 35: Example of a routed evolution: photons entering on inputs in_1 and in_2 are directed to the central 50:50 beam splitter by an input routing unitary. After the action of the 50:50 beam splitter , an output routing unitary sends photons to the desired physical output of the network where detection is performed.

inputs in_1 and in_2 are selected the unitary $\hat{R}_{in}(in_1 \to 6, in_2 \to 7)$ directs photons that enter on those inputs to one of the beam splitters acting on the two central modes of the chip. This beam splitter is set to 50:50 and here photon pairs can perform HOM interference. After the 50:50 beam splitter, the unitary $\hat{R}_{out}(6 \to out_1, 7 \to out_2)$ sends the photons to the output modes out_1 and out_2 where they are detected.

Since our previous analysis highlighted that the outer inputs perform better than the central ones we only consider physical connections involving mode combinations: $(1, 2)$, $(1, 12)$ and $(11, 12)$ both for feeding photons in the network and collecting them. Interference visibilities have been evaluated for all possible input-output combinations and are shown in Fig. 36 where we see that the combination $\hat{R}_{out}(6 \to 1, 7 \to 2)\hat{BS}(6, 7)\hat{R}_{in}(1 \to 6, 2 \to 7)$ has the highest visibility, whereby we find a value $V^{Max}_{Routed} = (90.9 \pm 0.9)\%$.

From this comparison we see that the maximum visibility obtained using the routing is comparable with the unrouted one and therefore using unitary routing we can overcome the limitations seen in the case of physical reconnection. To further show the method performance we are now present the results obtained applying this strategy to the implementation of Hadamard walks.

5.1.2 Single and two photon quantum walks with routing

Before showing the measured walks we must clarify how position and coin are encoded in the photonic network. The chip can encode at maximum for 12 modes, which we

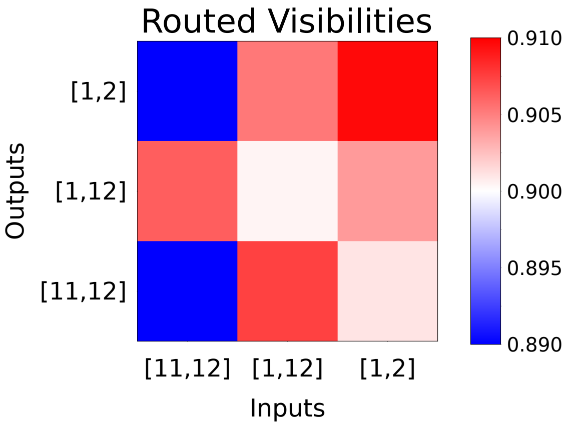

Figure 36: Routed HOM visibilities, the axes represent which input and outputs are used, while the 50:50 beam splitter is always set between mode 6 and 7.

want to use to represent the walk basis states $|x, \uparrow\rangle$, $|x, \downarrow\rangle$, where x denotes the walker's position and $|\uparrow\rangle, |\downarrow\rangle$ are the two available coin states.
Keeping in mind Fig. 17b we may identify the crossing in each vertical layer of the network as the positions on the line, whereby the first layer can be neglected as it only redirects light towards the central beam splitter in the second layer. Since the walk starts there, we identify the two incoming modes as $|0\downarrow\rangle$ and $|0\uparrow\rangle$. This beam splitter implements the first step of the walk and its output modes correspond to the walk states $|1\uparrow\rangle$ and $|-1\downarrow\rangle$.
From this we see that paths travelling upwards and downwards correspond to the coin states $|\uparrow\rangle$ and $|\downarrow\rangle$, respectively, while moving upwards or downwards correspond to increasing or decreasing the walker's position by a unit.
Following this criterion, it is possible to see that the 12 modes encode for different walk basis states at even and odd steps as shown in Table 3.

Mode / **Step**	**1**	**2**	**3**	**4**	**5**	**6**	**7**	**8**	**9**	**10**	**11**	**12**
Odd	$5\downarrow$	$5\uparrow$	$3\downarrow$	$3\uparrow$	$1\downarrow$	$1\uparrow$	$-1\downarrow$	$-1\uparrow$	$-3\downarrow$	$-3\uparrow$	$-5\downarrow$	$-5\uparrow$
Even	$6\uparrow$	$4\downarrow$	$4\uparrow$	$2\downarrow$	$2\uparrow$	$0\downarrow$	$0\uparrow$	$-2\downarrow$	$-2\uparrow$	$-4\downarrow$	$-4\uparrow$	$-6\downarrow$

Table 3: Mapping of chip modes to the walk position and coin states for even and odd steps.

Notably, it is not possible to access both coin states for positions ±6 as they would exceed the physical boundary of the chip. However, this is not a problem in our case as states $|6\downarrow\rangle$ and $|-6\uparrow\rangle$ can be populated only from step 8 on.

At this point we take into account walks of single photons. Here we consider walks with input states $|0\downarrow\rangle$ and $|0\uparrow\rangle$, which correspond to sending a single photon from the source to input 1 or 2 which are then routed to modes 6 and 7.
Figs. 37b and 37a show the measured output position probabilities for every step of the

walk compared with the expected ones, up to step six. Each position-coin output is accessed by an individual routing unitary that directs the corresponding mode (see Table 3) to mode one which is connected to an SNSPD. This means that each row of Figs. 37b and 37a requires 12 measurements. Running the source at a mean photon number of 0.01, considering that we have a total transmission efficiency from source to detection of $\approx 20\%$ and that we run the system at 76 MHz, we expect a total single photon rate of 170 kHz. This means that integrating each output for one second we expect on average to record 1400 events and a relative error of $\leq 1\%$. However, the real duration of each measurement is set to 7 s as the chip requires ≈ 4 s to stabilize when switching from a unitary setting to next one. Therefore, a complete measurement of an Hadamard walk of six steps with these settings requires approximately 8 minutes. The collected data show an overall similarity with respect to the theory up to 99.5% and show the expected coin dependence on the shape of the output probability. In fact, we see how the walker starting with an $|\uparrow\rangle$ ($|\downarrow\rangle$) coin shows probability peaks located towards positive (negative) positions on the discrete line.

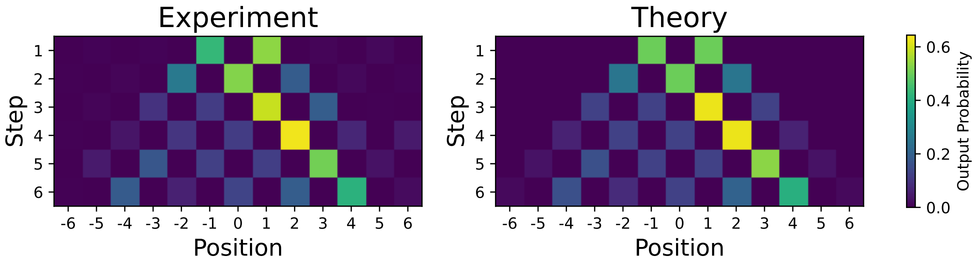

(a) Walk initiated in state $|0\uparrow\rangle$, theory and experiment show a similarity of 99.47%.

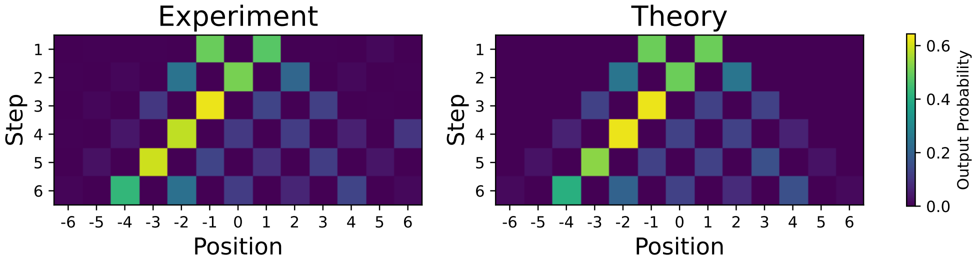

(b) Walk initiated in state $|0\downarrow\rangle$, theory and experiment show a similarity of 99.46%.

Figure 37: Single photon Hadamrd Quantum Walks performed in the photonic network using input and output unitary routing.

The good agreement between experiment and theory proves how, adopting routing it is possible to obtain an optimal wave-like interference pattern following the one predicted by an Hadamard walk.

In order to probe quantum interference happening within the walk we perform a two particle walk using a pair of indistinguishable photons. Once again we use HOM interference to synchronize the photons and set them to an optimal level of indistinguishability, which, given the photon spectral features at the time of the measurement, was limited to $\approx 90\%$.

With particle indistinguishability set, we send the two photons to the network where they are routed to the central modes and undergo a six-step Hadamard walk. In order to detect the output, we must evaluate two-fold coincidences among all output pairs which require using three detectors in the same configuration shown in Fig. 18. Running the experiment with the same mean photon number and repetition rate used for the single photon walk we expect a total two-photon rate of 38 kHz resulting on average in approximately 300 coincidences per mode combination when integrating for 1 second. Considering that in order to reconstruct the complete two photon output we require 144 measurements per step, using the same settings discussed for the single photon walk, a measurement up to 6 steps requires a total of 100 minutes. Fig. 38 shows the measured coin- and position-resolved two photon output distribution for step six in comparison with the simulated one. Experiment and Theory show a similarity of 90.03%, here the simulation does not take into account the reduced spectral indistinguishability.

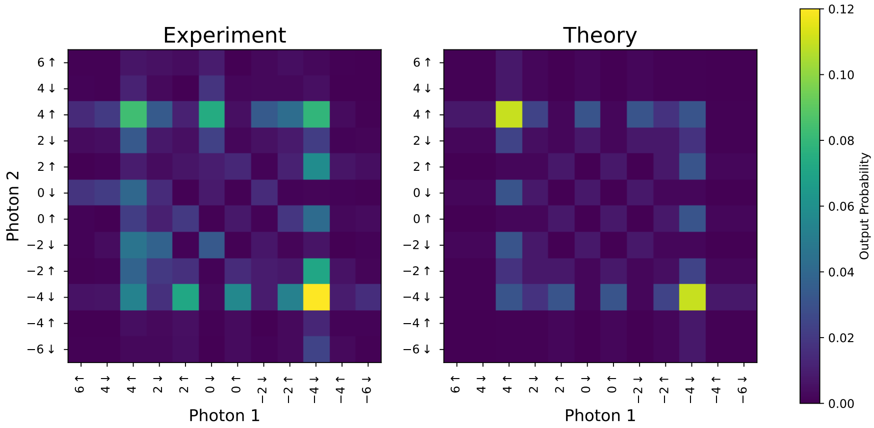

Figure 38: Experimentally measured and theoretically expected output distribution for an Hadamard walk of two photons with input $|0\uparrow\rangle \otimes |0\downarrow\rangle$. Experiment and theory show a similarity of 90.03%.

With this we can conclude that unitary routing is suitable to perform and measure a large photonic evolution in a resource efficient manner. We now move to a sightly different setting where the network is not only performing the routed evolution, but is also programmed to analyze the output.

5.1.3 Bell state generation and quantum state tomography

Stacking several unitaries, we can produce a routing from the physical channels used to feed photons in the network as well as to direct them outside and detect the evolution outcome. Now we show how we can extend this in order to generate a quantum state and perform its tomography.
Starting with a photon pair we can use input routing to path-encode a two-qubit state, which upon undergoing a unitary operation is transformed into a Bell state.
The procedure used is summarized in Fig. 39:

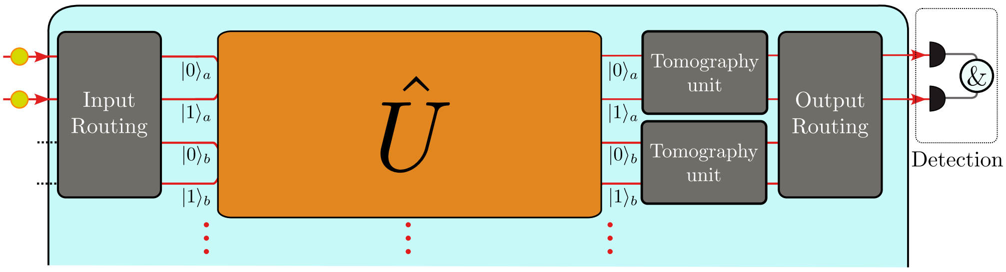

Figure 39: Scheme for on-chip generation and reconstruction of Bell States.

As in all previous cases, photons are sent to inputs 1 and 2 of the network. The two qubits a and b are encoded using modes 1 to 4, whereby the group $(1, 2)$ is reserved to qubit a and group (3,4) to b. In terms of vectors and photonic creation operators this corresponds to the encoding:

$$\begin{aligned} |0\rangle_a &= \begin{pmatrix} 1 \\ 0 \\ 0 \\ 0 \end{pmatrix} = \hat{a}_0^\dagger |\varnothing\rangle, \quad |1\rangle_a = \begin{pmatrix} 0 \\ 1 \\ 0 \\ 0 \end{pmatrix} = \hat{a}_1^\dagger |\varnothing\rangle, \\ |0\rangle_b &= \begin{pmatrix} 0 \\ 0 \\ 1 \\ 0 \end{pmatrix} = \hat{b}_0^\dagger |\varnothing\rangle, \quad |1\rangle_b = \begin{pmatrix} 0 \\ 0 \\ 0 \\ 1 \end{pmatrix} = \hat{b}_1^\dagger |\varnothing\rangle. \end{aligned} \tag{120}$$

In this sense, the four column vectors correspond to sending a single photon to the corresponding mode of the network, which is achieved by the input routing unitary. Right after that, a unitary $\hat{U}$ is applied. This unitary produces the target Bell state starting from the two-qubit computational basis. For instance, we can consider the operation:

$$\hat{M} = \frac{1}{\sqrt{2}} \begin{pmatrix} 0 & 0 & 1 & 1 \\ 1 & 1 & 0 & 0 \\ 1 & -1 & 0 & 0 \\ 0 & 0 & 1 & -1 \end{pmatrix}. \tag{121}$$

When $\hat{M}$ is applied to the four vectors of Eq. (120), it maps the creation operators associated to each mode in the following way:

$$\begin{aligned} \hat{a}_0^\dagger &\rightarrow \frac{\hat{a}_1^\dagger + \hat{b}_0^\dagger}{\sqrt{2}}, \quad \hat{a}_1^\dagger \rightarrow \frac{\hat{a}_1^\dagger - \hat{b}_0^\dagger}{\sqrt{2}}, \\ \hat{b}_0^\dagger &\rightarrow \frac{\hat{a}_0^\dagger + \hat{b}_1^\dagger}{\sqrt{2}}, \quad \hat{b}_1^\dagger \rightarrow \frac{\hat{a}_0^\dagger - \hat{b}_1^\dagger}{\sqrt{2}}. \end{aligned} \tag{122}$$

Therefore, the combinations of creation operators $\hat{a}_0^\dagger \hat{b}_0^\dagger$, $\hat{a}_0^\dagger \hat{b}_1^\dagger$, $\hat{a}_1^\dagger \hat{b}_0^\dagger$, $\hat{a}_1^\dagger \hat{b}_1^\dagger$, which generate the four basis states of the two-qubit computational basis, evolve into:

$$\begin{aligned} \hat{a}_0^\dagger \hat{b}_0^\dagger &\rightarrow \frac{1}{2}(\hat{a}_0^\dagger \hat{a}_1^\dagger + \underline{\hat{a}_0^\dagger \hat{b}_0^\dagger} + \underline{\hat{a}_1^\dagger \hat{b}_1^\dagger} + \hat{b}_0^\dagger \hat{b}_1^\dagger), \\ \hat{a}_0^\dagger \hat{b}_1^\dagger &\rightarrow \frac{1}{2}(\hat{a}_0^\dagger \hat{a}_1^\dagger + \underline{\hat{a}_0^\dagger \hat{b}_0^\dagger} - \underline{\hat{a}_1^\dagger \hat{b}_1^\dagger} - \hat{b}_0^\dagger \hat{b}_1^\dagger), \\ \hat{a}_1^\dagger \hat{b}_0^\dagger &\rightarrow \frac{1}{2}(\hat{a}_0^\dagger \hat{a}_1^\dagger - \underline{\hat{a}_0^\dagger \hat{b}_0^\dagger} + \underline{\hat{a}_1^\dagger \hat{b}_1^\dagger} - \hat{b}_0^\dagger \hat{b}_1^\dagger), \\ \hat{a}_1^\dagger \hat{b}_1^\dagger &\rightarrow \frac{1}{2}(\hat{a}_0^\dagger \hat{a}_1^\dagger - \underline{\hat{a}_0^\dagger \hat{b}_0^\dagger} - \underline{\hat{a}_1^\dagger \hat{b}_1^\dagger} + \hat{b}_0^\dagger \hat{b}_1^\dagger). \end{aligned} \tag{123}$$

The underlined contributions shown in Eq. (123) correspond to cases where each mode pair is populated by a single photon and therefore represent a valid two-qubit state in our encoding. Postselcting on these cases, the input is transformed into $|\phi^\pm\rangle$ with a probability of $\frac{1}{2}$. This means that to generate two out of the four Bell states we can set $\hat{U} = \hat{M}$ and post-select on events where the encoding is preserved. The remaining two Bell states can be then generated starting from $|\phi^\pm\rangle$ by flipping the state of qubit a and leaving b unchanged, which corresponds to setting $\hat{U} = (\hat{\sigma}_x^{(a)} \otimes \mathbb{I}^{(b)})\hat{M}$.
In summary, the four Bell states are generated probabilistically according to the following mapping:

$$\begin{aligned} |00\rangle &\xrightarrow{\hspace{1cm}\hat{M}\hspace{1cm}} |\phi^+\rangle, \\ |01\rangle &\xrightarrow{\hspace{1cm}\hat{M}\hspace{1cm}} |\phi^-\rangle, \\ |00\rangle &\xrightarrow{(\hat{\sigma}_x^{(a)} \otimes \mathbb{I}^{(b)})\hat{M}} |\psi^+\rangle, \\ |01\rangle &\xrightarrow{(\hat{\sigma}_x^{(a)} \otimes \mathbb{I}^{(b)})\hat{M}} |\psi^-\rangle. \end{aligned} \tag{124}$$

In order to verify the correct generation of the states we reconstruct the density operator associated to the state emerging from the action of $\hat{U}$.
As discussed in subsection 3.3.4, to reconstruct the density operator associated to a two-qubit state we need to measure the expectation values: $\langle \hat{\sigma}_i^{(a)} \otimes \hat{\sigma}_j^{(b)} \rangle$. This is achieved applying tomographic unitaries to the two qubits in order to project the state on the eigenbasis of $\hat{\sigma}_i^{(a)} \otimes \hat{\sigma}_j^{(b)}$. As shown in Fig. 39, we program the network to implement the tomographic unitaries after $\hat{U}$. As in the case of routing, this can be

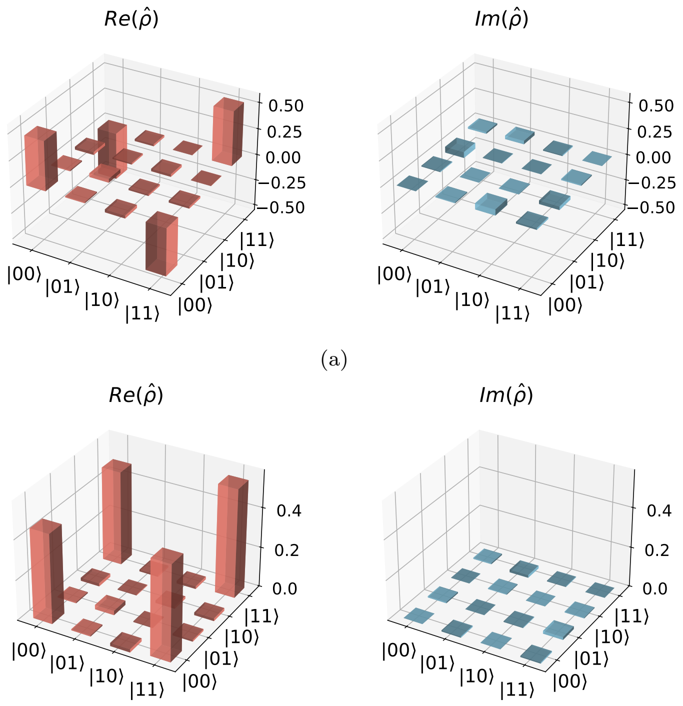

(a)

(b)

Figure 40: **(a):** Real and imaginary part of the reconstructed $|\phi^-\rangle$ state. **(b):** Real and imaginary part of the reconstructed $|\phi^+\rangle$ state.

done because the product of $\hat{U}$ and the basis change required to run the tomography is again a unitary operation of the same size of $\hat{U}$. With this, for each tomographic setting, the network directly sends out a state expressed in the required Pauli basis. In order to reconstruct $\langle \hat{\sigma}_i^{(a)} \otimes \hat{\sigma}_j^{(b)} \rangle$, we record the four coincidence count rates: $C_{1,3}$, $C_{1,4}$, $C_{2,3}$, $C_{2,4}$, where the indices correspond to the network modes. To do this it is sufficient to use two detectors and program a suitable routing unitary connecting the mode pair under investigation to the outputs used to perform the detection.
Figs. 40 and 41 show the reconstructed density operators compared to the theoretically expected ones. Agreement between theory and reconstructed density matrices can be quantified by the quantum state fidelity [134, 105], generally defined as:

$$\mathcal{F}(\hat{\rho}_{theo}, \hat{\rho}_{exp}) = Tr\left(\sqrt{\sqrt{\hat{\rho}_{theo}}\hat{\rho}_{exp}\sqrt{\hat{\rho}_{theo}}}\right)^2, \tag{125}$$

where here $\sqrt{\cdot}$ indicates the square root of a matrix.
Since in our case we compare the reconstructed density operators to pure states, $\hat{\rho}_{theo}$ is of the form: $\hat{\rho}_{theo} = |\psi\rangle\langle\psi|$. Considering that $\hat{\rho}_{exp} = \sum_i p_i |\phi_i\rangle\langle\phi_i|$ for a given ensemble of states $\{|\phi_i\rangle\}$, making use of the fact that $\sqrt{|\psi\rangle\langle\psi|} = |\psi\rangle\langle\psi|$ and using the properties

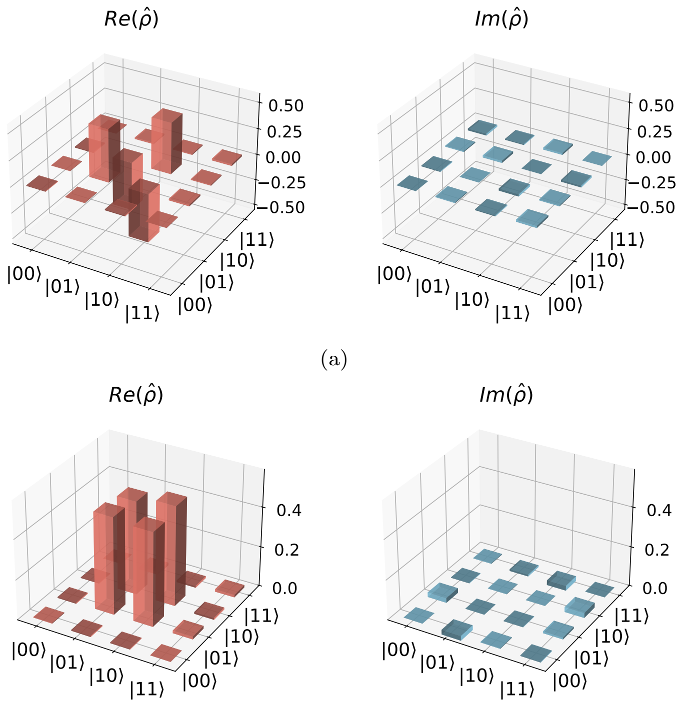

(a)

(b)

Figure 41: **(a):** Real and imaginary part of the reconstructed $|\psi^-\rangle$ state. **(b):** Real and imaginary part of the reconstructed $|\psi^+\rangle$ state.

of the trace of a matrix, the expression of $\mathcal{F}$ simplifies in the following way:

$$\begin{aligned}\mathcal{F} = Tr\left(\sqrt{|\psi\rangle\langle\psi|\rho_{exp}|\psi\rangle\langle\psi|}\right)^2 = Tr\left(\sqrt{\sum_i p_i|\langle\psi|\phi_i\rangle|^2|\psi\rangle\langle\psi|}\right)^2 = \\ = \sum_i p_i|\langle\psi|\phi_i\rangle|^2 Tr(|\psi\rangle\langle\psi|)^2 = \langle\psi|\hat{\rho}_{exp}|\psi\rangle.\end{aligned} \tag{126}$$

Evaluating this expression for reconstructed states we obtain the fidelities listed in Table 4. From the obtained fidelities we extract an average value of $(96.0 \pm 0.5)\%$. A recent work by Zatsch *et al.*[135] has shown an average quantum state fidelity of 97.7% for the four Bell states using a similar integrated platform capable of generating and reconstruct an arbitrary two-qubit state. Although slightly lower than the one showed in the aforementioned work, we find that our average fidelity compares favorably

	$\lvert\phi^-\rangle$	$\lvert\phi^+\rangle$	$\lvert\psi^-\rangle$	$\lvert\psi^+\rangle$
$\mathcal{F}$ [%]	95.0 ± 0.6	96.9 ± 0.5	96.0 ± 0.3	96.1 ± 0.3

Table 4: Quantum state fidelities of the reconstructed Bell states

especially considering that our system can handle up to six qubits.
In conclusion, this shows that exploiting the unitary nature of routing and tomographic operations to constitute an overall operation with the one under analysis is a viable way of investigating photonic evolution networks in a resource efficient fashion.
This concludes this section where the behavior of the photonic network has been examined. In the next one we apply some of the concepts tested here to the investigation of the dynamics of an Hadamard walk with losses.

5.2 Open system dynamics in multi-particle quantum walks

The introduction of multiple photons is essential in all quantum communication and computation schemes based on optical networks [87, 136, 137]. The strongest effect that prevents the scaling to many particles are losses due to non-ideal efficiencies of the network components and the measurement devices. In particular, the total transmission efficiency of any optical device decreases exponentially with the number of traveling photons. Additionally, single photon sources are probabilistic in nature, which further reduces the chance of detecting a particle at the end of an experiment. In order to overcome losses, technological advances, such as in the engineering of better and more efficient quantum sources and detectors and almost loss-free optical components are pushed forward, aiming at on-demand photon sources and ideal network properties. In addition, post-selection on coincidence events involving the targeted number of photons provides a valid selection criterion for a successful measurement run, in which all initiated walkers have arrived at their final step. Nevertheless, under certain conditions the introduction of controlled losses in a network is even indispensable to model physical effects, e.g. recurrence phenomena [138, 139, 140], non-hermitian evolutions and parity-time symmetry [141, 142, 143, 144, 145, 146], or invasiveness of quantum measurements [147].

For these reasons, here we study the fundamental effect of mode dependent particle losses in an Hadamard walk of two indistinguishable photons, implemented both in the integrated chip and in a modified version of the time-multiplexed setup. In order to do this, we have devised a method to perform a quantum walk of n temporal steps where we can insert losses at a time step $m < n$ on a selected propagation mode in a controlled way and successively detect the output single particle distributions resulting from the remaining unperturbed dynamic.

5.2.1 Modelling of loss mechanism

Let us start by illustrating the loss mechanism that allows us to implement losses within the walk in a controlled way. In particular, let us consider the scheme shown in Fig. 42, where we show a two-photon walk of s steps with a loss happening at step s_l. The evolution before and after s_l is unitary and corresponds to the one induced by coin and shift operation, therefore: $\hat{U}(0 \to s_l) = (\hat{S}\hat{C})^{s_l}$ and $\hat{U}(s_l \to s) = (\hat{S}\hat{C})^{s-s_l}$. The two unitaries involve a set of system modes corresponding to the walk's coin-position states $|x, c\rangle$. In addition to the system modes we consider an ancillary channel $|aux\rangle$, which is not populated at the beginning of the evolution. A loss happening at step s_l on the system mode identified by position and coin x_l and c_l, is modelled by the action of a beam splitter with reflectivity r and transmissivity t involving modes $|x, c\rangle$ and $|aux\rangle$, which is represented by the operator:

$$\hat{L}(x_l, c_l) = r(|x_l, c_l\rangle\langle x_l, c_l| - |aux\rangle\langle aux|) + t(|x_l, c_l\rangle\langle aux| + |aux\rangle\langle x_l, c_l|). \tag{127}$$

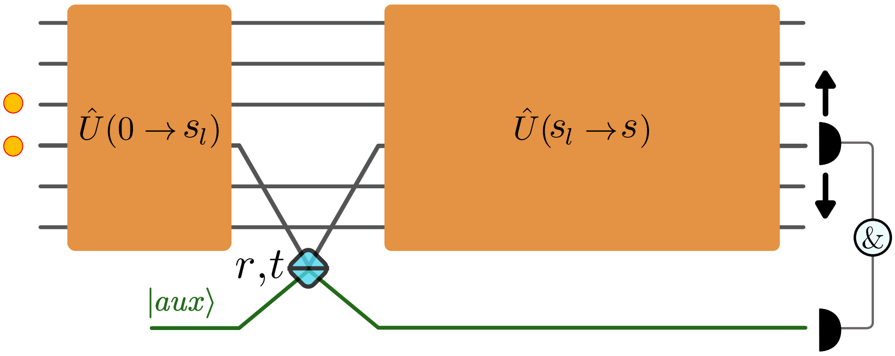

Figure 42: Path encoded scheme for the insertion of controlled losses. The system evolving is couped to an auxiliary mode by a beam splitter . The lossy dynamics is retrieved post-selecting on events where a photon is in the auxiliary mode and the other in one of the system outputs.

Therefore, the overall evolution is given by the unitary operation involving both system and ancillary modes:

$$\hat{\mathcal{U}}(s \,|\, s_l, x_l, c_l) = (\hat{S}\hat{C})^{s-s_l}\hat{L}(x_l, c_l)(\hat{S}\hat{C})^{s_l}. \tag{128}$$

We are interested in reconstructing the output probability for the surviving photon given that the other one has been lost at a given step and mode. As shown in Fig. 42 this can be achieved measuring events where one particle is detected on the ancillary mode and the other in one of the system outputs. Mathematically, this is implemented by the two-photon projector:

$$\hat{\Pi}(x, c) = |aux, (x, c)\rangle\langle aux, (x, c)| + |(x, c), aux\rangle\langle(x, c), aux|, \tag{129}$$

where the order within the kets and bras corresponds to particle 1 and 2.
With this, the probability amplitude relative to a photon propagating up to step s and mode $|x, c\rangle$, conditioned to a loss that happened at step s_l on mode $|x_l, c_l\rangle$ are given by:

$$\pi(x, c, s \,|\, x_l, c_l, s_l) = \langle\hat{\Pi}(x, c)[\hat{\mathcal{U}}(s \,|\, s_l, x_l, c_l)]^{\otimes 2}\rangle, \tag{130}$$

where the expectation value is calculated on the two-photon input state.
From the amplitudes we obtain the target conditional probability distribution for the surviving photon:

$$P(x, c, s \,|\, x_l, c_l, s_l) = \frac{|\pi(x, c, s \,|\, x_l, c_l, s_l)|^2}{\sum_{x', c'} |\pi(x', c', s \,|\, x_l, c_l, s_l)|^2}, \tag{131}$$

where the sum appearing in the denominator ensures that $P(x, c, s \,|\, x_l, c_l, s_l)$ is normalized to 1.
This conceptual scheme can be implemented both in the photonic network and the time-multiplexed setup.

5.2.2 Open dynamics in the photonic network

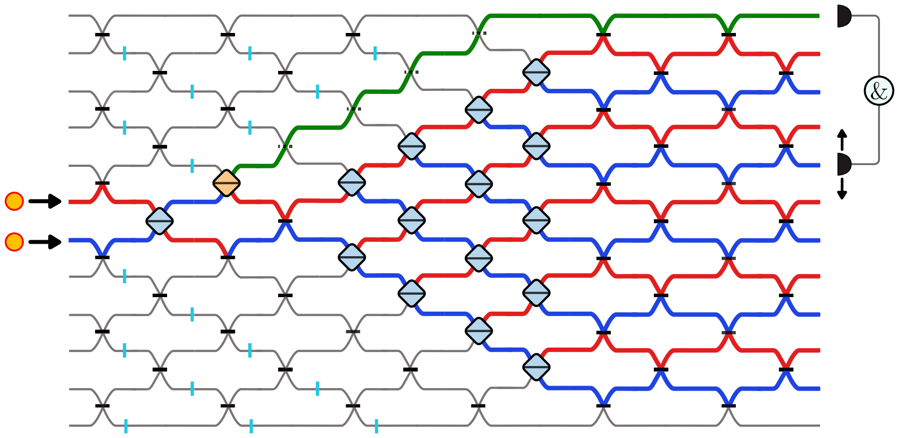

Figure 43: Sketch of the lossy walk implemented using the path encoded photonic network. One of the modes within the network serves as ancillary mode which is coupled to one of the system modes using a beam splitter to implement losses. This beam splitter may be programmed at any point of the network. The output distribution for the surviving particle is measured recording coincidences between system outputs and ancillary mode.

The interferometer shown in Fig. 43 implements a possible instance of the scheme shown in Fig. 42. In particular, here we see that the loss is happening right after step 1, however it can be implemented in any other mode or step setting the desired unitary $\hat{\mathcal{U}}(s \,|\, s_l, x_l, c_l)$ to the chip. What is important to note here is that one mode of the chip has to be employed to implement the ancillary mode where the lost photon will go and is used to perform the conditioning. As a result, the space available to the actual walk is reduced: in fact, with the 12×12 system the introduction of a loss channel reduces the amount of steps that can be performed from six to five.
Besides that, input and output routing can be applied without any restriction and in fact we use input routing in the same way as seen in the previous section. Output routing is employed to detect coincidences between the ancillary mode (output 1) and the walk outputs (modes 2 to 11). Since here the walk is path encoded, when referring to its modes within this system we denote the coin states with $|\uparrow\rangle$ and $|\downarrow\rangle$ as we have done previously.
Analogously to what we have seen in the previous section, the path encoded platform can run at a repetition rate of 76 MHz, with an expected average amount of coincidences of 300 per second on each mode pair when operating the source at a mean photon number of 0.1. For each step s, the loss mode can be located on any of the $s(s+1)$ modes between step 1 and s. Given a loss setting, the distribution for the surviving photon is obtained recording coincidences between the ancillary mode and the remaining 10 possible quantum walk outputs. This means that at each step, $10s(s+1)$ unitaries must be set to implement all possible loss modes and routings, resulting in a total of 700 settings required to measure all the conditioned distributions from step 1 to 5. As in the case of the plain Hadamard, each measurement lasts 7

seconds, therefore a complete data acquisition requires up to 80 minutes.

5.2.3 Open dynamics in the time-multiplexed setup

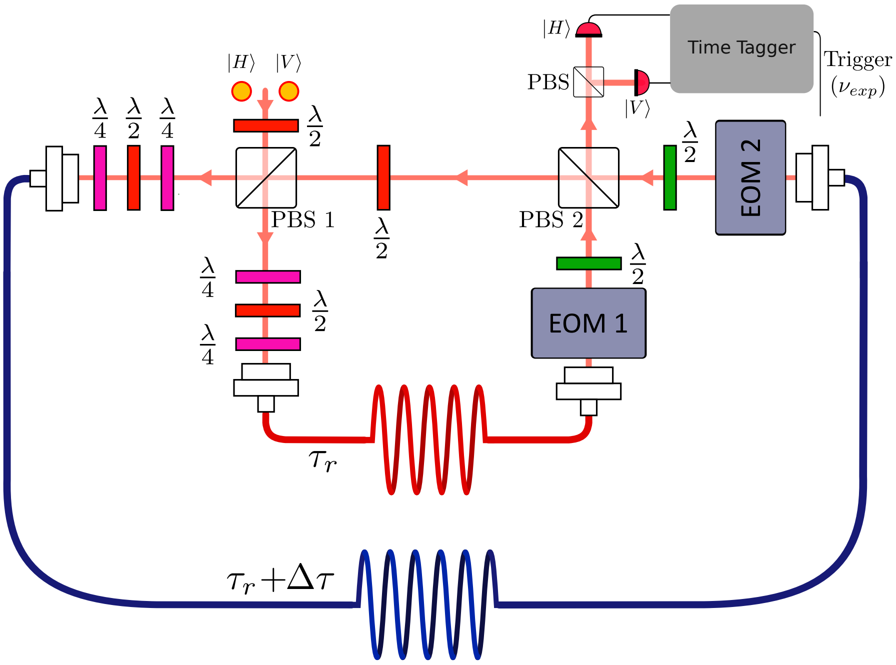

Figure 44: Sketch of the lossy walk implemented using the active time-multiplexed setup. Inserting losses is possible using two waveplates after EOMs 1 and 2. The two waveplates are set at 11.4° and cause 15% of the light to be sent outside the setup. The lossy dynamics is recovered post-selecting on events where one photon is out-coupled at a time-bin relative to $|x_l, c_l\rangle$ and the remaining one is sent out at a later step.

Fig. 44 shows the setup used to implement the lossy dynamics in time. Since we perform an Hadamard walk, instead of using an EOM, the coin is realized by a $\frac{\lambda}{2}$ waveplate with its axis at 22.5°, which implements $\hat{C}_H$ in polarization. Additionally, two waveplates (green $\frac{\lambda}{2}$ in the sketch) with axis set at 11.4° are positioned after EOMs 1 and 2. After the initial in-coupling carried out by the EOMs, only H- and V-polarized photons travel in the long and short loop, respectively. Because of the two waveplates, before reaching PBS 2, V- (H-) photons from the short (long) loop are put in an 85:15 superposition of V and H (H and V). This means that at each roundtrip a photon coming form any of the two loops proceeds to the feedback with 85% probability or is sent out with 15% probability. In the former case the photon continues and perform an additional step in the walk, while in the latter it goes to a polarizing beam splitter which directs it to one of two SNSPDs.

Using a time tagger we can record all the events relative to time-bins encoding the positions of the walk at every step. To do this, besides the signals form the two detectors, the time tagger receives the experimental trigger at frequency ν_{exp} generated by the clock multiplier discussed in subsection 4.3.5. If we send only $|H\rangle$ photons to the setup while running the source at ν_{exp} without performing any in-coupling, we can determine the time t_{off} between a trigger event and the earliest time-bin of the first roundtrip. This corresponds to position $x = -1$ of at step $s = 1$, knowing the time-bin separation $\Delta\tau = 170\ ns$ and that the time required to travel in the short loop is $\tau_r = 5.3\ \mu s$, position x at step s is mapped to an arrival time $t_{s,x}$ given by:

$$t_{s,x} = t_{off} + (s-1)\tau_r + \frac{s+x}{2}\Delta\tau \tag{132}$$

In order to perform the lossy evolution we enter the setup with a photon pair generated by the SPDC source and record only events relative to the times defined by Eq. 132 from step 1 to s_{max}. In order to condition only on cases where a photon was lost at step s_l on mode $|x_l, c_l\rangle$, while the second made it to step s, we post-select on events were a single photon was detected at time t_{s_l,x_l} with polarization given by c_l, while the second has been detected at times $t_{s,x}$ with $x \in \{-s, s\}$ in any of the two possible polarizations.
Since in this implementation the coin is encoded in polarization, the coin state is denoted with $|H\rangle$ and $|V\rangle$ in results obtained using the time-multiplexed platform.

5.2.4 Achievable rates in the time-multiplexed architecture

Considering that the roundtrip time is $\approx 5\,\mu s$, and that the electro-optical modulators in the loop have a limited continuous operation rate of 1 MHz, in order to perform a walk up to 10 steps the experimental rate is limited to $\approx 13\ kHz$. In addition, we must consider that in the time-multiplexed setup, losses scale exponentially with the number of steps performed, in particular we can calculate the probability that a single photon is detected after n steps as:

$$p_n = \eta_{ppKTP} \cdot \eta_{in} \cdot (\eta_{loop} \cdot (1-\eta_{out}))^{n-1} \cdot \eta_{out} \cdot \eta_{fiber} \cdot \eta_{det}, \tag{133}$$

where, in the setup used here, $\eta_{ppKTP} = 70\%$ is the transmission of the ppKTP waveguide, $\eta_{in} = 41\%$ is the transmission from waveguide to setup, $\eta_{loop} = 80\%$ is the loop efficiency, $\eta_{out} = 15\%$ is the outcoupling rate, $\eta_{fiber} = 70\%$ is the coupling efficiency from setup to the detection fibers and $\eta_{det} = 90\%$ is the detection efficiency. The transmission efficiency η_{in} includes 90% transmission of the spectral filter, 65% transmission in the KTP compensation crystal and 70% incoupling to the fibers realizing the loops within the setup. The reduced transmission of the KTP crystal used here is mainly due to the fact that its cross-section of $1 \times 1\ mm^2$ is slightly smaller than the beam coming from the waveguide. It must be noted that, this is not the compensation crystal discussed in subsection 4.1.4, which was not available at the time of this experiment. Besides having a smaller coross-section, this KTP crystal had a length of 12.5 mm which is 1.8 mm longer than the optimal length found performing the measurement discussed in subsection 4.1.4. Therefore, in this case, the photon indistinguishability was reduced to only 93%.

With these values for the efficiencies, considering an experimental repetition rate $\nu_{exp} = 13\ kHz$ and a mean photon number for the source $\langle n \rangle = 0.1$, the coincidence rate for events involving photons travelling n and m roundtrips is given by:

$$c_{n,m} = \nu_{rep} \langle n \rangle p_n p_m. \tag{134}$$

Considering a measurement time of 60 hours and an evolution up to 10 steps, using this relation we can calculate the total amount of two-photon events for all possible loss scenarios, whose values are listed in table 5. Since at each step s photons can occupy $2s$ positions, if a particle is lost at step s_{loss} while the other is detected at step s_{out}, the total two-photon events are distributed over a total $4 s_{out} \cdot s_{loss}$ combinations. If all combinations were equiprobable, this would mean that starting from $s_{loss} = 5$ we would expect ≤ 10 coincidences per possible outcome starting from $s_{out} = 9$, which would signify that not enough statistics is accumulated for the reconstruction of the lossy dynamics. In particular, setting the threshold at 10 coincidences per combination, a measurement time 10 times longer would be required, rendering the measurement unfeasible.

s_{out}	s_{loss}								
	1	2	3	4	5	6	7	8	9
2	140111								
3	95276	64788							
4	64788	44056	29958						
5	44056	29958	20371	13852					
6	29958	20371	13852	9420	6405				
7	20371	13852	9420	6405	4356	2962			
8	13852	9420	6405	4356	2962	2014	1370		
9	9420	6405	4356	2962	2014	1370	931	633	
10	6405	4356	2962	2014	1370	931	633	431	293

Table 5: Expected total two-photon counts for all possible combinations where a photon travels up step s_{out}, while the other is lost at step s_{loss} (with $1 \leq s_{loss} \leq s_{out} - 1$). The amount of clicks is estimated considering an experimental rate of 13 kHz and an integration time of 60 hours.

However, as we have seen in the introduction, rater than being flat, the probability distribution for an Hadamard walk typically features higher peaks for a subset of positions. This further affects the expected coincidence rates between s_{loss} and s_{out}, making more likely to observe patterns relative to peaks in the distribution of the photon that was detected earlier. Therefore, an average reduced count rate does not imply that all loss patterns will be underrepresented. For this reason and since it is not feasible to run the experiment for months, we will stick to the 60 hours considered here for the time-multiplexed platform even if not all output distributions are expected to exhibit a high enough statistics.

5.2.5 Conditioned dynamics

At this point examine the effect of conditioning on various modes of the walks during its evolution. We first look at what happens when the loss occurs at an early stage of the walk, namely at step one. After that we focus on cases where a photon is lost later. Then we investigate the effects of losses on the walk's spread, and finally we show how discarding knowledge about the loss mode affects the walk's output.

First step:
The simplest setting in the conditional statistics is the conditioning on the loss of a particle in one of the two available modes $(-1, \downarrow)$ and $(1, \uparrow)$ at step 1. In Fig. 45 we present this evolution for both conditioning modes measured using the photonic network for the five achievable steps. Analogously to what was shown in Fig. 37, each row of the plot corresponds to the position probability distribution for a step.

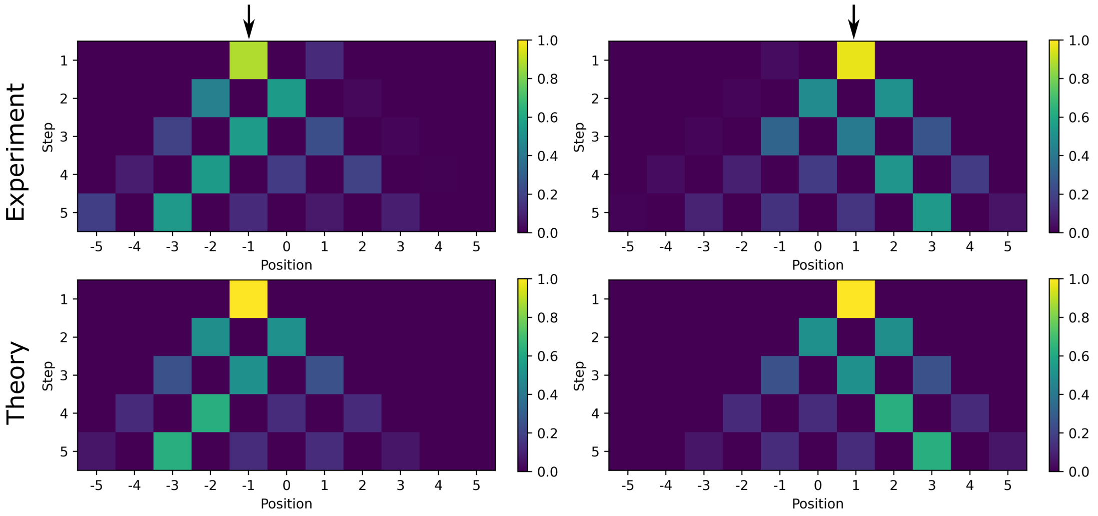

Figure 45: Conditioning for step 1 recorded using the photonic network. The arrows mark the conditioning mode $(-1, \downarrow)$ (left column) and $(1, \uparrow)$ (right column) in the experiment (upper) and theory (lower row). The similarities between experimental probability distribution and theoretical prediction are 98.66% and 98.03%, respectively.

The most striking feature of the two distributions is their clear asymmetry. This is an effect of the initial HOM interference happening at the first step of the walk: because of it, the two photons are in a *N00N* state after the first beam splitter. Therefore, loosing one of them in one mode localizes the other on the same mode and the output distributions are the same as the ones of a four steps Hadamard walk of a single walker starting at position ±1. With this setting we are able to see the effects of photon bunching.
The comparisons with the theory find similarities of 98.66% and 98.03%, respectively.

In Fig. 46 we show the same conditional probabilities measured with the time-multiplexed setup. As in this case the walkers' coins are encoded in their polarization, we refer to the loss modes as $(-1, H)$ and $(1, V)$. Similarly to the chip's case, we can observe the same bunching and localization behavior with similarities between theory and experiment of 96.05% and 93.87%. At the same time exploiting the inherent scalability of the time-multiplexed architecture we are able to record up to 10 steps of the walk.

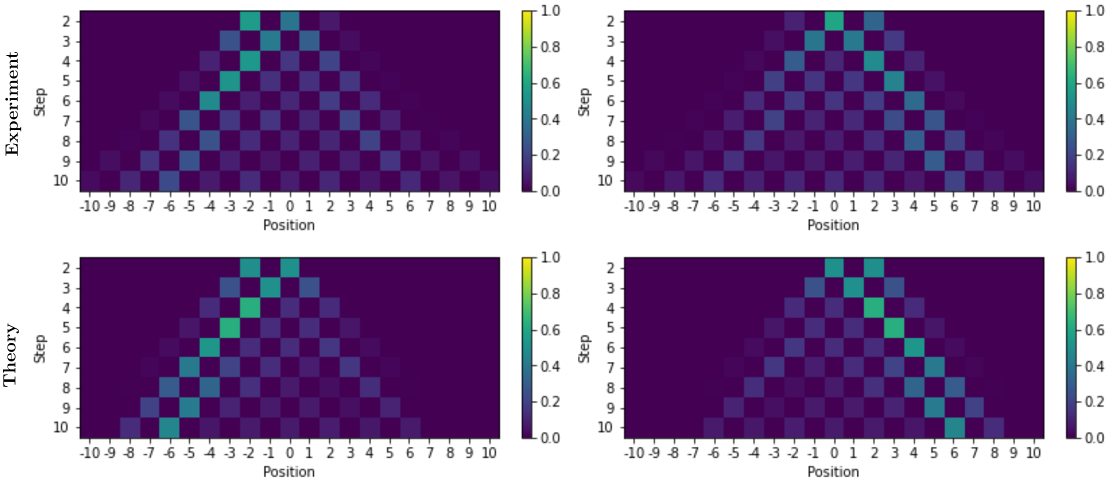

Figure 46: Conditioning for step 1 recorded using the time-multiplexed setup. Similarly to Fig. 45 the plots refer to loss modes $(-1, H)$ (left column) and $(1, V)$ (right column) in the experiment (upper) and theory (lower row). The similarities between experimental probability distribution and theoretical prediction are 96.05% and 93.87%, respectively.

Later steps:
In Figs. 47 and 48 we present 4 probability distributions of the dynamic conditioning in steps 3, 4, and 5 and various modes measured with the two setups. In particular, the ones shown in Fig. 47 are measured using the photonic network: the two top ones show two output distributions that correspond to cases where one photon was lost in step 3 and the other is measured in step 4, while the bottom ones show two cases where we have lost one photon at step 4 and 5 and the surviving one has been detected at step 5. In Fig. 48 we have the same kind of data taken with the time-multiplexed platform and, starting from the top left one and proceeding clockwise, it shows cases where a photon was lost at step 4, 6, 7 and 3 while the other propagated to steps 7, 8, 9 and 10, respectively. Among all the possible choices we have selected these specific plots to be shown as they provide representative examples of how conditioning impacts on the shape of the output probabilities reconstructed in both setups. The predominant aspect that we want to highlight are the effects of mode dependent losses on the symmetry of the distributions when compared to an unperturbed case. Whereby the unperturbed case is a single photon walk starting at $x = 0$ with a coin in an even superposition state. The upper row of Fig. 47 shows the conditioning in step 3 in mode $(1, \uparrow)$ and

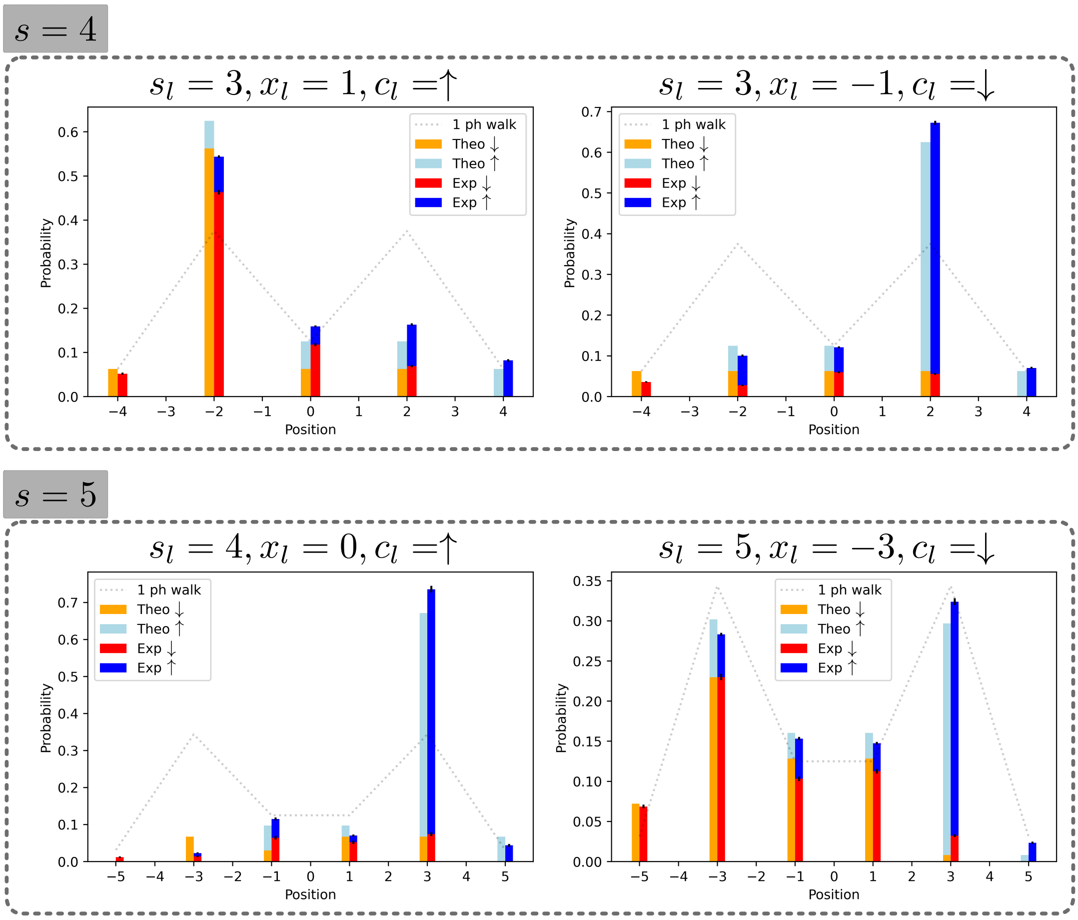

Figure 47: Dynamic conditioning for steps 3,4 and 5 and different conditioning modes as indicated in the titles of the subfigures measured with the integrated network. The similarities between experimental probability distribution and theoretical prediction are 98.44% and 99.63% (upper row), 99.27% and 99.34% (lower row). The gray dotted line in the background indicates the symmetric single photon quantum walk distribution initialized with $|\Psi\rangle = |0\rangle \otimes \frac{|\uparrow\rangle + i|\downarrow\rangle}{\sqrt{2}}$ as a reference.

$(-1, \downarrow)$, respectively. Both distributions appear mirrored, witnessing the high symmetry of the input state and the dynamics. Another case where the dynamic conditioning produces an asymmetrical output at a later step is shown in the bottom left plot of Fig. 47, however, we are able to identify also loss setting for which the output symmetry is not affected by the loss of one particle and closely resembles the single photon case, as shown in the bottom right plot of the same figure. Comparing theory ad experiment we see an average similarity of 99.2% for the plots shown in Fig. 47. Using the time-multiplexed setup we can probe longer evolutions as shown in Fig. 48, where we show output distributions for steps 7, 8, 9 and 10 with various loss settings. Similarly to what was observed using the integrated networks, losses cause asymmetries in the output seeded by the loss of one of the two particles. Also in this case we observe a good agreement between the measured distributions and the

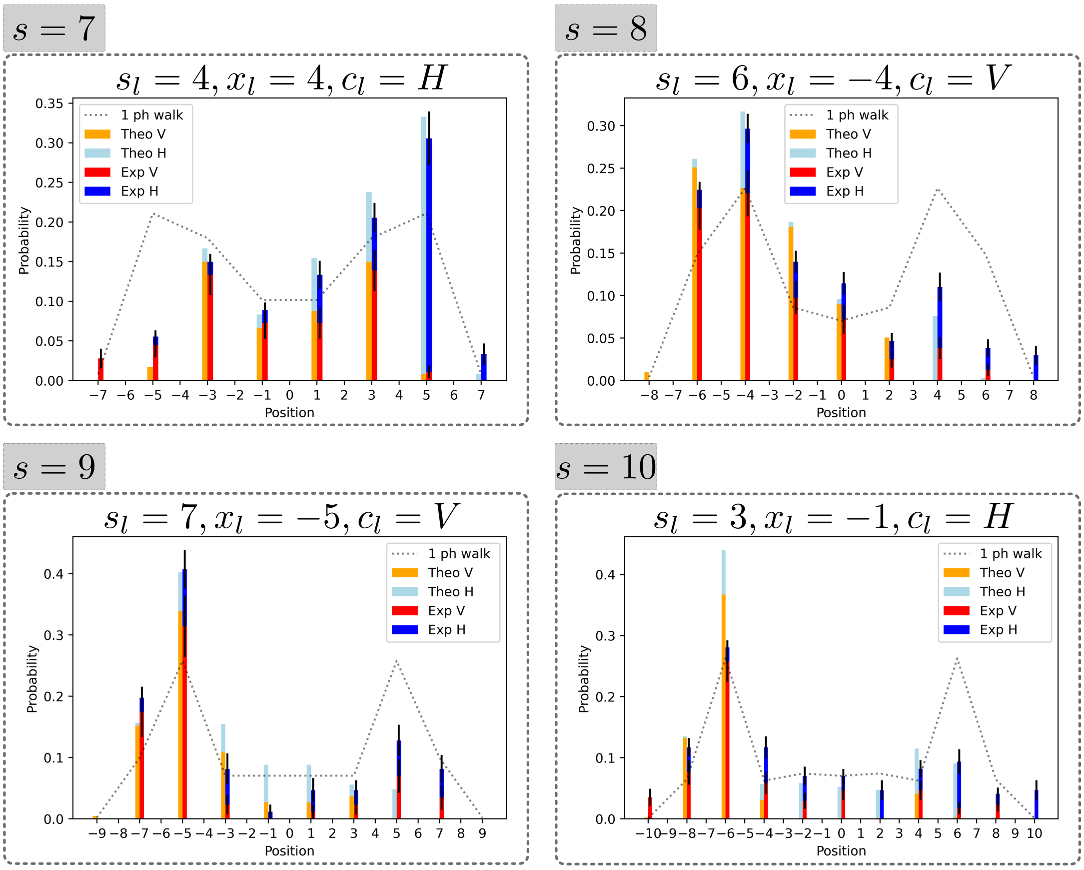

Figure 48: Same as in Fig. 47, but data taken with the TM setup. With this, higher step numbers and larger walks up to 10 steps and 22 modes can be achieved. The similarities between experimental probability distribution and theoretical prediction are 99.51% and 97.77% (upper row), 96.54% and 96.34% (lower row), respectively.

theoretically expected ones.

Walk variances:
After seeing how targeted losses influence the output probabilities, we now discuss how the walks spread is affected by this type of loss.
For a quantum walk we expect a ballistic spread, *i.e.* $\sigma^2(s) \propto s^2$, for the position of a walker after s steps. In Fig. 49 we plot the variance of the distribution of some examples of conditioned dynamics and compare it with the spread of the single particle walk and the two photon walk. We determine the variances as

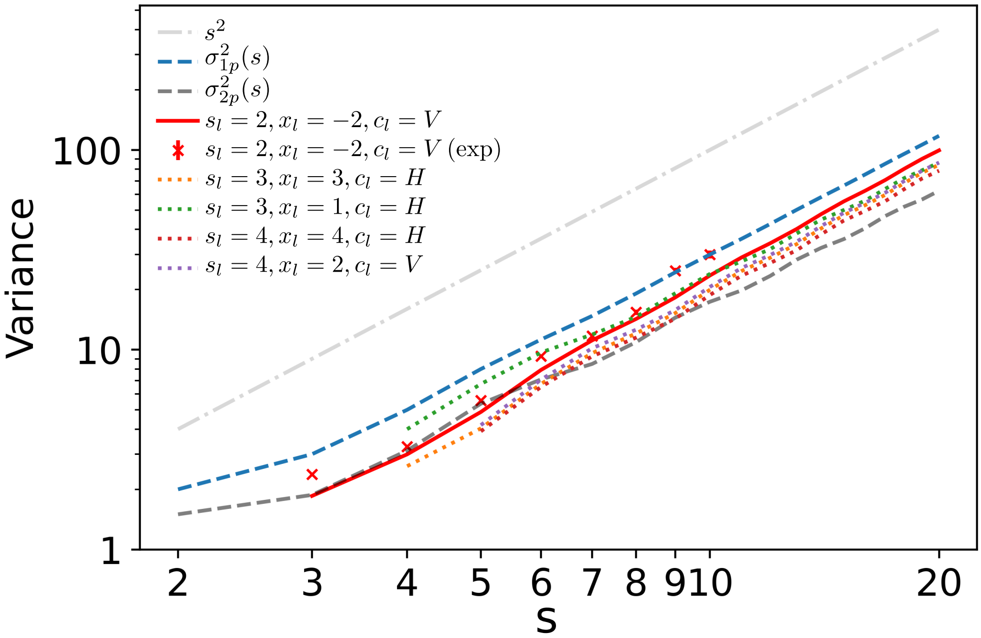

Figure 49: Asymptotic spreading of one photon walk (blue), 2 photon quantum walk (gray), and conditioned walks (dotted lines). The red crosses indicate one exemplary set of experimental data for the conditioning in step 2 and mode $(-2, V)$ in accordance with the theory data (solid red). The gray dotted-dashed line shows a constant slope of 2, the expected ballistic spread.

$$\begin{aligned}
{\sigma^2}_{1p} &= \sum_x x^2 P(x) - \left(\sum_x x P(x)\right)^2 \\
{\sigma^2}_{2p} &= \sum_{(x,y)} \left(\frac{x+y}{2}\right)^2 P(x,y) - \left(\sum_{(x,y)} \frac{x+y}{2} P(x,y)\right)^2 ,
\end{aligned} \tag{135}$$

where $P(x)$ and $P(x, y)$ are generic probability distributions.
The dotted dashed light gray line indicates the ballistic spread with a constant slope of 2. One observes clearly, that after the transient behavior in the first few steps all distributions spread ballistically with the same slope. Thus, a dynamic conditioning does not impact the spreading characteristics of the asymptotic distribution, but just modifies the transient behavior within the first steps. In the same picture we show a set of experimental points (red crosses) obtained employing the TM loop. They show the measured variance trend for the output probability distributions conditioned on losses at step 2 and mode $(-2, V)$ and output steps from 2 to 10 for which we find a good agreement with respect to the respective simulated trend.

Averaging:

Up to this point we have investigated the problem of losses within the walk under the assumption of knowing where a particle has been lost. We now consider what happens when we do not have access to the specific loss mode.
This means we know that there was a loss, but we do not know where. In order to simulate this case, for each step we average the conditioned quantum walk distributions of all possible loss modes, hence obtaining the distributions:

$$\overline{P}(x,c,s) = \frac{1}{\mathcal{N}(s)} \sum_{x_l, c_l, s_l < s} P(x,c,s \,|\, x_l, c_l, s_l), \tag{136}$$

where $\mathcal{N}(s)$ corresponds to the number of modes where a photon can be lost between step 0 and s. In Fig. 50, we show two instances of the average probabilities obtained from the integrated network and time-multiplexed setup. Specifically, Fig. 50a shows the average output at step 5 (measured with the integrated network), while Fig. 50b the same quantity observed at step 7 (measured with the TM loop). Except from noticing the good agreement between experiment and theory, we immediately observe that it is almost impossible to experimentally distinguish the averaged distributions from the unperturbed ones.

In conclusion, here we have developed a formalism that include particle losses in a quantum walk of two photons that may be readily extended to more particles. In addition, we have shown two setups capable of implementing the lossy dynamics using path-encoding and time-multiplexing.
We observe that, knowing where one of the two photons was lost, the output distribution shows pronounced differences with respect to the unperturbed case. We find that averaging over all possible loss modes destroys the effect of the dynamic conditioning and the final distribution cannot be experimentally distinguished from a single particle walk anymore. When focusing on the asymptotic behavior, our simulations show that the conditioning does not influence the ballistic spread of the walker and that after a short transient behavior the variances of the spatial probability distributions grow with the square of the step number.
Although here we use the model to insert losses in a controlled way, the same approach can be applied to the study of recurrence problems where multiple photons propagate in an optical network.

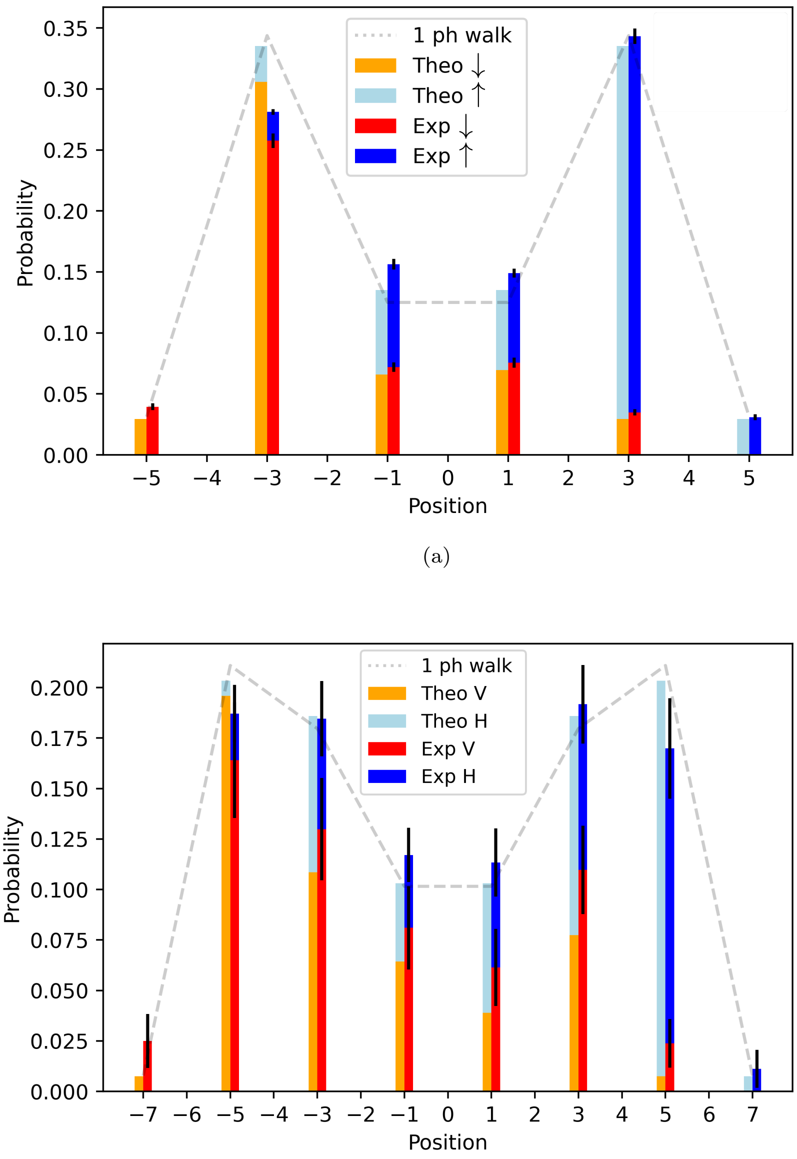

(a)

(b)

Figure 50: **(a):** Dynamic conditioning in step 5 measured with the integrated network averaged over all possible loss modes from step 1 to 4. **(b):** same but for step 7 measured with the TM network averaged over all possible loss modes from step 1 to 6 The similarity between experimental probability distribution and theoretical prediction is 99.41% and 96.87% As above, the dashed line in the background indicates the symmetric single photon quantum walk distribution initialized with an even coin superposition as a reference.

5.3 Entanglement generation in quantum walks

As already discussed from a conceptual point of view in subsection 3.3.5, quantum entanglement is a prime resource for quantum information and computation tasks.
At the same time quantum walks stand out for their suitability for universal quantum computing [148, 149] and have been applied to the development of protocols capable of handling complex computational tasks such as graph search and element distinctness tests [150, 151, 152, 153].
Given the multipartite nature of quantum walkss, it is natural to combine them with the notion of entanglement in order to unfold and enhance their full computational potential. In the case of single particle evolutions, it has been shown theoretically [154] and demonstrated experimentally [155] how interference in quantum walks might lead to the generation mode entanglement among coin and position degree of freedoms of a single walker. As highlighted in [156], this particular flavor of entanglement, often referred to as *classical entanglement*, crucially lacks the non-locality of genuine quantum entanglement, hence it is not suited for all tasks requiring the distribution of parties of an entangled state (e.g. quantum teleportation, entanglement swapping, quantum repeater based communication schemes, etc.).
This is compensated considering quantum walks with many walkers; where the combination of bosonic/fermionic symmetry requirements and projection of one of the joint subspaces involved in the evolution leads to the generation of authentic non-local quantum entanglement [157, 158].

Here we show how, performing a two-photon time-multiplexed Hadamard walk with a measurement induced non-linearity it is possible to entangle the coin degree of freedom of the two walkers, which in our case is constituted by the photon polarizations. In order to show the walk entangling behavior we develop average entanglement quantifiers starting from the entanglement of formation (see Eq. (70)) of the individual states. The platform used to produce the results shown here is the time-multiplexed setup discussed in section 4.3 in combination with the tomographic setup presented in section 4.4.

5.3.1 Generation scheme

In subsection 3.1.3 we discussed how shift and coin operations act on the input state of a single walker to implement a walk of N steps. Here we consider a Hadamard walk, the coin operation is step independent and following from Eq. (13), the walk is realized by the unitary operation:

$$\hat{U}_N = (\hat{S}\hat{C}_H)^N, \tag{137}$$

where $\hat{C}_H$ and $\hat{S}$ are the coin and shift operators defined in Eqs. (11) and (12), respectively.
Now, let us consider a walk with two walkers both starting at the origin of the line with opposite coins, whose state is given by:

$$|\Psi\rangle = |0, \uparrow\rangle_1 \otimes |0, \downarrow\rangle_2. \tag{138}$$

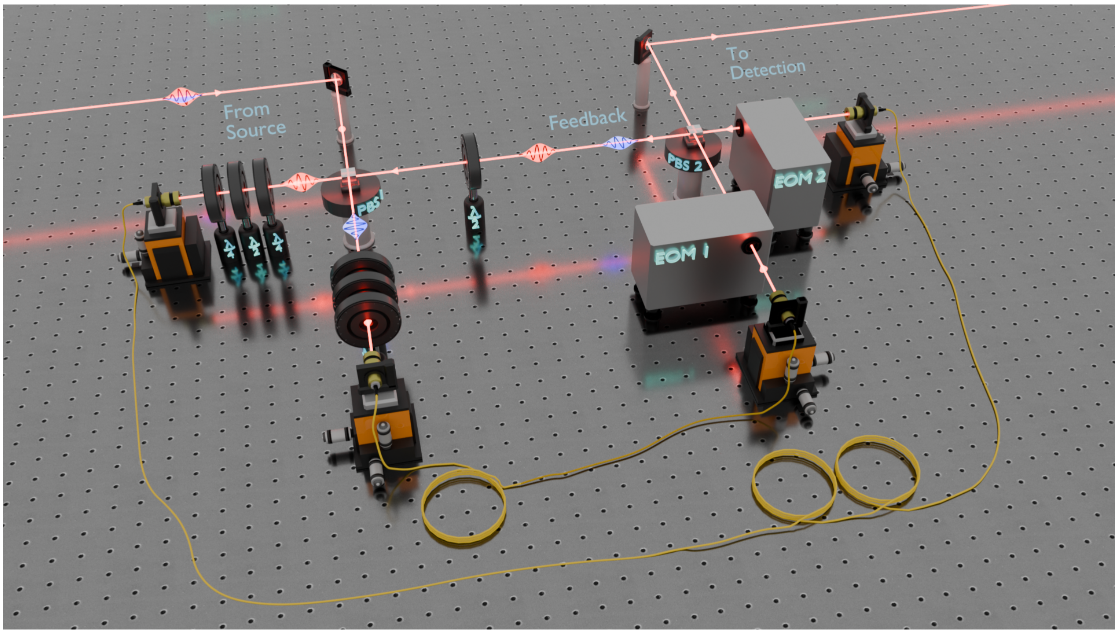

Figure 51: Sketch of the active time-multiplexed setup with static coin. EOM 1 and 2 implement active in- and out-coupling after $|H\rangle$ and $|V\rangle$ polarized photons exit the two fiber delay loops. Instead of using an EOM, here the coin is implemented by an $\frac{\lambda}{2}$-waveplate and it is equal for all time-bins and roundtrips.

After N steps, this state is evolved, according to the operator $\hat{U}_N \otimes \hat{U}_N$ into the state:

$$|\Psi_N\rangle = \sum_{x_1,x_2 \in \Xi_N} \alpha^{(N)}_{x_1,x_2} |x_1, x_2\rangle_p \otimes |\Phi^{(N)}_{x_1,x_2}\rangle_c, \tag{139}$$

where the subscripts p and c denote the two particle joint position and coin subspaces, while Ξ_N is the subset of $\mathbb{Z}$ containing all the line sites occupied at step N. From Eq. (139) we notice that each position pair (x_1, x_2) is associated a coin state $|\Phi^{(N)}_{x_1,x_2}\rangle_c$. Given the coin dimensionality, each of the $|\Phi^{(N)}_{x_1,x_2}\rangle_c$ states can be interpreted as a two-qubit state with an associated density operator $\hat{\rho}_{x_1,x_2}(N) = |\Phi^{(N)}_{x_1,x_2}\rangle_{cc}\langle\Phi^{(N)}_{x_1,x_2}|$. At any step the local coin state associated to a given position combination may be obtained applying the projector $\hat{\Pi}_{x_1,x_2} = |x_1, x_2\rangle_{pp}\langle x_1, x_2|$ to the complete walk state $|\Psi_N\rangle$.
Given the fact that interference within the walk is capable of generating position-coin entanglement [159, 160, 155], we want to investigate if, adopting this projective strategy we can generate entanglement between the two coins.

In practice, to achieve this we use photon pairs generated by our SPDC source to realize the two walkers, whose coin state is given by their polarization. The walk is performed using the setup shown in Fig. 51 where the EOM in the feedback is replaced by a $\frac{\lambda}{2}$-waveplate at 22.5° that implements the Hadamard coin $\hat{C}_H$.
After N roundtrips we direct the photon pair to the tomography setup where a

complete polarization tomography is performed on all possible combinations of output positions. The projection is achieved by post-selecting on events where the two photons have been measured in time-bins encoding the targeted output positions.

5.3.2 Achievable rates

Before proceeding further to illustrate what quantifiers have been used to investigate the entangling dynamics, we must again consider the achievable count rates and measurement times.
Similarly to what we have seen in the previous section, loop efficiencies impact exponentially on the amount of particles reaching the detection stage after each roundtrip. However, although sharing the same basic structure, the setup used here and the one used to study losses in two photon walks features a few key differences which affect the total transmission efficiency. First, since we are interested in output states where both photons exit the setup after the same amount of roundtrips, the waveplates that where implementing the probabilistic outcoupling are not required. Therfore, the probability that a photon is detected after n roundtrips is now given by:

$$p_n = \eta_{ppKTP} \cdot \eta_{in} \cdot \eta_{loop}^{n} \cdot \eta_{fiber} \cdot \eta_{det}. \tag{140}$$

Secondly, in this iteration of the setup $\eta_{in} = 70\%$ and $\eta_{fiber} = 90\%$. Compared to the previous values, the former has been improved building a telescope to increase the mode matching between setup output and detection fibers, while the latter has been increased using an AR coated KTP compensation crystal with a $6 \times 6\ mm^2$ cross-section which inserts no significant losses in the input beam. Please note that this is the crystal with the optimal length discussed at the end of subsection 4.1.4, which means that photons coming from the source are temporally synchronized and feature 98% indistinguishability.

The instantaneous two-photon rate is obtained again using Eq. (134), where now $n = m$. To ensure that a sufficient number of counts is accumulated for all sates generated through the projection $\hat{\Pi}_{x_1,x_2}$ we must consider that, for any step N and position pair (x_1, x_2), the projection succeeds with probability:

$$P_{gen}(N, x_1, x_2) = |\langle \Psi_N | \hat{\Pi}_{x_1,x_2} | \Psi_N \rangle|^2. \tag{141}$$

At each step we are interested in $P_{gen}^{(min)}(N) = min_{x_1,x_2}\{P_{gen}(N, x_1, x_2)\}$. Using this quantity we estimate the amount of two-photon events relative to state with the lowest generation probability as:

$$c_s = P_{gen}^{(min)}(s) \cdot \nu_{rep} \cdot \langle n \rangle \cdot p_s^2. \tag{142}$$

Considering a repetition rate $\nu_{exp} = 15\ kHz$ a mean photon number $\langle n \rangle = 0.01$ and stipulating a minimum value of 100 for c_s we obtain the integration times listed in table 6 for up to 8 steps. These times also take into account the fact that, as discussed when illustrating the tomography setup, the reconstruction requires up to six settings

Step	$P_{gen}^{(min)}$	Integration time [h]
1	50%	0.01
2	25%	0.07
3	9%	0.28
4	2%	1.90
5	2%	2.90
7	1%	13.48
8	0.5%	41.08
Total integration time [h]:	64.14	

Table 6: Estimated measurement times to ensure that running the experiment at 15 kHz with a mean photon number of 0.01, at least 100 coincidences per tomographic setting are recorded for states featuring the lowest generation probability. Recording up to 8 steps requires approximately 64 hours of measurement time.

per step.
Following from this analysis we see that a total measurement time of 64.14 hours is sufficient to ensure the condition $c_s \geq 100$ for $s \leq 8$.
We do not consider more than 8 steps as the integration time for $s = 8$ already exceeds the operation time of the SNSPDs, which need to undergo a cycle of condensation and evaporation each 30 hours in order to maintain them at their operation temperature. This means that measuring step 8 already requires at least two separated measurement runs which might impact negatively on the reconstruction as the experimental conditions might vary.
Recording more than 8 steps would require to lower ν_{rep} and thus integrating even longer, which would lead to additional interruptions for the measurement of a single step.

5.3.3 Walk entangling behavior

The first step required to investigate the walk entangling power is to reconstruct the coin-coin density operators at all steps.
In order to access the density operators at step N we use the tomography setup shown in Fig. 27. As discussed in section 4.4, the reconstruction of a two-qubit density operator requires the evaluation of the expectation values $\langle \hat{\sigma}_i \otimes \hat{\sigma}_j \rangle$ with $x = 0, x, y, z$ and $\hat{\sigma}_0 = \mathbb{I}$. Depending on the combination $\hat{\sigma}_i \otimes \hat{\sigma}_j$ that we want to probe we set the angles of the waveplates in the two tomographic units according to the angles listed in table 1. At this point we record all the time stamps relative to walk positions at step N whose arrival times can be determined using the relation shown in Eq.(132). Given time stamps relative to the chosen position combination (x_1, x_2), we extract from them the number of two photon events N_{H_1,H_2}, N_{H_1,V_2}, N_{V_1,H_2} and N_{V_1,V_2}. These are the coincidences recorded by detection unit pairs (H1,H2), (H1,V2), (V1,H2) and (V1,V2) (see Fig. 27). The desired expectation value is then obtained combining the numbers of

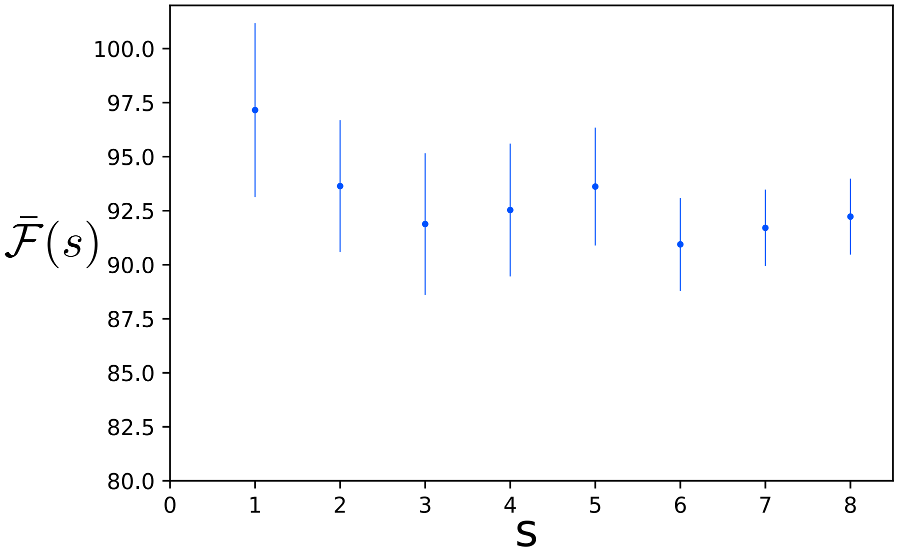

Figure 52: Average quantum state fidelities as function of the step.

two photon events as:

$$\langle \hat{\sigma}_i \otimes \hat{\sigma}_j \rangle = \frac{N_{H_1,H_2} - N_{H_1,V_2} - N_{V_1,H_2} + N_{V_1,V_2}}{N_{H_1,H_2} + N_{H_1,V_2} + N_{V_1,H_2} + N_{V_1,V_2}}. \tag{143}$$

Repeating this procedure for every combination of Pauli basis we can apply Eq. (61) to calculate the coefficients of the expansion of $\hat{\rho}$ in terms of the tensor products $\hat{\sigma}_i \otimes \hat{\sigma}_j$.

The expected states have been simulated according to the Hadamard walk dynamics, which allows to quantify agreement between experiment and theoretical expectations using quantum state fidelity, see Eqs. (125) and (126). In this sense, at each step we can identify a set of fidelities $\mathcal{F}(\hat{\rho}^{theo}_{x_1,x_2}, \hat{\rho}^{exp}_{x_1,x_2})$, for $(x_1, x_2) \in \Xi_s$.
The global agreement over a single step is then given by the average of the quantum fidelities relative to each state, which we call $\bar{\mathcal{F}}(s)$.
In Fig. 52 we show the obtained average fidelities which stay above 90% for all recorded steps and average at $\approx$ 93%.
To each density operator, we can associate a degree of entanglement quantified by its entanglement of formation $\mathcal{E}(\hat{\rho}_{x_1,x_2}(s))$, the first global quantifier that we introduce is the average entanglement, defined as:

$$\bar{\mathcal{E}}(s) = \frac{1}{(s+1)^2} \sum_{x_1,x_2 \,\in\, \Xi_s} \mathcal{E}(\hat{\rho}_{x_1,x_2}(s)), \tag{144}$$

where the normalization factor $(s+1)^2$ corresponds to the number of possible position pairs step s. In Fig. 53a we show the expected trend for $\bar{\mathcal{E}}(s)$ over 100 steps of evolution. Following from the properties of the entanglement of formation, this average quantity not only witnesses the presence of entanglement but also informs about the

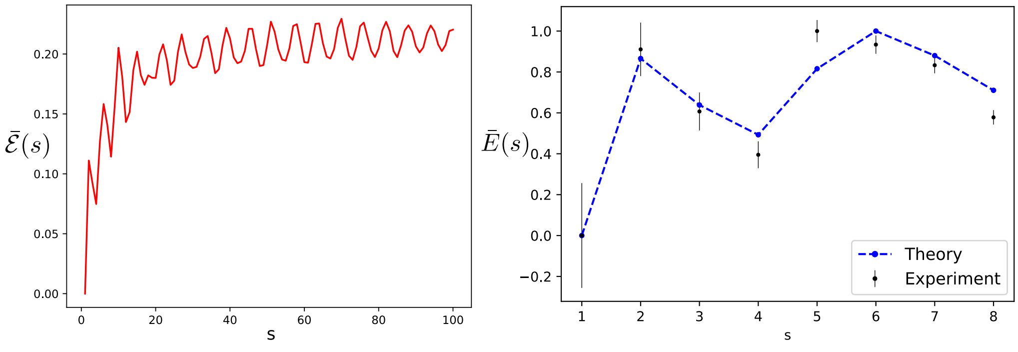

(a) (b)

Figure 53: **(a)** Simulated trend for the mean entanglement for 100 steps. The simulation shows how the walk is expected to generate coin-coin entanglement. **(b):** Experimentally measured normalized mean entanglement. Recording 8 steps of the walk we see how the reconstructed density operators exhibit entanglements. The values are normalized to the maximum entanglement produced over the 8 steps.

average degree of entanglement that we expect to find at each step adopting this generation scheme. As it is seen from the plot $\bar{\mathcal{E}}(s)$ starts at zero as the two walkers are initially in a separable state and increases over the first 20 steps after which its value stops growing and instead tends to oscillate. Therefore, we expect the walk to produce entanglement among the two coin degrees of freedom. Starting from this quantity we can define also a normalized average entanglement as follows:

$$\bar{E}(s) = \frac{\bar{\mathcal{E}}(s)}{\max_s \left\{\bar{\mathcal{E}}(s)\right\}}, \tag{145}$$

where the maximization appearing in the denominator is performed over the number of steps observed.

A non-zero value of $\bar{E}(s)$ still implies that entanglement is generated at step s, however it does not quantify the degree of entanglement in absolute terms but only relatively to the set of steps under investigation. In Fig. 53b we show the experimentally obtained value of $\bar{E}(s)$ compared to the expected ones. We find a good agreement between theory and experiment, therefore we conclude that the time-multiplexed walk is producing entanglement between the photon polarizations.

5.3.4 Spread of entangled photons

Since we now know that the walk produces entanglement, we would like to take a step forward in investigating the behavior of this resource within this system. In particular, we would like to determine how polarization entanglement spreads as the walk progresses. It is known that the spread of a quantum walker, quantified by the standard deviation of its position, depends linearly on the number of steps travelled. This feature makes the quantum walk faster than its classical counterpart, which provides algorithmic advantages in terms of how fast the information carriers move.

We now want to see if a similar behavior can be found when considering the spread of entanglement. In order to do this we define the entanglement distance as the weighted average:

$$\mathcal{D}_{\mathcal{E}}(s) = \sum_{x_1,x_2\,\in\,\Xi_s} \varepsilon_{x_1,x_2}(s)|x_1 - x_2|, \tag{146}$$

where the coefficients $\varepsilon_{x_1,x_2}(s)$ depend on the entanglement of formation of the coin-coin density operators at step s as follows:

$$\varepsilon_{x_1,x_2}(s) = \frac{\mathcal{E}(\hat{\rho}_{x_1,x_2}(s))}{\sum_{x_1,x_2\,\in\,\Xi_s} \mathcal{E}(\hat{\rho}_{x_1,x_2}(s))}. \tag{147}$$

Given this definition for the weights, states featuring higher values of $\mathcal{E}$ contribute more in the sum, while separable states do not contribute at all. Therefore, $\mathcal{D}_{\mathcal{E}}(s)$ gives an information about how far on average are the two walkers when their coin degrees of freedom are in an entangled state.
For comparison, we can consider the average distance between the two walkers:

$$d(s) = \sum_{x_1,x_2\,\in\,\Xi_s} P_s(x_1, x_2)|x_1 - x_2|, \tag{148}$$

where $P_s(x_1, x_2)$ is the probability for the two photons to occupy positions x_1 and x_2 at step s. Fig. 54a shows the simulated trends both for $\mathcal{D}_{\mathcal{E}}(s)$ and $d(s)$ over the first 100 steps of the walk. As expected from the walk dynamics $d(s)$ follows a linear trend as highlighted by the linear fit for which we obtain: $d(s) = 0.61s + 0.53$. In comparison, the fit for the entanglement distance yields a functional dependence $\mathcal{D}_{\mathcal{E}}(s) = 0.37s - 0.31$. Therefore, the average distance among entangled walkers increases linearly with the evolution step, however, when we compared to the two particles spread, entanglement propagates slower than the walkers. The expected trend for the entanglement distance is confirmed experimentally as shown in Fig. 54b, where the experimentally reconstructed values of $\mathcal{D}_{\mathcal{E}}$ are compared with the expected ones for the first eight steps of the walk.

In conclusion, we were able to show experimentally that a quantum walk of two walkers can generate entanglement between the walkers' coins when combined with a measurement induced non-linearity. Moreover, the generated entanglement inherits the walker spreading features, therefore it might be useful in protocols that require Entanglement generation and transport in a quantum network. This concludes this section, in the next one we take a step forward by considering a walk with a non-homogeneous coin operation to show how the time-multiplexed architecture has been employed in order to realize a time-encoded version of a two-qubit gate.

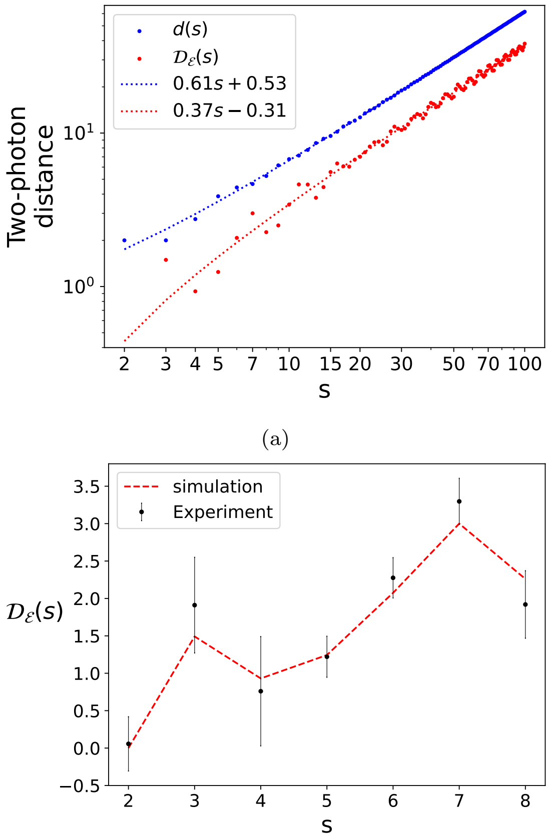

(a)

(b)

Figure 54: **(a):** Simulated trends for $\mathcal{D}_{\mathcal{E}}(s)$ (red dots) and $d(s)$ (blue dots) as a function of the step. Both quantities are expected to follow a linear dependence on s as shown by the linear fits (dotted lines). **(b):** Experimentally measured entanglement distance (black dots) compared to the theoretical expectations.

5.4 Towards time-multiplexed gate based quantum computing

As already discussed in subsection 3.3.2, the circuit model of quantum computing requires gates acting on the state of the quantum register both at a single- and two-qubit level in order to implement the desired computational task. At the same time, this work focusses on photonic encoding, therefore information is carried by one or more degrees of freedom of light quanta.

Depending on the chosen degree of freedom , the realization of single qubit gates within this framework might be challenging form a technical point of view, however no fundamental limitation obstacles the implementation of a unitary operation involving a single photon.

The situation is different when considering two-qubit gates as they require an interaction between the involved particles. For photons this is quite problematic as they are non-interteracting bosons, nevertheless, it is possible to implement two-qubit gates adopting post-selection in an optical interferometer.

A prominent example is the one proposed by Ralph *et. al.* in [161], where a CNOT gate is implemented sending two photons in the path encoded interferoemeter shown in Fig. 55. Where the C_{in} and T_{in} inputs, encode the control and target qubits,

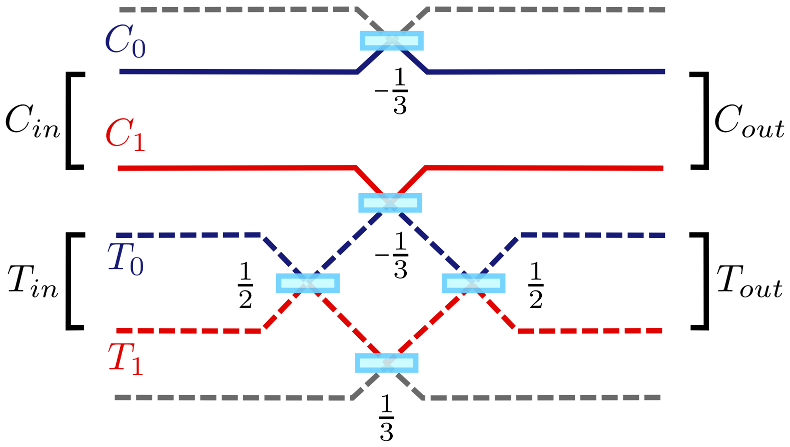

Figure 55: Path encoded interferometer proposed by Ralph *et. al.* in [161] to implement a CNOT gate.

respectively, while the gray inputs and outputs are ancillary modes. In order to produce the evolution of a quantum CNOT gate (see Eq.(37)) a series of beam splitters with different reflectivities acts on the two photons. The reflectivities are shown by the fractions in the scheme, where a reflectivity of $\pm R$ corresponds to the beam splitter operation:

$$\hat{U}_{BS} = \begin{pmatrix} \pm\sqrt{R} & \sqrt{1-R} \\ \sqrt{1-R} & \mp\sqrt{R} \end{pmatrix}. \tag{149}$$

The interferometer consists of two disjointed parts, namely the one constituted by upper ancillary mode and C_0 and the one formed by C_1, T_0, T_1 and the lower ancilla. Notably, the lower part can be seen as a Mach-Zehnder interferometer with lossy arms and a relative π phase between the upper and lower path.

This means that, when the control qubit starts in the $|0\rangle$ state, a single photon enters the lossy Mach-Zehnder either on T_0 or T_1, and given the phase relation between the upper and lower paths it will exit on the same target mode with probability of $\frac{1}{3}$. In all the other cases the photon will be directed to C_1 or to the ancillary mode.

At the same time, the control photon remains in C_0 with probability $\frac{1}{3}$. Therefore, with probability $\frac{1}{9}$, the state of control and target photons will not be altered. When this does not happen, the two photons will always end up in a mode combination that does not preserve the encoding of control and target modes, where, thus in these cases the gate is not successful.

Conversely, when the control is initiated in the $|1\rangle$ state, both photons enter the lower part of the interferometer. Here, partial HOM interference between photons that occupy modes C_1 and T_0 take place at the $-\frac{1}{3}$ beam splitter, which applies an additional π phase shift in all cases where photons emerge on C_1 mode and T_0. Because of the additional phase shift the phase relation in the Mach-Zehnder arms becomes π,

thus a photon that started on T_0 will be sent to T_1 and vice versa.
Therefore, if we only consider events where a single photon exits on the C_1 mode, the state of the target photon will always be flipped, thus, in all successful cases, the interferometer behaves as path encoded CNOT gate. The probability for this to happen is determined by the anti-bunching probability within the partial HOM interference, which is obtained considering that following Eq.(149):

$$\begin{aligned} \hat{c}_1^\dagger &\to \frac{-\hat{c}_1^\dagger + \sqrt{2}\hat{t}_0^\dagger}{\sqrt{3}}, \\ \hat{t}_0^\dagger &\to \frac{\sqrt{2}\hat{c}_1^\dagger + \hat{t}_0^\dagger}{\sqrt{3}}. \end{aligned} \tag{150}$$

Where $\hat{c}_1^\dagger$ and $\hat{t}_0^\dagger$ are the creation operators associated to the modes C_1 and T_0. A photon pair impinging on the beam splitter is represented by the state $c_1^\dagger t_0^\dagger|\varnothing\rangle$, which evolves according to:

$$\hat{c}_1^\dagger\hat{t}_0^\dagger|\varnothing\rangle \to \frac{-\sqrt{2}(\hat{c}_1^\dagger)^2 + \hat{c}_1^\dagger\hat{t}_0^\dagger + \sqrt{2}(\hat{t}_0^\dagger)^2}{3}|\varnothing\rangle, \tag{151}$$

therefore the photons stay separated on the respective control and target modes with probability of $\frac{1}{9}$. Following from the interferometer behavior, we conclude that upon detecting a single photon in the control and target outputs, the circuit implements the CNOT unitary with a success rate of $\frac{1}{9}$.
As we have already pointed out, the scheme shown in Fig. 55 is path encoded, however its implementation may be translated to any other photonic degree of freedom. Photonic CNOT gates have been demonstrated with path and polarization encoding both in bulk [162, 163] and integrated optics [164, 165] At the same time, light properties as frequency [166, 167] and optical angular momentum [168] has been successfully employed to the same scope.
When looking at time-multiplexed, although this strategy has been extensively investigated for scaling systems [169, 75, 170], it has been harnessed to show quantum advantage [17] and some work has been carried out to demonstrate time-multiplexed based linear optical quantum computation [171]. However, a direct implementation of a time encoded CNOT is missing. For this reason now we show how, by introducing a dynamical coin operation in the active time-multiplexed platform, we can use it to implement a circuit capable of preparing the state of control and target qubits and then perform the CNOT gate.

5.4.1 The time-multiplexed CNOT gate

In order to clarify how we use our time-multiplexed system to implement the CNOT, let us start by considering again a path encoded interferometer resembling more closely a quantum walk structure, namely the one shown in Fig. 56.
Comparing this beam splitter cascade that implements an Hadamard walk (Fig. 2b),

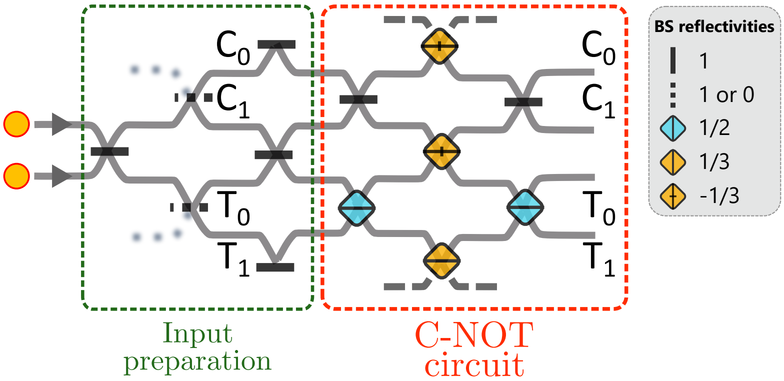

Figure 56: Path encoded circuit implementing both input state preparation and CNOT. The circuit is structured as a quantum walk with a variable coin operation. In the first three steps a series of reflections and transmissions directs the two photons to the desired control and target modes. The remaining three steps implement the CNOT.

we see that both consist of layers of beam splitters whose position may be associated to the sites of a line. Each layer implements a step of the walk, while the beam splitters realize the coin operation, which in this case is not constant.

In particular, we consider a photon pair entering the network at the same input position with opposite coin states, the first step consists of a full reflection that directs the two photons to the next step. Here either transmission or reflection can be applied by the two beam splitters, form here on we can identify the two outputs of the upper beam splitter as the control 0 and 1 modes (C_0 and C_1 in the scheme), while the outputs of the lower one are the target modes (T_0 and T_1). Setting a different combination of reflection and transmissions for the two coins it is possible to generate all four control-target modes, whereby we have:

$$\begin{aligned} C_0\ T_0 &\rightarrow R\ T \\ C_0\ T_1 &\rightarrow T\ T \\ C_1\ T_0 &\rightarrow R\ R \\ C_1\ T_1 &\rightarrow T\ R, \end{aligned} \tag{152}$$

where R and T indicate reflection and transmission, while their order corresponds to the setting for upper and lower beam splitter.

After this selection step, the third one features again only reflections, and it serves the purpose of keeping control and target confined before directing them to the next stage of the interferometer. In this sense, the walk used here significantly differs from the Hadamard walk as it takes place in a constrained position space.

At this point the input state is ready to undergo the CNOT gate, which is implemented by the next three steps of the walk. In fact, we can compare this stage to the scheme shown in Fig. 55. We can see that its upper part is separated from the lower one by the two reflections, therefore this part only couples the C_0 mode to the ancillary one through the beam splitter with $-\frac{1}{3}$ reflectivity. Instead, the lower part is

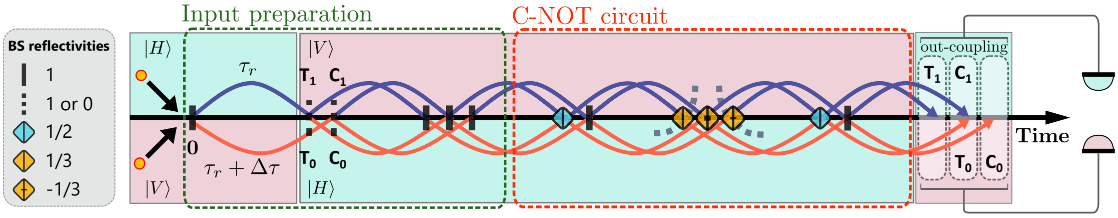

Figure 57: Time encoded version of the circuit shown in Fig. 56. The various optical elements appearing in the path encoded interferometer are translated into a sequence of operations carried out by the same device within the active time-multiplexed setup. The background color shows which polarization travels in the delay loops. The polarization flips happening at roundtrips one and six correspond to the active in- and out-coupling. The gate outcome can be recovered performing time- and polarization-resolved detection.

analogous to the lossy Mach-Zehnder that we have already discussed when explaining Ralph's scheme.

We realize this circuit using a time-multiplexed strategy in the setup discussed in subsection 4.3.3 and shown in Fig. 21, where EOM 3 is used implement a variable coin acting on the photon polarization state.
To this aim, let us consider the timeline shown in Fig. 57, which shows the required sequence of operations. At time $T = 0$ a photon pair coming from the SPDC source arrives at the first PBS of the setup (PBS 1 in Fig. 21). Here they are separated and sent to the short and long fiber delay line, which in the timeline corresponds to traveling forward of τ_r and $\tau_r + \Delta\tau$, respectively. After being in-coupled by EOMs 1 and 2 they are directed to the feedback, where EOM 3 acts on their polarization state to realize the desired input state according to the beam splitter operations listed in Eq. (152). At this point the two photons, which are distributed on two time-bins , come back to PBS 1 where the next roundtrip starts. In the next roundtrips EOM 3 performs the remaining operations shown on the timeline.
Comparing Fig. 56 and Fig. 57 we see that layers of the former correspond to roundtrips within the latter. In order to realize the full circuit in time, six roundtrips within the setup are required. At the end of the sixth roundtrip the two photons are out-coupled and the result of the CNOT is encoded by three output time-bins , where T_1 and C_1 correspond to H-polarized photons, and T_0 and C_0 are V-polarized. A readout of the gate output is obtained performing time- and polarization-resolved detection.

The system efficiencies are the same discussed in the previous section, however, since we perform only six roundtrips the experiment can run at $\nu_{rep} = 21\ kHz$. Setting an input mean photon number of 0.01, and considering the success rate of $\frac{1}{9}$ for the gate, after six roundtrips it is possible to accumulate up to 1000 coincidences distributed over the four time-bins encoding control and target qubits in approximately 1.5 hours. This means that employing these settings for experimental rate and mean photon number, a total of 6 hours of measurement is required to reconstruct the four possible

Platform	Gate fidelity
Bulk optics [172]	84%
Integrated photonics [164]	94%
Frequency encoding [166]	91%
Light orbital angular momentum [168]	65%

Table 7: Reported CNOT gate fidelities for different photonic encodings.

output states of the gate. The result is summarized in the plot shown in Fig. 58 where we show the reconstructed gate operation in comparison with the ideal one, which is the one given by the transformation:

$$\hat{U}_{CNOT} = \begin{pmatrix} 1 & 0 & 0 & 0 \\ 0 & 1 & 0 & 0 \\ 0 & 0 & 0 & 1 \\ 0 & 0 & 1 & 0 \end{pmatrix}.$$

Comparing theory and experiment we obtain a gate fidelity of $(93.8 \pm 1.4)\%$. Comparing the performance of our time-multiplexed scheme to the ones adopted in [172, 164, 166, 168] (see table 7), we find that the gate fidelity of our time-multiplexed CNOT compares favorably to the ones of state-of-the-art platforms exploiting other light degrees of freedom. Given the good performance of the gate, now we show how the system can be reconfigured to implement a circuit shown in Fig. 5, which can generate the four Bell states.

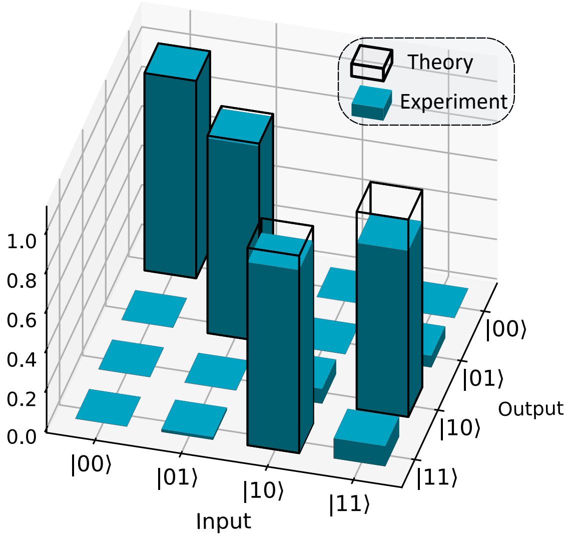

Figure 58: Reconstructed gate operation. Here we show the gate behavior compared to the theoretically expected one. The comparison shows a fidelity of $(93.8 \pm 1.4)\%$.

5.4.2 Generation and detection of Bell states

A CNOT gate can be used to entangle the state of two qubits. In subsection 3.3.5 we have seen how the states of the two-qubit computational basis are transformed into the four Bell states using the circuit shown in Fig.(5). The circuit requires the application of an Hadamard gate on one qubit, which is then fed to a CNOT as control while the other enters as target.
In our framework, an Hadamard gate corresponds to a 50:50 polarization splitting operated by the electro-optical modulator in the setup feedback. To combine Hadamard and CNOT gate, we program the setup to perform the operations shown in Fig. 59. Again, the first three roundtrips in the setup serve as input preparation, while the next block of operations implements the Bell generation circuit. Specifically, at the second time-bin of roundtrip four, the coin EOM is programmed to perform a 50:50 splitting. This has the effect of putting the control qubit into an even superposition of $|0\rangle$ and $|1\rangle$ and implements the Hadamard gate.

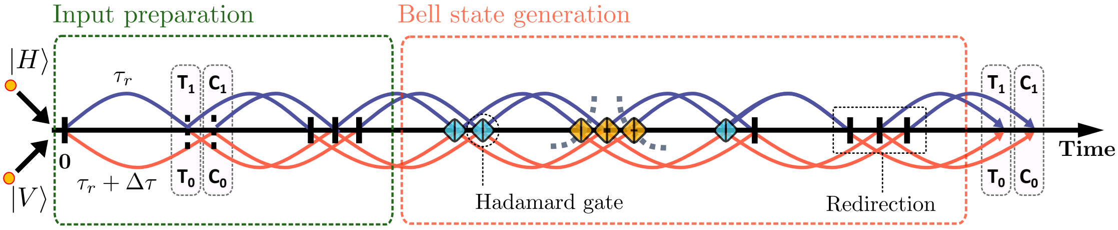

Figure 59: Operation timeline required to generate Bell states.

After this, we perform additional four roundtrips before out-coupling control and target, thus the circuit is one roundtrip longer than the one of Fig. 57. In this additional roundtrip the coin EOM performs again a series of three reflections. This set of additional operations is required to redirect control and target to two separated time-bins). The redirection is required because in order to reconstruct the density operator of the states using the tomography setup, each of the two qubits must be identifiable with a single time-bin.

The state reconstruction is performed in the same way discussed in the previous section, *i.e.* measuring coincidences among the four detection units and combining them to evaluate the correlations $\langle\hat{\sigma}_i \otimes \hat{\sigma}_j\rangle$ for each basis setting.
Because of the additional roundtrip , adopting the same settings in terms of photon generation probabilities and repetition rates, 2 hours of measurement are required for a single input state and tomographic setting. Similarly to what we did to measure the gate operation, we used the state generation stage to prepare the four input states $\{|00\rangle_{CT}, |01\rangle_{CT}, |10\rangle_{CT}, |11\rangle_{CT}\}$ which circuit that we have just discussed. Fig. 60 shows the reconstructed density operators obtained preparing and evolving the four input states $\{|00\rangle_{CT}, |01\rangle_{CT}, |10\rangle_{CT}, |11\rangle_{CT}\}$. Compared to the theoretically expected states, the reconstructed ones exhibit the quantum state fidelities shown in Table 8:
The quantum state fidelities obtained reconstructing the states are comparable with

	$\lvert\phi^-\rangle$	$\lvert\phi^+\rangle$	$\lvert\psi^-\rangle$	$\lvert\psi^+\rangle$
$\mathcal{F}$ [%]	85 ± 6	79 ± 13	76 ± 7	84 ± 12

Table 8: Quantum state fidelities of the reconstructed Bell states

the ones shown in [172], but lower than the ones shown in more recent works [164]. The reduced fidedilities might be ascribed to inbalances in detection efficiency in the four detection arms of the tomography setup. Nonetheless, our system is capable of combining single- and two-qubit gates, wich combined with the inherently scalable nature of time-multiplexing, allows us to envision af a large network based on the parallelization of temporally encoded quantum gates.
Additionally, since our system relies on active optical devices whose action can be adjusted at high speed, our platform is suited to perform feedforward, wich would allow to multiplex several time encoded probabilitstic gates to enhance the success probability.

In conclusion, here we have shown the first implementation of a photonic CNOT gate in fully reconfigurable time-multiplexed . We were able to demonstrate a gate operation with high fidelity, morover, our platform grants us the ability of preparing deterministically different control-target input states, including superpositions at the single qubit level.
Using the system reconfigurability we program it to implement a combination of single- and two-qubit gates capable of generating quantum entanglement.
Additionally, since our system relies on active optical devices whose action can be adjusted at high speed, our platform is particularly suited to perform feedforward.
Hence, our result paves the way to the realization of more complex TM evolution networks featuring a multitude of input and output modes, with no significant limitation in the input states that can be launched in the network.
The architecture presented here can be further improoved both in terms of exprimental rates and accessible transformations.
Albeit featuring low losses, the current free space modulators are limited to bandwidths up to 10 MHz, which limits the time-bin separation to ≈ 100 ns. With the development of faster devices with a bandwidth up to 100 MHz, this parameter as well as the roundtrip time could be reduced by a factor of ten, which in the current setup would have the twofold advantage of enabling higher repetition rates and reducing the length of the fibers from the current 1.1 Km down to 110 m, thus increasing loop efficiencies of $\approx 5\%$.
The unitary transformations accessible by the current platform are limited by the fact that the electro-optical modulator employed to implement the dynamic coin cannot impose an arbitrary phase between H- and V-polarized photons. To this aim, a second electro-optical modulator of the same kind could be used in combination with waveplates as proposed in [173] enabling the time-multiplexed architecture to be used as a universal photonic processor.

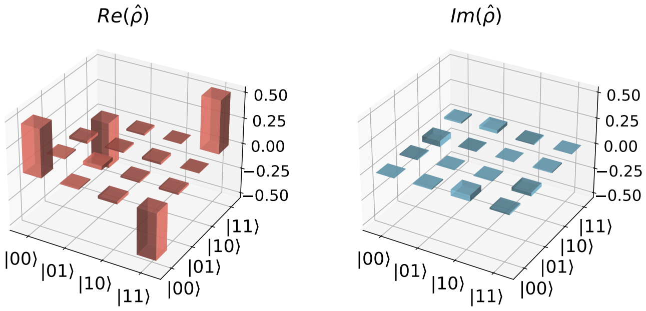

(a) $|\phi^-\rangle$

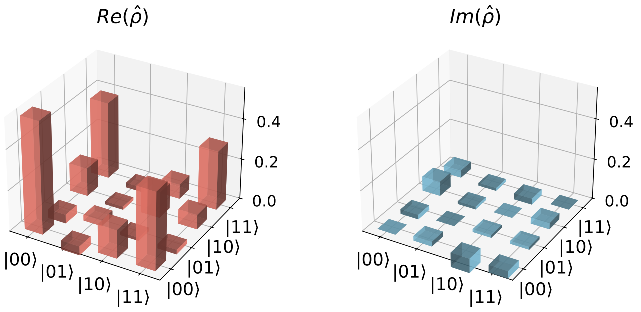

(b) $|\phi^+\rangle$

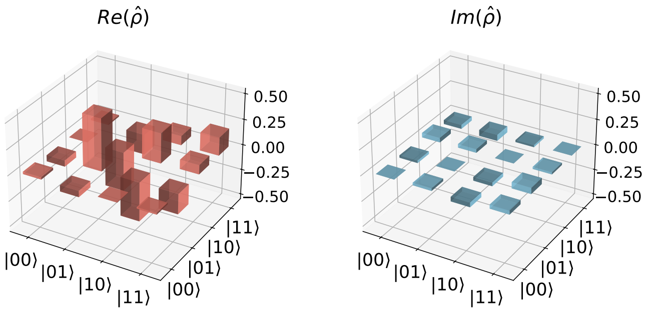

(c) $|\psi^-\rangle$

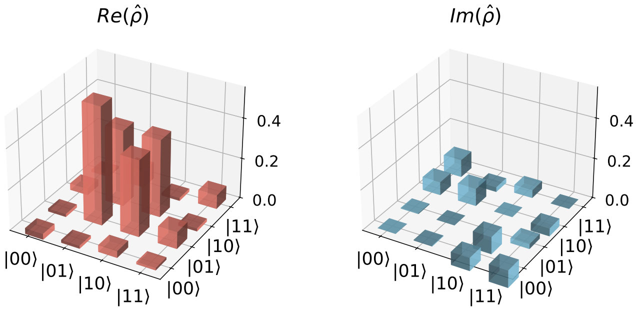

(d) $|\psi^+\rangle$

Figure 60: Real and imaginary part of the reconstructed Bell states.

6 Conclusion and Outlook

The aim of this work was to implement path-encoded and time-multiplexed systems comprising single photon inputs, reconfigurable networks and the ability of both an efficient read-out of the system's output and the reconstruction of the quantum state of selected internal degrees of freedom. At the same time, using these implementations we investigated effects such as open system dynamics, entanglement generation and the introduction of interaction between photonic qubits in a novel time-encoded scheme.

6.1 Path-encoded system

In section 4.2 we presented a path encoded photonic processor featuring the capability of applying any interferometric unitary operation on its twelve input modes. Besides being resource intensive in terms of number of detection units required, this system has shown a few criticalities in terms of mode-dependent quality of single- and two-photon interference (see subsection 5.1.1). We were able to overcome these issues exploiting the platform universal nature, which allows the realization of a unitary routing. Using this method we are able use to physical inputs featuring the best performance to implement any evolution. At the same time, this approach significantly reduces the requirements in terms of peripheral devices and number of detectors needed to perform a complete detection of single- and two-fold events.
We have shown the validity of this method performing Hadamard walks of one and two photons showing similarities with theory up to 99.5% and 90%, respectively.
After demonstrating the good performance of routing, in subsection 5.1.3 we have shown how this idea may be extended in order to generate a state of two qubits and perform a tomography of the associated density operator. Using this approach, we were able to generate Bell states featuring fidelities of up to 97%.
Using this platform and the development machinery in terms of unitary routing we devised a method to study non-unitary dynamics in a quantum walk of two particles (see section 5.2). In this case we have seen how the controlled insertion of losses alters the output distribution of the surviving particle and reveals multi-photon effects. However, the adoption of ancillary modes together with the physical size of the path encoded platform poses a serious limitation to the depth of the evolution. To overcome this issue we performed the same experiment in our time-multiplexed system, where the number of system modes can be efficiently increased tailoring the delay lines within the setup.

6.2 Time-multiplexed system

In section 4.3, we have shown our time-multiplexed setup, which is based on the implementation shown in [124]. One of the main novelties of our implementation is the adoption of electro-optical modulators capable of performing arbitrary operations on the photon polarization and enable the realization of evolutions featuring non-homogeneous coins. In addition, we upgraded the system detection adding the

tomographic units described in section 4.4, thus enabling the reconstruction of the density operators associated to the coin state of a two-photon walk.
Using this system in parallel to the photonic network, we managed to probe the same effects in terms of non-unitary dynamics, but we were also able to access evolutions featuring double the amount of steps because the inherent scalability of the time-multiplexed approach.
In section 5.3 we used the time-multiplexed setup to investigate the entangling power of quantum walks. To do this we used the setup in combination with the new tomography in order to reconstruct the joint coin states of two-walkers performing up to 8 steps of an Hadamard walk. Adopting average entanglement quantifiers we have shown how, starting from separable two-photon state the walk generates entanglement between the polarization of the two particles. Moreover, considering the average distance of entangled photons, we have shown that this quantity follows a non-decreasing behavior. Thus, the walk distributes the generated entanglement to system nodes positioned further apart in the network as it progresses.
In section 5.4 we demonstrated how the time-multiplexed setup equipped with the new electro-optical modulator can be programmed to implement a quantum circuit and we used it to demonstrate the first direct implementation of a time-multiplexed CNOT gate showing a system performance comparable or higher than the ones of implementations exploiting different photonic encodings [172, 164, 166, 168]
Using the same platform with a modified operation sequence we were able to realize a circuit containing single- and two-qubit gates capable of generating Bell states starting from the two-qubit computational basis. This constitutes a step towards time-multiplexed gate based quantum computing and shows how the time-multiplexed setup can be employed in a way similar to the path encoded chip. However, additional work has to be done in order to match the chip capabilities in terms of accessible unitaries. In fact, the unit cell of the time-multiplexed circuit presented in subsection 5.4.1 can realize any splitting ratio of $|H\rangle$ and $|V\rangle$, it is not capable of imposing an arbitrary relative phase among the two polarizations. Therefore, a step must still be taken in this direction in order to convert the system used in this work into a fully fledged universal time-multiplexed photonic processor.

In summary, we have implemented two highly reconfigurable systems exploiting different encodings where pure and indistinguishable photons can be deployed in order to perform complex single- and two-particle unitary evolutions where we have the ability of resolving all system modes as well as performing a complete quantum state tomography of a set of selected degrees of freedom.

7 Acknowledgements

During the time I have spent in Paderborn for my PhD, I had the great opportunity of joining a fervent group of scientists working enthusiastically in a quickly developing research field. I found myself in a stimulating and supporting environment, where I have had the chance of developing as a researcher. This thesis would have not been possible without a lot of discussions, shared ideas and moment of support which came from many people, who I would like to acknowledge and thank here.

First, I would like to express my deepest gratitude to Christine for offering me the opportunity of working in her group. I would also like to thank her for being an excellent supervisor, for being always able to provide guidance and for encouraging me to explore new ideas. Working with her, I learnt one of the most important lessons: never be afraid of asking "stupid questions"; which I think is not only true in science but a good approach in life in general.

A special thank goes also to my group leader Benni, who has been a reference in all kind of matters and has been always present throughout these years to provide advice and guidance.

In addition, I would like to thank Syam and Sonja for letting me work closely with them at the very beginning and for introducing me to the arts of time-multiplexing.

This journey would have not been the same without those who were there when I started and made moving to a new country during a pandemic much more enjoyable and, more importantly, less lonely. I would like to thank Laura, Franz, Patrick and Dana, my fellow "newbies", for being a wonderful group of companions. I will never forget how much fun we had together, and I will always smile when thinking to our adventures. Talking about how it all started, I owe a special thanks to Matteo who welcomed me in Paderborn on what I will always remember as the snowiest day of my life and also as the first time I have ever had to deal with the German railways.

I am also grateful to Abhinandan, who has been my running mate and with whom I have quite literally shared a lot of kilometers of this journey.

Office and lab life would have not been as bright without many people. A big thanks goes to Philip for being both an excellent colleague and co-lab-responsible, and also to always make sure that I was familiar with important aspects of the German culture such as Schläger songs and comedy sketches by Loriot. Jokes aside, it has been a pleasure to share a considerable amount of lab time with him and I hope we both benefitted from collaborating on many projects. I would also like to thank Jonas for being an excellent fellow quantum walker, for inspiring me with his deep thinking and for the time spent filling whiteboards of calculations only to find out that, sometimes, SU(2) is not the answer.

Apart from my personal experience and development, I also consider myself lucky to have witnessed the first steps of a new generation of scientists. In particular, I would like to thank Moritz and Theresa for the motivation they have shown from the very beginning and for the fun moments shared in the lab, in the office and at conferences.

Last, but not least, I would like to express my gratitude to people who have not been in Paderborn the whole time, but nonetheless have been with me in a way or the other:

a heartfelt thank goes to my family and to my old university colleague and friend Luca for supporting me during this journey and always believing in me.

8 References

[1] Richard P. Feynman. “Simulating physics with computers”. In: *International Journal of Theoretical Physics* 21.6–7 (June 1982), pp. 467–488. ISSN: 0020-7748, 1572-9575. DOI: `10.1007/BF02650179`. URL: `http://link.springer.com/10.1007/BF02650179`.

[2] Charles H Bennett and Gilles Brassard. “Quantum cryptography: Public key distribution and coin tossing”. In: *Theoretical computer science* 560 (2014), pp. 7–11.

[3] Artur K Ekert. “Quantum cryptography based on Bell’s theorem”. In: *Physical review letters* 67.6 (1991), p. 661.

[4] Peter W. Shor. “Polynomial-Time Algorithms for Prime Factorization and Discrete Logarithms on a Quantum Computer”. In: *SIAM Journal on Computing* 26.5 (Oct. 1997), pp. 1484–1509. ISSN: 0097-5397. DOI: `10.1137/S0097539795293172`. URL: `http://epubs.siam.org/doi/abs/10.1137/S0097539795293172`.

[5] Lov K. Grover. “A fast quantum mechanical algorithm for database search”. In: *arXiv preprint quant-ph/9605043* (May 1996). URL: `http://arxiv.org/abs/quant-ph/9605043`.

[6] Stephen Wiesner. “Conjugate coding”. In: *ACM Sigact News* 15.1 (1983), pp. 78–88.

[7] Carlton M Caves. “Quantum-mechanical noise in an interferometer”. In: *Physical Review D* 23.8 (1981), p. 1693.

[8] Vittorio Giovannetti, Seth Lloyd, and Lorenzo Maccone. “Quantum metrology”. In: *Physical review letters* 96.1 (2006), p. 010401.

[9] John Preskill. “Quantum computing and the entanglement frontier”. In: *arXiv preprint arXiv:1203.5813* (2012).

[10] Sergio Boixo et al. “Characterizing quantum supremacy in near-term devices”. In: *Nature Physics* 14.6 (2018), pp. 595–600.

[11] Scott Aaronson and Alex Arkhipov. “The Computational Complexity of Linear Optics”. In: *Proceedings of the 43rd Annual ACM Symposium on Theory of Computing (STOC ’11)*. New York, NY, USA: ACM, 2011, pp. 333–342. ISBN: 978-1-4503-0691-1. DOI: `10.1145/1993636.1993682`. URL: `http://doi.acm.org/10.1145/1993636.1993682`.

[12] Craig S. Hamilton et al. “Gaussian Boson Sampling”. In: *Physical Review Letters* 119.17 (Oct. 2017), p. 170501. DOI: `10.1103/PhysRevLett.119.170501`. URL: `https://link.aps.org/doi/10.1103/PhysRevLett.119.170501`.

[13] Frank Arute et al. “Quantum supremacy using a programmable superconducting processor”. In: *Nature* 574.7779 (2019), pp. 505–510.

[14] Yulin Wu et al. “Strong quantum computational advantage using a superconducting quantum processor”. In: *Physical review letters* 127.18 (2021), p. 180501.

[15] Han-Sen Zhong et al. “Quantum computational advantage using photons”. In: *Science* (2020).

[16] Han-Sen Zhong et al. “Phase-programmable Gaussian boson sampling using stimulated squeezed light”. In: *Physical review letters* 127.18 (2021), p. 180502.

[17] Lars S Madsen et al. “Quantum computational advantage with a programmable photonic processor”. In: *Nature* 606.7912 (2022), pp. 75–81.

[18] John Clarke and Frank K Wilhelm. “Superconducting quantum bits”. In: *Nature* 453.7198 (2008), pp. 1031–1042.

[19] Colin D Bruzewicz et al. “Trapped-ion quantum computing: Progress and challenges”. In: *Applied physics reviews* 6.2 (2019).

[20] Pieter Kok et al. “Linear optical quantum computing with photonic qubits”. In: *Reviews of modern physics* 79.1 (2007), pp. 135–174.

[21] Loic Henriet et al. “Quantum computing with neutral atoms”. In: *Quantum* 4 (2020), p. 327.

[22] Igor Žutić, Jaroslav Fabian, and S Das Sarma. “Spintronics: Fundamentals and applications”. In: *Reviews of modern physics* 76.2 (2004), p. 323.

[23] Daniel Loss and David P DiVincenzo. “Quantum computation with quantum dots”. In: *Physical Review A* 57.1 (1998), p. 120.

[24] Karl Pearson. “The problem of the random walk”. In: *Nature* 72.1867 (1905), pp. 342–342.

[25] George H Weiss and Robert J Rubin. “Random walks: theory and selected applications”. In: *Adv. Chem. Phys* 52 (1983), pp. 363–505.

[26] David A Kodde and Hein Schreuder. “Forecasting Corporate Revenue and Profit: Time-Series Models versus Management and Analysts”. In: *Journal of Business Finance & Accounting* 11.3 (1984), pp. 381–395.

[27] Thomas F Hansen and Emília P Martins. “Translating between microevolutionary process and macroevolutionary patterns: the correlation structure of interspecific data”. In: *Evolution* 50.4 (1996), pp. 1404–1417.

[28] Ziv Bar-Yossef and Maxim Gurevich. “Random sampling from a search engine’s index”. In: *J. ACM* 55.5 (Nov. 2008). ISSN: 0004-5411. DOI: `10.1145/1411509.1411514`. URL: `https://doi.org/10.1145/1411509.1411514`.

[29] Francis Galton. *Natural inheritance*. Macmillan, 1889.

[30] Frederick W Strauch. “Connecting the discrete-and continuous-time quantum walks”. In: *Physical Review A—Atomic, Molecular, and Optical Physics* 74.3 (2006), p. 030301.

[31] Andrew M Childs. “On the relationship between continuous-and discrete-time quantum walk”. In: *Communications in Mathematical Physics* 294 (2010), pp. 581–603.

[32] Salvador Venegas-Andraca. “Quantum walks: a comprehensive review”. In: *Quantum Information Processing* 11.5 (2012), pp. 1015–1106.

[33] Andrew M. Childs. “Universal Computation by Quantum Walk”. In: *Physical Review Letters* 102.18 (May 2009), p. 180501. DOI: `10.1103/PhysRevLett.102.180501`. URL: `https://link.aps.org/doi/10.1103/PhysRevLett.102.180501`.

[34] Andrew M. Childs, David Gosset, and Zak Webb. “Universal Computation by Multiparticle Quantum Walk”. In: *Science* 339.6121 (Feb. 2013), pp. 791–794. ISSN: 0036-8075, 1095-9203. DOI: `10.1126/science.1229957`. URL: `http://science.sciencemag.org/content/339/6121/791`.

[35] Neil B. Lovett et al. “Universal quantum computation using the discrete-time quantum walk”. In: *Physical Review A* 81.4 (Apr. 2010), p. 042330. DOI: `10.1103/PhysRevA.81.042330`. URL: `https://link.aps.org/doi/10.1103/PhysRevA.81.042330`.

[36] Neil Shenvi, Julia Kempe, and K. Birgitta Whaley. “Quantum random-walk search algorithm”. In: *Physical Review A* 67.5 (May 2003), p. 052307. DOI: `10.1103/PhysRevA.67.052307`. URL: `https://link.aps.org/doi/10.1103/PhysRevA.67.052307`.

[37] Andris Ambainis. “Quantum Walk Algorithm for Element Distinctness”. In: *SIAM Journal on Computing* 37.1 (Jan. 2007), pp. 210–239. DOI: `10.1137/S0097539705447311`. URL: `http://epubs.siam.org/doi/10.1137/S0097539705447311`.

[38] Frederick W. Strauch. “Relativistic quantum walks”. In: *Physical Review A* 73.5 (May 2006), p. 054302. DOI: `10.1103/PhysRevA.73.054302`. URL: `https://link.aps.org/doi/10.1103/PhysRevA.73.054302`.

[39] Gregory S. Engel et al. “Evidence for wavelike energy transfer through quantum coherence in photosynthetic systems”. In: *Nature* 446.7137 (Apr. 2007), pp. 782–786. DOI: `10.1038/nature05678`. URL: `https://www.nature.com/articles/nature05678`.

[40] C. K. Law, I. A. Walmsley, and J. H. Eberly. “Continuous Frequency Entanglement: Effective Finite Hilbert Space and Entropy Control”. In: *Physical Review Letters* 84.23 (June 2000), pp. 5304–5307. DOI: `10.1103/PhysRevLett.84.5304`. URL: `https://link.aps.org/doi/10.1103/PhysRevLett.84.5304`.

[41] M. B. Plenio and S. F. Huelga. “Dephasing-assisted transport: quantum networks and biomolecules”. In: *New Journal of Physics* 10.11 (2008), p. 113019. DOI: `10.1088/1367-2630/10/11/113019`. URL: `http://stacks.iop.org/1367-2630/10/i=11/a=113019`.

[42] Andre Ahlbrecht et al. "Molecular binding in interacting quantum walks". In: *New Journal of Physics* 14.7 (2012), p. 073050. DOI: `10.1088/1367-2630/14/7/073050`. URL: `http://stacks.iop.org/1367-2630/14/i=7/a=073050`.

[43] D. Witthaut. "Quantum walks and quantum simulations with Bloch-oscillating spinor atoms". In: *Physical Review A* 82.3 (Sept. 2010), p. 033602. DOI: `10.1103/PhysRevA.82.033602`. URL: `https://link.aps.org/doi/10.1103/PhysRevA.82.033602`.

[44] Chang-Woo Lee, Pawel Kurzynski, and Hyunchul Nha. "Quantum walk as a simulator of nonlinear dynamics: Nonlinear Dirac equation and solitons". In: *Physical Review A* 92.5 (Nov. 2015), p. 052336. DOI: `10.1103/PhysRevA.92.052336`. URL: `https://link.aps.org/doi/10.1103/PhysRevA.92.052336`.

[45] Takuya Kitagawa et al. "Exploring topological phases with quantum walks". In: *Physical Review A* 82.3 (Sept. 2010), p. 033429. DOI: `10.1103/PhysRevA.82.033429`. URL: `https://link.aps.org/doi/10.1103/PhysRevA.82.033429`.

[46] J. K. Asbóth. "Symmetries, topological phases, and bound states in the one-dimensional quantum walk". In: *Physical Review B* 86.19 (Nov. 2012), p. 195414. DOI: `10.1103/PhysRevB.86.195414`. URL: `https://link.aps.org/doi/10.1103/PhysRevB.86.195414`.

[47] C. Cedzich et al. "The Topological Classification of One-Dimensional Symmetric Quantum Walks". In: *Annales Henri Poincaré* 19.2 (Feb. 2018), pp. 325–383. DOI: `10.1007/s00023-017-0630-x`. URL: `https://link.springer.com/article/10.1007/s00023-017-0630-x`.

[48] Matthew A. Broome et al. "Photonic Boson Sampling in a Tunable Circuit". In: *Science* 339.6121 (Feb. 2013), pp. 794–798. DOI: `10.1126/science.1231440`. URL: `http://science.sciencemag.org/content/339/6121/794`.

[49] Justin B. Spring et al. "Boson Sampling on a Photonic Chip". In: *Science* 339.6121 (Feb. 2013), pp. 798–801. DOI: `10.1126/science.1231692`. URL: `http://science.sciencemag.org/content/339/6121/798`.

[50] Keith R. Motes et al. "Scalable Boson Sampling with Time-Bin Encoding Using a Loop-Based Architecture". In: *Physical Review Letters* 113.12 (Sept. 2014), p. 120501. DOI: `10.1103/PhysRevLett.113.120501`. URL: `https://link.aps.org/doi/10.1103/PhysRevLett.113.120501`.

[51] Yu He et al. "Time-Bin–Encoded Boson Sampling with a Single-Photon Device". In: *Physical Review Letters* 118.19 (May 2017), p. 190501. DOI: `10.1103/PhysRevLett.118.190501`. URL: `https://link.aps.org/doi/10.1103/PhysRevLett.118.190501`.

[52] Hui Wang et al. "High-efficiency multiphoton boson sampling". In: *Nature Photonics* 11.6 (June 2017), pp. 361–365. DOI: `10.1038/nphoton.2017.63`. URL: `http://www.nature.com/nphoton/journal/v11/n6/full/nphoton.2017.63.html`.

[53] Hagai Perets et al. "Realization of Quantum Walks with Negligible Decoherence in Waveguide Lattices". In: *Physical Review Letters* 100.17 (May 2008), p. 170506. DOI: `10.1103/PhysRevLett.100.170506`. URL: `http://link.aps.org/doi/10.1103/PhysRevLett.100.170506`.

[54] Alberto Peruzzo et al. "Quantum Walks of Correlated Photons". In: *Science* 329.5998 (Sept. 2010), pp. 1500–1503. DOI: `10.1126/science.1193515`. URL: `http://science.sciencemag.org/content/329/5998/1500`.

[55] Regina Kruse et al. "Spatio-spectral characteristics of parametric down-conversion in waveguide arrays". In: *New Journal of Physics* 15.8 (2013), p. 083046. DOI: `10.1088/1367-2630/15/8/083046`. URL: `http://stacks.iop.org/1367-2630/15/i=8/a=083046`.

[56] J. D. A. Meinecke et al. "Coherent time evolution and boundary conditions of two-photon quantum walks in waveguide arrays". In: *Physical Review A* 88.1 (July 2013), p. 012308. DOI: `10.1103/PhysRevA.88.012308`. URL: `http://link.aps.org/doi/10.1103/PhysRevA.88.012308`.

[57] H. Schmitz et al. "Quantum Walk of a Trapped Ion in Phase Space". In: *Physical Review Letters* 103.9 (Aug. 2009), p. 090504. DOI: `10.1103/PhysRevLett.103.090504`. URL: `https://link.aps.org/doi/10.1103/PhysRevLett.103.090504`.

[58] F. Zähringer et al. "Realization of a Quantum Walk with One and Two Trapped Ions". In: *Physical Review Letters* 104.10 (Mar. 2010), p. 100503. DOI: `10.1103/PhysRevLett.104.100503`. URL: `https://link.aps.org/doi/10.1103/PhysRevLett.104.100503`.

[59] Michal Karski et al. "Quantum Walk in Position Space with Single Optically Trapped Atoms". In: *Science* 325.5937 (July 2009), pp. 174–177. DOI: `10.1126/science.1174436`. URL: `http://science.sciencemag.org/content/325/5937/174`.

[60] Maximilian Genske et al. "Electric Quantum Walks with Individual Atoms". In: *Physical Review Letters* 110.19 (May 2013), p. 190601. DOI: `10.1103/PhysRevLett.110.190601`. URL: `https://link.aps.org/doi/10.1103/PhysRevLett.110.190601`.

[61] C. A. Ryan et al. "Experimental implementation of a discrete-time quantum random walk on an NMR quantum-information processor". In: *Physical Review A* 72.6 (Dec. 2005), p. 062317. DOI: `10.1103/PhysRevA.72.062317`. URL: `https://link.aps.org/doi/10.1103/PhysRevA.72.062317`.

[62] Matthew A. Broome et al. “Discrete Single-Photon Quantum Walks with Tunable Decoherence”. In: *Physical Review Letters* 104.15 (Apr. 2010), p. 153602. DOI: `10.1103/PhysRevLett.104.153602`. URL: `http://link.aps.org/doi/10.1103/PhysRevLett.104.153602`.

[63] Peng Xue et al. “Observation of quasiperiodic dynamics in a one-dimensional quantum walk of single photons in space”. In: *New Journal of Physics* 16.5 (2014), p. 053009. DOI: `10.1088/1367-2630/16/5/053009`. URL: `http://stacks.iop.org/1367-2630/16/i=5/a=053009`.

[64] Peng Xue et al. “Localized state in a two-dimensional quantum walk on a disordered lattice”. In: *Physical Review A* 92.4 (Oct. 2015), p. 042316. DOI: `10.1103/PhysRevA.92.042316`. URL: `https://link.aps.org/doi/10.1103/PhysRevA.92.042316`.

[65] Andrea Geraldi et al. “A novel bulk-optics scheme for quantum walk with high phase stability”. In: *Condensed Matter* 4.1 (2019), p. 14.

[66] J. O. Owens et al. “Two-photon quantum walks in an elliptical direct-write waveguide array”. In: *New Journal of Physics* 13.7 (July 2011), p. 075003. DOI: `10.1088/1367-2630/13/7/075003`. URL: `http://iopscience.iop.org/1367-2630/13/7/075003`.

[67] Linda Sansoni et al. “Two-Particle Bosonic-Fermionic Quantum Walk via Integrated Photonics”. In: *Physical Review Letters* 108.1 (Jan. 2012), p. 010502. DOI: `10.1103/PhysRevLett.108.010502`. URL: `http://link.aps.org/doi/10.1103/PhysRevLett.108.010502`.

[68] Andrea Crespi et al. “Anderson localization of entangled photons in an integrated quantum walk”. In: *Nature Photonics* 7.4 (Apr. 2013), pp. 322–328. DOI: `10.1038/nphoton.2013.26`. URL: `http://www.nature.com/nphoton/journal/v7/n4/abs/nphoton.2013.26.html`.

[69] Jacques Carolan et al. “Universal Linear Optics”. In: *Science* 349.6249 (Aug. 2015), pp. 711–716. DOI: `10.1126/science.aab3642`. URL: `http://arxiv.org/abs/1505.01182`.

[70] Syamsundar De et al. “Realization of high-fidelity unitary operations on up to 64 frequency bins”. In: *Physical Review Research* 6.2 (2024), p. L022040.

[71] Pei Zhang et al. “Demonstration of one-dimensional quantum random walks using orbital angular momentum of photons”. In: *Physical Review A* 75.5 (May 2007), p. 052310. DOI: `10.1103/PhysRevA.75.052310`. URL: `https://link.aps.org/doi/10.1103/PhysRevA.75.052310`.

[72] Sandeep K. Goyal et al. “Implementing Quantum Walks Using Orbital Angular Momentum of Classical Light”. In: *Physical Review Letters* 110.26 (June 2013), p. 263602. DOI: `10.1103/PhysRevLett.110.263602`. URL: `https://link.aps.org/doi/10.1103/PhysRevLett.110.263602`.

[73] Filippo Cardano et al. “Quantum walks and wavepacket dynamics on a lattice with twisted photons”. In: *Science Advances* 1.2 (Mar. 2015), e1500087. DOI: `10.1126/sciadv.1500087`. URL: `http://advances.sciencemag.org/content/1/2/e1500087`.

[74] Bereneice Sephton et al. “A versatile quantum walk resonator with bright classical light”. In: *PLOS ONE* 14.4 (Apr. 2019), e0214891. DOI: `10.1371/journal.pone.0214891`. URL: `http://dx.plos.org/10.1371/journal.pone.0214891`.

[75] A. Schreiber et al. “Photons Walking the Line: A Quantum Walk with Adjustable Coin Operations”. In: *Physical Review Letters* 104.5 (Feb. 2010), p. 050502. DOI: `10.1103/PhysRevLett.104.050502`. URL: `http://link.aps.org/doi/10.1103/PhysRevLett.104.050502`.

[76] Alois Regensburger et al. “Photon Propagation in a Discrete Fiber Network: An Interplay of Coherence and Losses”. In: *Physical Review Letters* 107.23 (Dec. 2011), p. 233902. DOI: `10.1103/PhysRevLett.107.233902`. URL: `http://link.aps.org/doi/10.1103/PhysRevLett.107.233902`.

[77] Julien Boutari et al. “Large-scale quantum walks by means of optical fiber cavities”. In: *Journal of Optics* 18.9 (2016), p. 094007. DOI: `10.1088/2040-8978/18/9/094007`. URL: `http://stacks.iop.org/2040-8986/18/i=9/a=094007`.

[78] Kia Manouchehri and Jingbo Wang. *Physical Implementation of Quantum Walks*. Berlin, Heidelberg: Springer Berlin Heidelberg, 2014. ISBN: 978-3-642-36014-5. DOI: `10.1007/978-3-642-36014-5`. URL: `http://link.springer.com/10.1007/978-3-642-36014-5`.

[79] John Preskill. “Quantum computing in the NISQ era and beyond”. In: *Quantum* 2 (2018), p. 79.

[80] Lieven M. K. Vandersypen and Mark A. Eriksson. “Quantum computing with semiconductor spins”. In: *Physics Today* 72.8 (Aug. 2019), pp. 38–45.

[81] J. A. Jones and M. Mosca. “Implementation of a quantum algorithm on a nuclear magnetic resonance quantum computer”. In: *The Journal of Chemical Physics* 109.5 (Aug. 1998), pp. 1648–1653.

[82] J. I. Cirac and P. Zoller. “Quantum Computations with Cold Trapped Ions”. In: *Phys. Rev. Lett.* 74 (20 May 1995), pp. 4091–4094.

[83] Adriano Barenco et al. “Conditional Quantum Dynamics and Logic Gates”. In: *Phys. Rev. Lett.* 74 (20 May 1995), pp. 4083–4086.

[84] Eduardo Berrios et al. “High fidelity quantum gates with vibrational qubits”. In: *The Journal of Physical Chemistry A* 116.46 (2012), pp. 11347–11354.

[85] He-Liang Huang et al. “Superconducting quantum computing: a review”. In: *Science China Information Sciences* 63.8 (July 2020).

[86] A.Yu. Kitaev. “Fault-tolerant quantum computation by anyons”. In: *Annals of Physics* 303.1 (Jan. 2003), pp. 2–30.

[87] Emanuel Knill, Raymond Laflamme, and Gerald J Milburn. “A scheme for efficient quantum computation with linear optics”. In: *nature* 409.6816 (2001), p. 46.

[88] T. B. Pittman, B. C. Jacobs, and J. D. Franson. “Probabilistic quantum logic operations using polarizing beam splitters”. In: *Phys. Rev. A* 64 (6 Nov. 2001), p. 062311.

[89] William R Clements et al. “Optimal design for universal multiport interferometers”. In: *Optica* 3.12 (2016), pp. 1460–1465.

[90] Michael Reck et al. “Experimental realization of any discrete unitary operator”. In: *Phys. Rev. Lett.* 73 (1 July 1994), pp. 58–61.

[91] Peter P. Rohde. “Simple scheme for universal linear-optics quantum computing with constant experimental complexity using fiber loops”. In: *Phys. Rev. A* 91 (1 Jan. 2015), p. 012306. DOI: `10.1103/PhysRevA.91.012306`. URL: `https://link.aps.org/doi/10.1103/PhysRevA.91.012306`.

[92] P. W. Anderson. “Absence of Diffusion in Certain Random Lattices”. In: *Physical Review* 109.5 (Mar. 1958), pp. 1492–1505. DOI: `10.1103/PhysRev.109.1492`. URL: `https://link.aps.org/doi/10.1103/PhysRev.109.1492`.

[93] A. Schreiber et al. “Decoherence and Disorder in Quantum Walks: From Ballistic Spread to Localization”. In: *Physical Review Letters* 106.18 (May 2011), p. 180403. DOI: `10.1103/PhysRevLett.106.180403`. URL: `http://link.aps.org/doi/10.1103/PhysRevLett.106.180403`.

[94] Fabian Elster et al. “Quantum walk coherences on a dynamical percolation graph”. In: *Scientific Reports* 5 (Aug. 2015), p. 13495. ISSN: 2045-2322. DOI: `10.1038/srep13495`. URL: `http://www.nature.com/doifinder/10.1038/srep13495`.

[95] Thomas Nitsche et al. “Quantum walks with dynamical control: graph engineering, initial state preparation and state transfer”. In: *New Journal of Physics* 18.6 (2016), p. 063017. DOI: `10.1088/1367-2630/18/6/063017`. URL: `http://stacks.iop.org/1367-2630/18/i=6/a=063017`.

[96] Shota Yokoyama et al. “Ultra-large-scale continuous-variable cluster states multiplexed in the time domain”. In: *Nature Photonics* 7.12 (2013), pp. 982–986.

[97] Warit Asavanant et al. “Generation of time-domain-multiplexed two-dimensional cluster state”. In: *Science* 366.6463 (2019), pp. 373–376.

[98] H Aghaee Rad et al. “Scaling and networking a modular photonic quantum computer”. In: *Nature* 638.8052 (2025), pp. 912–919.

[99] Hua-Liang Liu et al. “Robust quantum computational advantage with programmable 3050-photon Gaussian boson sampling”. In: *arXiv preprint arXiv:2508.09092* (2025).

[100] Han-Sen Zhong et al. “Experimental gaussian boson sampling”. In: *Science Bulletin* 64.8 (2019), pp. 511–515.

[101] Marco Bentivegna et al. “Experimental scattershot boson sampling”. In: *Science advances* 1.3 (2015), e1400255.

[102] Han-Sen Zhong et al. “12-photon entanglement and scalable scattershot boson sampling with optimal entangled-photon pairs from parametric down-conversion”. In: *Physical Review Letters* 121.25 (2018), p. 250505.

[103] Giuliano Benenti, Giulio Casati, and Giuliano Strini. *Principles of quantum computation and information-volume I: Basic concepts*. World scientific, 2004.

[104] Adriano Barenco et al. “Elementary gates for quantum computation”. In: *Physical review A* 52.5 (1995), p. 3457.

[105] Michael A Nielsen and Isaac L Chuang. *Quantum computation and quantum information*. Vol. 2. Cambridge university press Cambridge, 2001.

[106] Colin P Williams and Colin P Williams. “Quantum gates”. In: *Explorations in quantum computing* (2011), pp. 51–122.

[107] Benjamin Schumacher. “Sending entanglement through noisy quantum channels”. In: *Physical Review A* 54.4 (1996), p. 2614.

[108] Giuliano Benenti et al. *Principles of quantum computation and information: a comprehensive textbook*. World Scientific, 2019.

[109] Joseph B. Altepeter, Daniel F. V. James, and Paul G. Kwiat. “Quantum State Tomography”. In: *Quantum State Estimation*. Ed. by Matteo G. A. Paris and Jaroslav Rehacek. Vol. 649. Lecture Notes in Physics. Berlin, Heidelberg: Springer, 2004, pp. 113–145. DOI: `10.1007/978-3-540-44481-7_4`.

[110] A. Einstein, B. Podolsky, and N. Rosen. “Can Quantum-Mechanical Description of Physical Reality Be Considered Complete?” In: *Phys. Rev.* 47 (10 May 1935), pp. 777–780. DOI: `10.1103/PhysRev.47.777`. URL: `https://link.aps.org/doi/10.1103/PhysRev.47.777`.

[111] Charles H. Bennett et al. “Teleporting an unknown quantum state via dual classical and Einstein-Podolsky-Rosen channels”. In: *Phys. Rev. Lett.* 70 (13 Mar. 1993), pp. 1895–1899. DOI: `10.1103/PhysRevLett.70.1895`. URL: `https://link.aps.org/doi/10.1103/PhysRevLett.70.1895`.

[112] Marek Żukowski et al. ““Event-ready-detectors”Bell experiment via entanglement swapping”. In: *Physical Review Letters* 71.26 (1993), p. 4287.

[113] H.-J. Briegel et al. “Quantum Repeaters: The Role of Imperfect Local Operations in Quantum Communication”. In: *Phys. Rev. Lett.* 81 (26 Dec. 1998), pp. 5932–5935. DOI: `10.1103/PhysRevLett.81.5932`. URL: `https://link.aps.org/doi/10.1103/PhysRevLett.81.5932`.

[114] Artur K. Ekert. “Quantum cryptography based on Bell’s theorem”. In: *Phys. Rev. Lett.* 67 (6 Aug. 1991), pp. 661–663. DOI: `10.1103/PhysRevLett.67.661`. URL: `https://link.aps.org/doi/10.1103/PhysRevLett.67.661`.

[115] Artur Ekert and Peter L Knight. “Entangled quantum systems and the Schmidt decomposition”. In: *American Journal of Physics* 63.5 (1995), pp. 415–423.

[116] John Von Neumann. “Thermodynamik quantenmechanischer gesamtheiten”. In: *Nachrichten von der Gesellschaft der Wissenschaften zu Göttingen, Mathematisch-Physikalische Klasse* 1927 (1927), pp. 273–291.

[117] C. H. Bennet et al. “Mixed-state entanglement and the concurrence”. In: *Physical Rewiew A* (1996).

[118] J Sperling and IA Walmsley. “Quasiprobability representation of quantum coherence”. In: *Physical Review A* 97.6 (2018), p. 062327.

[119] R. Simon. “Peres-Horodecki Separability Criterion for Continuous Variable Systems”. In: *Phys. Rev. Lett.* 84 (12 Mar. 2000), pp. 2726–2729. DOI: `10.1103/PhysRevLett.84.2726`. URL: `https://link.aps.org/doi/10.1103/PhysRevLett.84.2726`.

[120] Claude E Shannon. “A mathematical theory of communication”. In: *The Bell system technical journal* 27.3 (1948), pp. 379–423.

[121] Charles H Bennett et al. “Mixed-state entanglement and quantum error correction”. In: *Physical Review A* 54.5 (1996), p. 3824.

[122] William K Wootters. “Entanglement of formation of an arbitrary state of two qubits”. In: *Physical Review Letters* 80.10 (1998), p. 2245.

[123] Jun John Sakurai and Jim Napolitano. *Modern quantum mechanics.* Cambridge University Press, 2020.

[124] Thomas Nitsche. “From coherent to single-particle quantum walks”. PhD thesis. Universität Paderborn, 2019.

[125] Alan Migdall et al., eds. *Single-Photon Generation and Detection: Physics and Applications.* Vol. 45. Experimental Methods in the Physical Sciences. Amsterdam: Elsevier/Academic Press, 2013. ISBN: 978-0-12-387696-6.

[126] Christophe Couteau. “Spontaneous parametric down-conversion”. In: *Contemporary Physics* 59.3 (July 2018), pp. 291–304. ISSN: 1366-5812. DOI: `10.1080/00107514.2018.1488463`. URL: `http://dx.doi.org/10.1080/00107514.2018.1488463`.

[127] Warren P Grice and Ian A Walmsley. “Spectral information and distinguishability in type-II down-conversion with a broadband pump”. In: *Physical Review A* 56.2 (1997), p. 1627.

[128] CK Law, Ian A Walmsley, and JH Eberly. “Continuous frequency entanglement: effective finite Hilbert space and entropy control”. In: *Physical Review Letters* 84.23 (2000), p. 5304.

[129] Malte Avenhaus et al. "Fiber-assisted single-photon spectrograph". In: *Optics letters* 34.18 (2009), pp. 2873–2875.

[130] C. K. Hong, Z. Y. Ou, and L. Mandel. "Measurement of subpicosecond time intervals between two photons by interference". In: *Physical Review Letters* 59.18 (Nov. 1987), pp. 2044–2046. DOI: `10.1103/PhysRevLett.59.2044`. URL: `https://link.aps.org/doi/10.1103/PhysRevLett.59.2044` (visited on 07/31/2018).

[131] Andreas Schreiber et al. "A 2D Quantum Walk Simulation of Two-Particle Dynamics". In: *Science* 336.6077 (June 2012), pp. 55–58. DOI: `10.1126/science.1218448`. URL: `http://www.sciencemag.org/content/336/6077/55`.

[132] Friedrich Pockels. *Ueber den Einfluss des elektrostatischen Feldes auf das optische Verhalten piëzoelektrischer Krystalle.* Vol. 39. Dieterichsche Verlags-Buchhandlung, 1894.

[133] Vincent Borlisch. *Optimizing round-trip losses in quantum walks.* 2023.

[134] Richard Jozsa. "Fidelity for mixed quantum states". In: *Journal of modern optics* 41.12 (1994), pp. 2315–2323.

[135] Jonas CJ Zatsch et al. "Integrated high-fidelity preparation and analysis of photonic two-qubit states for quantum network nodes". In: *arXiv preprint arXiv:2509.15312* (2025).

[136] Andrew M Childs. "Universal computation by quantum walk". In: *Physical Review Letters* 102.18 (2009), p. 180501.

[137] Peter P Rohde et al. "Multi-walker discrete time quantum walks on arbitrary graphs, their properties and their photonic implementation". In: *New Journal of Physics* 13.1 (2011), p. 013001.

[138] M. Štefaňák, I. Jex, and T. Kiss. "Recurrence and Pólya Number of Quantum Walks". In: *Phys. Rev. Lett.* 100.2 (Jan. 2008), p. 020501. DOI: `10.1103/PhysRevLett.100.020501`.

[139] M Štefaňák, Tamas Kiss, and Igor Jex. "Recurrence properties of unbiased coined quantum walks on infinite d-dimensional lattices". In: *Physical Review A* 78.3 (2008), p. 032306.

[140] Thomas Nitsche et al. "Probing measurement-induced effects in quantum walks via recurrence". In: *Science Advances* 4.6 (2018), eaar6444.

[141] Martin Wimmer et al. "Observation of Bloch oscillations in complex PT-symmetric photonic lattices". In: *Scientific Reports* 5 (2015), p. 17760.

[142] Ken Mochizuki, Dakyeong Kim, and Hideaki Obuse. "Explicit definition of PT symmetry for nonunitary quantum walks with gain and loss". In: *Physical Review A* 93.6 (2016), p. 062116.

[143] Xiang Zhan et al. "Detecting topological invariants in nonunitary discrete-time quantum walks". In: *Physical Review Letters* 119.13 (2017), p. 130501.

[144] Mark Kremer et al. “Demonstration of a two-dimensional PT-symmetric crystal”. In: *Nature communications* 10.1 (2019), pp. 1–7.

[145] Shiqi Xia et al. “Nonlinear tuning of PT symmetry and non-Hermitian topological states”. In: *Science* 372.6537 (2021), pp. 72–76.

[146] Lei Xiao et al. “Observation of non-Bloch parity-time symmetry and exceptional points”. In: *Physical Review Letters* 126.23 (2021), p. 230402.

[147] Andrea Smirne et al. “Experimental control of the degree of non-classicality via quantum coherence”. In: *Quantum Science and Technology* 5.4 (2020), 04LT01.

[148] Shivani Singh et al. “Universal quantum computing using single-particle discrete-time quantum walk”. In: *Scientific Reports* 11.1 (2021), p. 11551.

[149] Andrew M Childs, David Gosset, and Zak Webb. “Universal computation by multiparticle quantum walk”. In: *Science* 339.6121 (2013), pp. 791–794.

[150] Andrew M Childs and Jeffrey Goldstone. “Spatial search by quantum walk”. In: *Physical Review A* 70.2 (2004), p. 022314.

[151] Shantanav Chakraborty et al. “Spatial search by quantum walk is optimal for almost all graphs”. In: *Physical review letters* 116.10 (2016), p. 100501.

[152] Andris Ambainis. “Quantum walk algorithm for element distinctness”. In: *SIAM Journal on Computing* 37.1 (2007), pp. 210–239.

[153] Harry Buhrman et al. “Quantum algorithms for element distinctness”. In: *SIAM Journal on Computing* 34.6 (2005), pp. 1324–1330.

[154] Ivens Carneiro et al. “Entanglement in coined quantum walks on regular graphs”. In: *New Journal of Physics* 7.1 (2005), p. 156.

[155] Xiao-Xu Fang et al. “Maximal coin-position entanglement generation in a quantum walk for the third step and beyond regardless of the initial state”. In: *Physical Review A* 107.1 (2023), p. 012433.

[156] Ebrahim Karimi and Robert W Boyd. “Classical entanglement?” In: *Science* 350.6265 (2015), pp. 1172–1173.

[157] Sandeep K Goyal and CM Chandrashekar. “Spatial entanglement using a quantum walk on a many-body system”. In: *Journal of Physics A: Mathematical and Theoretical* 43.23 (2010), p. 235303.

[158] Salvador E Venegas-Andraca and Sougato Bose. “Quantum walk-based generation of entanglement between two walkers”. In: *arXiv preprint arXiv:0901.3946* (2009).

[159] Gonzalo Abal, Raul Donangelo, and Hugo Fort. “Asymptotic entanglement in the discrete-time quantum walk”. In: *arXiv preprint arXiv:0709.3279* (2007).

[160] Yusuke Ide, Norio Konno, and Takuya Machida. “Entanglement for discrete-time quantum walks on the line”. In: *arXiv preprint arXiv:1012.4164* (2010).

[161] Timothy C Ralph et al. "Linear optical controlled-NOT gate in the coincidence basis". In: *Physical Review A* 65.6 (2002), p. 062324.

[162] Jeremy L O'Brien et al. "Demonstration of an all-optical quantum controlled-NOT gate". In: *Nature* 426.6964 (2003), pp. 264–267.

[163] Zhi Zhao et al. "Experimental Demonstration of a Nondestructive Controlled-NOT Quantum Gate for Two Independent Photon Qubits". In: *Phys. Rev. Lett.* 94 (3 Jan. 2005), p. 030501.

[164] Andrea Crespi et al. "Integrated photonic quantum gates for polarization qubits". In: *Nature communications* 2.1 (2011), p. 566.

[165] Qian Zhang et al. "Femtosecond laser direct writing of an integrated path-encoded CNOT quantum gate". In: *Optical Materials Express* 9.5 (2019), pp. 2318–2326.

[166] Hsuan-Hao Lu et al. "A controlled-NOT gate for frequency-bin qubits". In: *npj Quantum Information* 5.1 (2019), p. 24.

[167] Hsuan-Hao Lu et al. "Building a controlled-NOT gate between polarization and frequency". In: *Optica Quantum* 2.4 (2024), pp. 282–287.

[168] JH Lopes et al. "Linear optical CNOT gate with orbital angular momentum and polarization". In: *Quantum information processing* 18 (2019), pp. 1–10.

[169] A Schreiber et al. "Decoherence and disorder in quantum walks: from ballistic spread to localization". In: *Physical review letters* 106.18 (2011), p. 180403.

[170] Thomas Nitsche et al. "Quantum walks with dynamical control: graph engineering, initial state preparation and state transfer". In: *New Journal of Physics* 18.6 (2016), p. 063017.

[171] Peter C Humphreys et al. "Linear optical quantum computing in a single spatial mode". In: *Physical review letters* 111.15 (2013), p. 150501.

[172] J. L. O'Brien et al. "Demonstration of an all-optical quantum controlled-NOT gate". In: *Nature* 426.6964 (Nov. 2003), pp. 264–267. DOI: `10.1038/nature02054`. URL: `https://www.nature.com/articles/nature02054`.

[173] Jonas Lammers et al. "Resource-efficient universal photonic processor based on time-multiplexed hybrid architectures". In: *arXiv preprint arXiv:2509.22521* (2025).